UiT The Arctic University of Norway

Faculty of Science and Technology
Department of Geosciences

The origin and evolution of LCT pegmatites in Helgeland, northern Norway: stable isotope evidence from tourmaline ($\delta^{11}B$) and garnet ($\delta^{18}O$, $\Delta'^{17}O$)

Amelie Schickhoff

Master's thesis in Geology (GEO-3900), June 2024

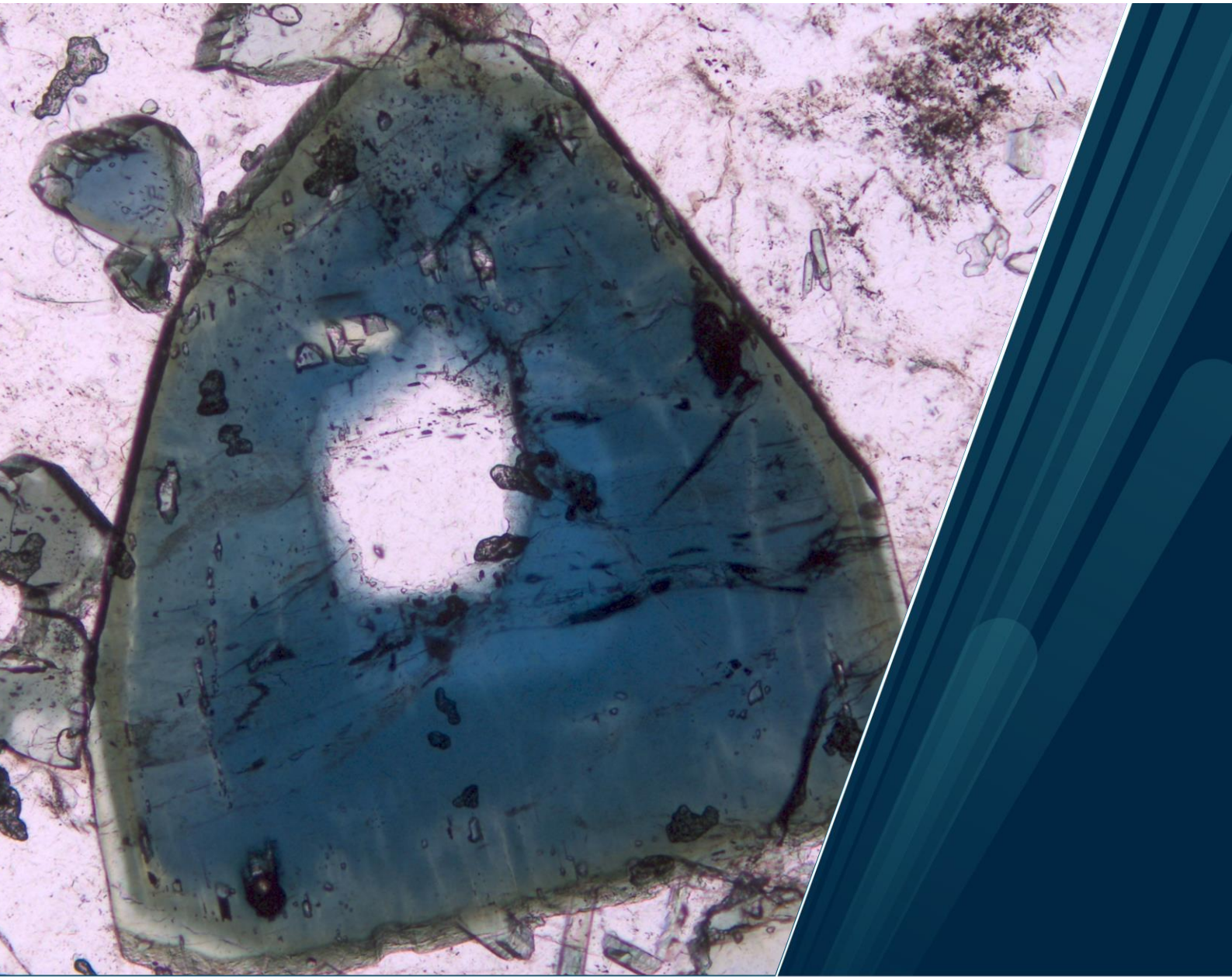

Supervisor:

Prof. Sebastian Tappe (Department of Geosciences, UiT The Arctic University of Norway)

Co-supervisors:

Prof. Stephan Klemme (University of Münster, Germany)

Dr. Christophe Ballouard (University of Lorraine, France)

Abstract

The processes leading to formation of rare-element enriched granitic pegmatites are controversially debated amongst petrologists and economic geologists. Two contrasting genetic models discuss the necessity of a parental granitic pluton as the magma source versus an anatectic origin via partial melting of metasedimentary rocks. Geochemical tools such as the analysis of stable isotopic compositions can be applied to trace the origins and evolution of pegmatite-forming magmas. In this MSc thesis, analyses of the boron isotopic compositions of tourmaline and the triple oxygen isotopic compositions of garnet from granitic pegmatites were combined with their mineral major and trace element compositions to evaluate the tectonomagmatic evolution of the North Helgeland pegmatite field (Nordland county, northern Norway). The magmatic-hydrothermal evolution of this LCT-type pegmatite field is constrained by a more detailed investigation of the previously mined pegmatite body at Ågskardet.

Tourmaline compositions in the selected pegmatite bodies vary between dravite in the upper pegmatite at Ågskardet, schorl at Grønnøya, Ørnes and in outer zones of the Ågskardet old quarry pegmatites, and F-schorl to F-rich elbaitic, tsilaisitic and F-liddicoatitic compositions in the inner zone of the Ågskardet old quarry pegmatite. Lithium contents in tourmaline increase from the outer to the inner pegmatite zones. Tourmaline from the inner zone is enriched in Sr and Pb compared to all other tourmaline crystals studied, and it shows complex replacement textures. Garnet in the North Helgeland pegmatites is dominated by almandine and spessartine components. Except for garnet from the old quarry pegmatite at Ågskardet, the garnet crystals are enriched in HREE.

Tourmaline $\delta^{11}B$ values range from -15.5 to -1.9 ‰ (± 0.9‰, 1-sigma). For tourmaline from the two pegmatite bodies at Ågskardet, the range in $\delta^{11}B$ corresponds to values typical for S-type granites, whereas slightly heavier values were obtained for tourmaline from the pegmatites at Grønnøya and Ørnes. The higher $\delta^{11}B$ values may be explained by a larger proportion of I-type granitic basement in the crustal source to the granitic pegmatite-forming magmas. Within the old quarry pegmatite at Ågskardet, isotopic fractionation between minerals-melt, melt-fluid and fluid-minerals likely played a role in the observed tourmaline $\delta^{11}B$ variations. Garnet $\delta^{18}O$ values range from 5.03 to 11.15 (± 0.1‰, 1-sigma). These values broadly coincide with the whole-rock $\delta^{18}O$ range displayed by Paleoproterozoic basement gneisses in the study area. Triple oxygen isotope data (-76 to -56 ± 0.4 ppm $\Delta'^{17}O$, 1-sigma) for pegmatitic garnet reveal a trend with a slope of 0.527 in linearized triple oxygen isotope space. This slope defined by fresh magmatic garnet crystals indicates low-temperature oxygen isotope fractionation, which

is consistent with and affirms contributions from an anatectic melt sourced from metapelitic rock units.

Tourmaline $\delta^{11}B$ compositions, garnet $\delta^{18}O$ compositions and triple oxygen isotope data are consistent with the North Helgeland pegmatites being produced by partial melting of a heterogeneous crustal source, which contained varying amounts of Paleoproterozoic metasedimentary rocks intruded by ca. 1.8 Ga old granitic orthogneisses of the Transscandinavian Igneous Belt. Oxygen isotope thermometry performed on garnet-quartz pairs yielded apparent temperatures of 585 (± 25 °C, 1-sigma) for the old quarry pegmatite at Ågskardet, 588 (± 25 °C, 1-sigma) for the Grønnøya pegmatite, 823 (± 53 °C, 1-sigma) for the Neverdalen pegmatite and 532 (± 20 °C, 1-sigma) as well as 1139 (± 115 °C, 1-sigma) for two separate samples from the upper pegmatite at Ågskardet. These contrasting values likely indicate disequilibrium conditions in the upper pegmatite. Tourmaline B-isotope variations and trace element characteristics within the old quarry pegmatite at Ågskardet indicate a transition from the main magmatic stage to a late stage dominated by a hydrosaline melt or fluid. This led to crystallization of tourmaline with F-rich elbaitic, tsilaisitic and F-liddicoatitic compositions, as well as to formation of Li-Rb-Cs enriched micas found as inclusions in late-stage tourmaline. Possibly, an aqueous fluid led to changes in the compositions of the rims of these complex tourmaline crystals. The late-stage paragenesis of LCT-type pegmatites presents a favorable exploration target (i.e., the Ågskardet old quarry occurrence), but the vast majority of pegmatite bodies in northern Helgeland have not reached such an advanced stage in their magmatic-hydrothermal evolution.

Acknowledgements

This study would not have been possible without the generous support by Kuniko Norge AS, for which the research team in Tromsø is very grateful.

I am immensely grateful to my supervisor Prof. Sebastian Tappe for the invaluable guidance, support and insightful discussions and feedback throughout the course of this project. His dedication and expertise have been essential to the successful completion of this thesis.

I extend my sincere thanks to my co-supervisors, Dr. Christophe Ballouard, and Prof. Stephan Klemme, for their feedback and support, which have significantly enriched my work.

A special thanks goes to Trine Dahl and Karina Monsen for their time, support, and guidance in the laboratory. I would also like to thank Dr. Eszter Sendula for her time and expertise on the Raman work and Maik Trogisch for the preparation of the grain mounts.

I also want to thank Prof. Axel Müller for sharing very interesting samples with us. They provided another level of detail to the tourmaline work.

I owe a special debt of gratitude to Dr. Stefan Peters for his invaluable expertise and the time and effort he invested into this project. His contributions were crucial.

I am extremely grateful to Dr. Bob Trumbull for his knowledge, expert advice, and support on the boron isotope work. I also want to thank Dr. Michael Wiedenbeck and Frederic Couffignal for their dedicated time and assistance in the SIMS laboratory.

I would like to sincerely thank Dr. Jasper Berndt-Gerdes and Beate Schmitte for their support, effort, and time repeatedly spent on microprobe and LA-ICP-MS lab work.

I want to thank Reginald Lomotey for the enriching dialogue during the entire duration of the project.

Finally, I am profoundly grateful to my friends and family for their unwavering support and encouragement throughout this journey.

Contents

1. Introduction

1.1. General

Granitic pegmatites are recorders of extreme magma differentiation and provide insight into magma evolution and incompatible element enrichment processes (Černý & Ercit, 2005; Černý et al., 2012). They are commonly interpreted as residual melts formed by extreme degrees of fractional crystallization of large peraluminous granitic magma bodies and can serve as significant sources of i) rare elements such as Ta, Nb, Li, Cs, Be, Y, and REE, ii) high-purity quartz, feldspar and mica, and iii) exotic gemstones such as beryl and tourmaline. Hence, granitic pegmatites are of both scientific and economic interest (Linnen & Cuney, 2005; London, 2005; Linnen et al., 2012; London & Kontak, 2012).

The origins of pegmatites have been subject to debate. While the classic model suggests their formation through fractional crystallization of granitic melts, a second model proposes partial melting of metasedimentary rocks enriched in rare metals and fluxing elements or igneous rocks along fluid-channeling shear zones in high-grade metamorphic settings (Kontak et al., 2005; Melleton et al., 2012; Cuney & Barbey, 2014; Romer & Kroner, 2016; Müller et al., 2017; Konzett et al., 2018; Müller et al., 2022). Fractional crystallization of the partial melts results in further enrichment of incompatible elements. Highly evolved pegmatites contain mineral assemblages and trace element signatures diagnostic of either Li-Cs-Ta (LCT) or Nb-Y-F (NYF) affinity (Černý, 1991; Černý et al., 2012) . The difference in formation and internal evolution between pegmatites and other granitic intrusives is explained by highly water- and flux-enriched magmas. These volatile components lead to a reduction of magma viscosity and solidus, enhanced segregation between minerals and melt, and melt-melt-fluid immiscibility (Veksler & Thomas, 2002; Veksler, 2004; Thomas & Davidson, 2012; Thomas et al., 2012). Reaction of fluxing components with major elements within undercooled melts suppresses nucleation, which can lead to rapid crystallization of the supersaturated melt inward, yielding the characteristic crystal sizes and orientation, as well as pegmatite body zoning (London, 2009; Nabelek et al., 2010; Anderson, 2012). However, the necessity of undercooling for the formation of the hallmark pegmatite textures features has been challenged (Thomas & Davidson, 2012; Thomas et al., 2012). Extremely low melt viscosity and melt-melt-fluid immiscibility alone might lead to these.

Some pegmatites lack evidence for fluid separation in late-stage melts, and the importance of magmatic vs. hydrothermal processes has been discussed (London, 2008; Siegel et al., 2016; Kaeter et al., 2018). A potentially useful tool to trace these processes is the analysis of stable isotope variations. Boron isotope analysis of tourmaline from peraluminous granites and

pegmatites has gained popularity (e.g., Trumbull et al., 2008; Trumbull et al., 2013; Siegel et al., 2016; Maner & London, 2017), because of the diagnostic fractionation of the two stable isotopes ^{10}B and ^{11}B between melt and fluid and because boron isotope ratios can be a tracer of the magma sources (Marschall & Foster, 2018). Tourmaline is the most common B-rich mineral and the predominant host of boron in most crustal rocks (Grew & Anovitz, 1996; Dutrow & Henry, 2011; Trumbull et al., 2020). It is a common accessory or minor constituent in peraluminous pegmatites and may record the isotopic composition of the medium it crystallized from (Marschall & Jiang, 2011; Trumbull & Slack, 2018). Tourmaline can form in igneous, diagenetic, metamorphic, metasomatic, and hydrothermal settings, and it has an extensive pressure and temperature stability range (Dutrow & Henry, 2011; van Hinsberg et al., 2011). The wide compositional range makes tourmaline adaptive to a variety of crystallization conditions and varying chemical environments (Dutrow & Henry, 2011; van Hinsberg et al., 2011). Its stability, paired with limited major and trace element diffusivity, enable tourmaline to retain chemical, isotopic, and textural characteristics over prolonged periods of time (Dutrow & Henry, 2011; van Hinsberg et al., 2011).

Another common accessory mineral in granitic pegmatites is garnet (London, 2008). Like tourmaline, it is a refractory, chemically inert mineral exhibiting slow intracrystalline diffusion, which enables it to retain petrogenetic information even at magmatic temperatures (Coghlan, 1990; Lancaster et al., 2009; Lackey et al., 2011). This makes magmatic garnet a very good prospect for triple oxygen isotope analysis. Triple oxygen isotope geochemistry is an advancing field investigating mass dependent and mass independent fractionation in $^{17}O/^{16}O$ relative to $^{18}O/^{16}O$, in a diverse range of geological materials (Bindeman & Pack, 2021). Triple oxygen isotope measurements can provide insights on environmental conditions at the time of mineral formation. Triple oxygen isotopic signatures get passed on from precipitation through sedimentation and metamorphism to anatectic melts and eventually igneous rocks (Bindeman, 2021). In magmatic-hydrothermal systems, triple oxygen isotope systematics can therefore be used to track meteoric components that may be preserved from the sedimentary stage in the evolution of the crustal sources to pegmatites.

1.2. Previous research on the North Helgeland pegmatite field

The North Helgeland pegmatite field in the county of Nordland, North Norway, comprises Caledonian pegmatites of late Silurian to Devonian ages (Ihlen, 2004; Lomotey, 2023). The presence of Li-mineralization in the most evolved pegmatite body at Ågskardet in Meløy municipality is known for more than 70 years (Oftedal, 1950), but received attention mainly from mineral collectors. The limited scientific work focused on specific mineralogy questions rather than tectonomagmatic processes that gave rise to this pegmatite field (Larsen et al.,

1999; Kolitsch et al., 2013; Kristiansen, 2019; Raade, 2020). In 2004, the pegmatite field was mapped by the Geological Survey of Norway (Ihlen, 2004). They identified more than 600 bodies and dykes, most of them barren, but with rare-metal enrichments in individual bodies of the suspected younger generation, specifically at Ågskardet. Due to a lack of potential parental granites in the area, they interpreted the pegmatites to be sourced from Paleoproterozoic orthogneisses and Caledonian supracrustal units by partial melting. Firm evidence to support this interpretation was not published.

In 2023, two MSc theses were completed on i) the mineralogy of the Ågskardet pegmatite (Caixeta Borges, 2023), confirming LCT affinity, and ii) the origin and economic potential of Li-mineralization in the North Helgeland pegmatite field (Lomotey, 2023). The latter study was conducted at UiT and constitutes the current state of research my thesis builds on. Lomotey (2023) conducted U-Pb zircon age dating and was able to distinguish between two pegmatite generations. The older generation (422 ± 5 to 412 ± 5 Ma) is interpreted to be a product of partial melting during the collisional stage of the Caledonian orogeny, whereas the younger generation (403 ± 6 and 387 ± 6 Ma) represents decompression melting in the crust during post-collisional extension (Lomotey, 2023). Lomotey confirms a trend of higher differentiation among the younger pegmatites. This is especially true for the Ågskardet pegmatite, which also yielded the youngest age (387 ± 6 Ma). Zircon Hf isotopic compositions are highly variable for the Helgeland pegmatites (εHfi = -32 to -8). The Paleoproterozoic gneisses in the area show a much smaller range between subchondritic and juvenile compositions (εHfi = -3.3 to +5), which was interpreted as a combination of mantle and more evolved crustal components in the melt source, likely in a subduction zone setting (Lomotey, 2023). The strong εHfi variation within the pegmatites indicates isotopically heterogeneous sources, such as Paleoproterozoic metasedimentary rocks and the regional orthogneisses. However, the orthogneisses, largely displaying I-type signature, cannot be the sole source to the peraluminous LCT-type pegmatites in Helgeland.

1.3. Aims and objectives

Building on these insights, this study aims to further investigate the origin and evolution of the parental magmas to the Helgeland pegmatite bodies to better understand their tectonic setting. Is there evidence supporting collision- and subduction-related anatexis of crustal rocks? What is the role of melt-fluid interactions and volatile fluxes in highly evolved magmatic or magmatic-hydrothermal systems and how do they affect rare-element mineralization processes in the resultant pegmatite bodies?

To answer these research questions, a number of methods are applied. Mineral assemblages and their crystallization sequences are identified for selected pegmatites by optical microscopy

and scanning electron microscopy (SEM) imaging, with special focus on the description of tourmaline textures. In-situ analysis of the major element compositions of garnet, tourmaline, and accompanying mineral phases were conducted using electron probe micro-analysis (EPMA). EPMA analysis serves for further mineral identification and interpretation of melt source and evolution through quantitative compositional characteristics. Garnet and tourmaline from pegmatite samples were analyzed by LA-ICP-MS for their trace element compositions to assess the geochemical signatures with regard to possible LCT affinity. Secondary ion mass spectrometry (SIMS) facilitated the boron isotope analysis of tourmaline crystals to interpret possible sources of boron and isotope fractionation processes in the magmatic-hydrothermal system. The final objective was to trace source rock triple oxygen isotopic compositions by laser-fluorination gas-source mass spectrometry, a novel technique applied to pegmatitic garnet and quartz and bulk basement samples. A possibly shared signature between pegmatites and basement rocks with potentially present meteoric components in the magmatic-hydrothermal system is investigated.

Background information on the applied principles and the geologic setting of the investigated pegmatite bodies is given in Chapter 2 and 3. Sample descriptions are provided in Chapter 4. The analytical methodology is outlined in Chapter 5 and the results are described in Chapter 6. Chapter 7 presents a discussion by putting the results into context, dealing with the research questions sequentially. The conclusions are presented in Chapter 8.

2. Theoretical background

2.1. What are pegmatites?

Pegmatites are igneous rocks of mostly granitic composition, characterized by coarse crystal sizes and distinctive textures. They are commonly observed to form small lenticular or bulbous intrusive bodies as well as dykes and sills (London, 2008; London & Kontak, 2012). Pegmatite intrusions are characterized by coarsening crystal size and mineralogical zonation from the margins toward the center. They typically show anisotropic fabrics such as concentric magmatic layering and oriented crystal growth, as well as intergrowth of feldspar and quartz known as the diagnostic ‘graphic granite’ texture. The main mineral assemblage comprises quartz, K-feldspar (microcline), sodic plagioclase (often albite) and mica (biotite and muscovite); i.e., a typical granitic mineralogy (Anderson, 2012; London & Kontak, 2012). Garnet, tourmaline, apatite and a few other minerals can be present in minor amounts (London & Morgan, 2012). Most pegmatites contain only a small range of accessory minerals and rare element contents are not elevated. These are also referred to as abyssal, barren, or ceramic

pegmatites (e.g., London, 2008). Less than 1% of known pegmatites worldwide contain uncommon minerals rich in rare elements such as Li, Be, Sn, Cs, B and Ta. This exotic subgroup is therefore referred to as the rare-element pegmatites (London & Kontak, 2012).

According to Černý (1991), two families of granitic rare-element pegmatites can be distinguished, which differ in melt origin and composition and, thus, mineralogy and rare metal association. Pegmatites of the LCT family, enriched in Li-Cs-Ta, are typically associated with peraluminous S-type granites, formed by partial melting of metasedimentary rocks in post-collisional orogenic settings. In contrast, pegmatites of the NYF family, enriched in Nb-Y-F, are commonly associated with peralkaline A-type granites, formed in extensional anorogenic settings. I-type granitic magmas are usually poor in B, P and F and thus rarely associated with pegmatites (Černý et al., 2012), although it has been suggested that pegmatites of both families might in some cases be sourced from I-type melts, especially if contaminated with other sources (Černý & Ercit, 2005; Novák et al., 2012). Mixing of LCT and NYF sources can also result in 'hybrid' pegmatites which carry a mixed signature of both families (Černý & Ercit, 2005; Martin & De Vito, 2005; Novák et al., 2012). The concept of pegmatite families was meant to be applied to swarms or fields of comagmatic pegmatites, not to individual bodies (Černý & Ercit, 2005). Many pegmatites within a swarm are barren, while only a few develop the mineralogical characteristics diagnostic for the pegmatite families (Černý et al., 2012). For pegmatites lacking a diagnostic mineralogy, trace element contents of common minerals can be used to constrain their affinity (Cerny et al., 1985; Černý et al., 2012). Of all rare element pegmatites, those with LCT affinity are far more numerous than those with NYF affinity, and within the LCT family, Be- and Li-rich types are most common (Černý et al., 2012).

The main repositories of trace element contents in metasedimentary source rocks forming S-type granitic melts and subsequently LCT pegmatites are feldspars and, chiefly, micas (Dahl et al., 1993; Černý et al., 2012; London et al., 2012). Micas and to a lesser degree feldspars are very reactive and readily transfer their trace element budgets into partial melts at the onset of anatexis (London et al., 2012). Rubidium is slightly and Li and Cs are highly incompatible in K-feldspar, which is continuously crystallizing from the granitic melt, and these elements subsequently concentrate in the melt (Černý et al., 2012). Another element diagnostic for peraluminous S-type granites and enriched in LCT pegmatites is P (London et al., 1999; Martin & De Vito, 2005).

A-type granites are sourced from pyroxene-bearing granulites and varying additional amounts of mantle components or may be entirely mantle-derived (King et al., 1997; Christiansen et al., 2007; Haapala et al., 2007). The signature of NYF pegmatites is consistent with those of alkaline and peralkaline magmas derived from mantle sources considering F and Nb contents

but they carry considerably higher amounts of heavy rare earth elements (Martin & de Vito, 2005). Mantle-derived rocks are often rich in P and Ca, which is not true for A-type granites and NYF pegmatites. Most pegmatites derived from enriched mantle sources do not entirely fit the NYF family traits (Černý et al., 2012). F contents of A-type magmas and NYF pegmatites are ascribed to the decomposition of F-rich amphiboles and micas in the source (Skjerlie & Johnston, 1992; Černý et al., 2012). The predominance of Nb over Ta might originate from their relative abundances in the source or from fractionation processes, but the high Nb/Ta ratio is not entirely understood (Černý et al., 2012; Ballouard et al., 2020b).

Pegmatite formation is commonly linked to fractional crystallization of granitic magma. In this model, pegmatites represent fluid-saturated residual melts at the final stage of fractionation, which explains the high contents of incompatible elements. Additional support for the fractionation model comes from the spatial distribution of pegmatite bodies within and around large granitic plutons of similar compositional affinity, which implies a genetic relationship (e.g., Černý & Ercit, 2005; London, 2008; London & Kontak, 2012). Alternative models argue for pegmatite formation by crustal anatexis in high-grade metamorphic settings, which is appealing in cases where no parental granitic bodies appear to exist, or where regional granitic intrusions differ in age, as well as mineralogical and geochemical compositions (Melleton et al., 2012; Müller et al., 2017; Konzett et al., 2018; Müller et al., 2022). This hypothesis has been presented for pegmatites with NYF signature (e.g., Prol-Ledesma et al., 2012; Müller et al., 2017) and LCT signature (e.g., Kontak et al., 2005; Melleton et al., 2012; Shaw et al., 2022). Based on these studies, the genetic classification system of pegmatites needs a revision, and a new mineralogical and geochemical classification system has been proposed recently (Wise et al., 2022).

In contrast to earlier models that emphasized the role of H_2O in the formation of pegmatites and argued for very slow crystal growth to explain the occurrence of up to several meters large crystals (e.g., Jahns & Burnham, 1969), recent research is focusing on the role of melt undercooling, low viscosity, and presence of fluxing elements such as B, P and F (London, 2009; Anderson, 2012; Dill, 2015). Slow nucleation and rapid crystal growth are caused by undercooling and the formation of a flux-rich crystal-melt boundary layer (London, 2005; Simmons & Webber, 2008; London, 2009). Incompatible elements enrich in the boundary layer, which is in disequilibrium with the bulk pegmatite melt (London, 2017). Once the bulk melt is fully consumed, crystallization from the highly enriched boundary layer starts, precipitating rare-element-minerals such as spodumene or pollucite. This process is supposed to be the reason for the observed sharp zonation of many evolved pegmatites (London, 2008, 2014; Lichtervelde et al., 2018), but has been reported by Thomas et al. (2012) as inconsistent with melt and fluid inclusion studies. Instead, these authors argue for the importance of melt–melt–

fluid immiscibility in pegmatite formation and deemphasize the need for liquidus undercooling. Additionally, they report pegmatite melt formation also in the absence of the commonly implied fluxing agents P and F, if other fluxing elements such as B and carbonates are present (Thomas & Davidson, 2012; Thomas et al., 2012).

Pegmatite zonation typically occurs concentrically or layered around the pegmatite's core or along its length, recording the progressive crystallization from the margins inward (Cameron et al., 1949; Jahns, 1982; London, 2008). Based on textural and mineralogical features, the following zones are distinguished:

(1) The border zone is the outermost contact to the country rocks. It is often composed of fine-grained quartz and feldspar and can contain larger crystals of accessory minerals (London, 2008). (2) The wall zone typically shows the same mineralogy plus mica but displays a coarser grain size. Accessory garnet and tourmaline are common (London, 2008). (3) The intermediate zones in the interior of a pegmatite body show an abrupt increase in grain size and tend to be dominated by a single mineral phase, typically microcline, plagioclase, quartz, spodumene, petalite or montebrasite (London, 2008). They can be asymmetrically distributed and pinch out in thinning bodies (London, 2008). (4) The core is the innermost unit of a pegmatite body. Monomineralic quartz cores are common, but perthite, albite, Li-aluminosilicates and phosphates also occur (London, 2008). (5) Some evolved pegmatites contain a so-called replacement zone, characterized by pronounced alteration of the pegmatitic minerals to a fine-grained pseudomorphic assemblage (London & Burt, 1982; London, 2008). Replacement zones often contain monomineralic (e.g., albite) masses or high concentrations of exotic minerals, explained by hydrothermal activity (London, 2008). They are typically the mineralogically most diverse unit of a pegmatite (Černý & Ercit, 2005; London, 2008). In zoned pegmatites, rare-element enrichment typically occurs from the intermediate zone inward (Černý, 1991). It is, however, important to note that not all chemically evolved pegmatites exhibit zoning (London, 2008).

2.2. Tourmaline

Tourmaline is a borosilicate mineral with the generalized structural formula $XY_3Z_6(T_6O_{18})(BO_3)_3V_3W$, which enables large compositional diversity (Hawthorne & Henry, 1999; Henry et al., 2011). The most common ions (or vacancy) are Na^+, Ca^{2+}, K^+, and vacancy on the X site; Mg^{2+}, Mn^{2+}, Al^{3+}, Li^{1+}, Fe^{3+}, and Cr^{3+} on the Y site; Al^{3+}, Fe^{3+}, Mg^{2+}, and Cr^{3+} on the Z site; Si^{4+}, Al^{3+}, and B^{3+} on the T site; B^{3+} on the B site; OH^- and O^{2-} on the V site and OH^-, F^-, and O^{2-} on the W site (Henry et al., 2011). The nomenclature of minerals of the tourmaline

supergroup is based on chemical systematics following the IMA−CNMNC dominant valency-rule (Hatert & Burke, 2008) and is published by the Subcommittee on Tourmaline Nomenclature (STN) of the IMA-CNMNC in Henry et al. (2011). For each distinct mineral species there is an irreducible endmember composition. The subdivision into three primary groups is based on X site occupancy. An alkali, a calcic, and a vacancy group are distinguished. The different valencies of the cations, or vacancy respectively, on the X site are charge-balanced by coupled substitution. For minerals that are dominated by OH^- or F^- on the W site, the OH^- - dominant species is eponymous and considered the root composition. Compositions with dominant F^- on the W site require a corresponding prefix, similarly to compositions dominated by other cations in the specific sites than the reference root composition (Henry et al., 2011).

Tourmaline commonly has an acentric and polar rhombohedral symmetry (space group R3m), although lower symmetries have been reported for specific occurrences (e.g., Akizuki et al., 2001; Shtukenberg et al., 2007). It forms prismatic to acicular and fibrous ditrigonal-pyramidal crystals with vertical running dominant trigonal and subordinate hexagonal prisms (Hawthorne & Dirlam, 2011; Nesse, 2014). In cross-section perpendicular to c the vicinal character of the prism faces causes a spherical impression. The tetrahedrally coordinated T site is predominantly occupied by Si but can also contain Al and B. Six $[TO_4]$ tetrahedra are connected on their corners to form hexagonal $[T_6O_{18}]$ rings which make up the cyclosilicate structure (Fig. 1). The base of the $[TO_4]$ tetrahedra are parallel to and their free O atoms point towards (001), which results in acentric symmetry and the polar properties (Hawthorne and Dirlam, 2011). Boron forms trigonally coordinated $[BO_3]$ rings. Y and Z sites are octahedrally coordinated. Edge-sharing $[ZO_5OH]$ octahedra form left- and right-handed helical screw axes parallel to c, which are connected to each other through their corners as well as through groups of three edge-sharing $[YO_4(OH)_2]$ octahedra. The $[BO_3]$ rings are connected to both the $[ZO_5OH]$ octahedra and the $[YO_4(OH)_2]$ octahedra. The large X atoms lie above the 6 free O atoms of the $[T_6O_{18}]$ rings and below the 3 O atoms of the $[BO_3]$ rings. The X atoms are only weakly bonded, and the X site can be partially unoccupied.

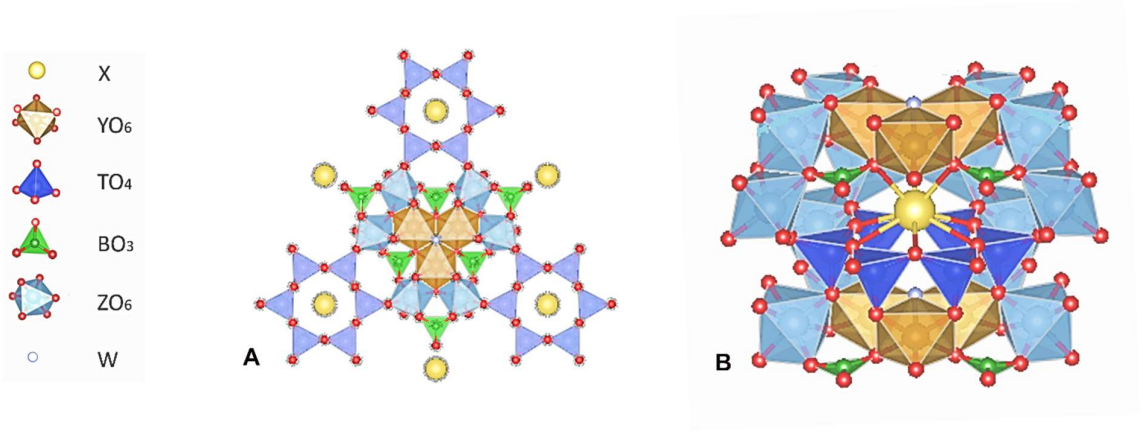

***Figure 1**. Structural model of tourmaline. A) projected onto (001) and B) oblique view. Crystallographic data from Tippe and Hamilton (1971). Visualized with Vesta 3.90 (Momma & Izumi, 2011).*

The great diversity in tourmaline composition leads to a broad spectrum of colors from black, brown, blue, green, pink, yellow to colorless. Chemical zoning is common and is often visible both in hand specimen and thin section (Pezzotta & Laurs, 2011; Nesse, 2014). The most common tourmaline is black Fe-rich tourmaline of schorlitic composition (Nesse, 2014). The structural formula of the schorl endmember is $NaFe^{2+}{}_3Al_6(BO_3)_3Si_6O_{18}(OH)_3(OH)$. Within the alkali tourmalines, schorl forms a subsystem with dravite (endmember composition $NaMg_3Al_6Si_6O_{18}$ $(BO_3)_3(OH)_3(OH)$) and elbaite ($Na(Li_{1.5}Al_{1.5})$ Al_6 (Si_6O_{18}) $(BO_3)_3$ $(OH)_3$ (OH)) (Henry et al., 2011).

2.3. Boron isotopes with special reference to tourmaline and granite

Boron is a lithophile element that is incompatible in igneous systems, but it is essential for the formation of tourmaline (London et al., 1996; Dutrow & Henry, 2011; Trumbull & Slack, 2018). It is readily mobilized and transported by silicic melts and aqueous fluids and is therefore enriched in the continental crust relative to the mantle (Dutrow & Henry, 2011; Trumbull & Slack, 2018). Sea water is a significant boron reservoir, and boron transfers into Earth's crust through subduction of hydrothermally altered oceanic crust and B-incorporating pelagic sediments. Increasing P-T conditions and circulating fluids in the subducting slab enable tourmaline growth, making tourmaline an important factor in the boron geochemical cycle (Dutrow & Henry, 2011). At the Earth's surface, boron can be concentrated through evaporation processes and is precipitated in borate minerals (Dutrow & Henry, 2011). In igneous settings, boron enriches through partial melting of boron-bearing (often metasedimentary) source rocks (Marschall & Jiang, 2011; Trumbull & Slack, 2018). Due to its incompatibility in major rock-forming minerals in granitoids, it concentrates in fractionated granitic and pegmatite-forming melts, and eventually in aqueous fluids (Morgan & London, 1989; Dutrow & Henry, 2011). In the absence of tourmaline, boron is mainly hosted by micas in felsic rocks. Pelitic and

metapelitic rocks have the highest concentrations of boron, owed to their mica and clay content (Gao et al., 1998; Trumbull & Slack, 2018).

Boron has two naturally occurring stable isotopes, ^{10}B and ^{11}B, which differ in their atomic masses by 10% and show an abundance ratio of 1:4 (Kowalski & Wunder, 2018; Trumbull et al., 2020). The ratio of the two isotopes is expressed as $\delta^{11}B$ values as the ‰ deviation relative to a standard (NIST SRM-951). The range of $\delta^{11}B$ values in nature is about 100‰ (Barth, 1993; Palmer & Swihart, 1996). Seawater is enriched in ^{11}B, and rocks of the oceanic crust incorporate the heavy isotope through alteration processes. For this reason, melts related to subduction zone magmatism are typically isotopically heavier than common continental crust, which is depleted in ^{11}B due to subaerial weathering processes (Marschall & Jiang, 2011). The commonly cited range for $\delta^{11}B$ values of the upper continental crust is -8 to -12‰ (Marschall & Jiang, 2011; Trumbull & Slack, 2018). S-type granitic rocks have a mean $\delta^{11}B$ value of -11‰ (s.d. = 4), I-type granites of -2‰ (s.d. = 5), and unaltered MORBs of -7‰ (s.d. = 1) (Trumbull & Slack, 2018).
There is significant fractionation of the two isotopes between minerals, melts and aqueous fluids, which is dependent on temperature, melt and fluid composition and, most importantly, the structural configuration of boron in the coexisting phases (Palmer & Swihart, 1996; Marschall & Jiang, 2011; Kowalski et al., 2013; Kowalski & Wunder, 2018).

The small cation B^{3+} can enter both trigonally and tetrahedrally coordinated sites in mineral structures and occurs in trigonal and tetrahedral coordination in melts, where trigonal $[BO_3]$ is considered the predominant species, particularly in peraluminous compositions and at higher temperatures (Tonarini et al., 2003; Kowalski & Wunder, 2018; Li et al., 2021). In aqueous fluids, boron forms tetrahedrally coordinated $B(OH)_4^-$ in higher pH alkaline fluids and at higher temperatures, but trigonally coordinated $B(OH)_3$ complexes in acidic solutions (Schmidt et al., 2005; Dutrow & Henry, 2011; Kowalski & Wunder, 2018). The ^{11}B isotope prefers trigonal coordination and ^{10}B favors tetrahedral coordination (Kakihana et al., 1977). This is due to the lighter isotope's preference for longer B-O bonds present in higher coordinations (Hawthorne et al., 1996; Wunder et al., 2005; Kowalski et al., 2013). Experimental studies on B-isotope fractionation between tourmaline and aqueous fluid report an enrichment of ^{11}B in the fluid under all conditions studied and a decrease in fractionation with increasing temperature and pressure (Palmer et al., 1992; Meyer et al., 2008). There is currently only one experimental study on the fractionation of B-isotopes between tourmaline and melt (Cheng et al., 2022). This study reports enrichment of ^{11}B in granitic melts relative to crystallizing tourmaline and stronger fractionation at lower temperatures, assuming no exsolution of fluids. At the magmatic-hydrothermal transition, ^{11}B partitions into the aqueous fluid, resulting in lower $\delta^{11}B$ values for

late magmatic tourmaline relative to the starting magma, whereas there is enrichment in ^{11}B in tourmaline crystallizing from the fluid (Trumbull & Slack, 2018, and references therein).

Fractionation between coexisting mineral phases (and involved fluids) is best studied for tourmaline and mica, which are the main boron hosts in granitic melts (Trumbull & Slack, 2018; Kowalski & Wunder, 2018; Li et al., 2021), in both experimental studies (Wunder et al., 2005; Meyer et al., 2008) and natural samples (Klemme et al., 2011). These studies report considerable fractionation between mica and tourmaline, with mica showing lower $\delta^{11}B$ than coexisting tourmaline. In mica, boron is tetrahedrally coordinated and enriched in ^{10}B. Fluids are enriched in ^{11}B in trigonal coordination (Wunder et al., 2005; Meyer et al., 2008). Inconsistencies in the magnitude of the reported observations can be attributed to the presence of tetrahedrally coordinated boron in neutral aqueous fluids at high temperatures (Kowalski et al., 2013). The enrichment of ^{10}B in micas and clay minerals due to tetrahedral coordination is also the main reason for the light isotopic signature of S-type granites (Trumbull & Slack, 2018). Analyses of natural samples show that while the crystallization of micas (and other phases containing tetrahedrally coordinated B) can lead to enrichment of ^{11}B in the residual melts, crystallization of tourmaline might have the opposite effect (Trumbull et al., 2008; 2013; Siegel et al., 2016).

2.4. Garnet

The garnet supergroup includes all minerals isostructural to garnet regardless of which elements occupy the atomic sites (Grew et al., 2013). The general formula for the garnet supergroup minerals is $\{X_3\}[Y_2](Z_3)\phi_{12}$, where X, Y and Z refer to dodecahedral, octahedral, and tetrahedral sites, respectively, and ϕ is O, OH, or F (Grew et al., 2013). Except for two OH-bearing species, all garnet supergroup minerals are of cubic symmetry, space group Ia 3d (Grew et al., 2013).

The garnet supergroup is subdivided into five groups on the basis of the total charge of cations in the tetrahedral site. The garnet group has 14 members, which have the Z site occupied by Si_3 and the ϕ site by O_{12}. Species are distinguished based on the dominant-valency rule and the nomenclature is approved by the IMA-CNMNC (Hatert & Burke, 2008; Grew et al., 2013). The most common endmembers are pyrope, almandine, spessartine, uvarovite, grossular and andradite (Baxter et al., 2013; Okrusch & Matthes, 2014). Before the revision in 2013 by Grew et al. (and as still commonly used today), their formulas were reported as: $Mg_3Al_2(SiO_4)_3$ (pyrope), $(Fe^{2+})_3Al_2(SiO_4)_3$ (almandine), $(Mn^{2+})_3Al_2(SiO_4)_3$ (spessartine), $Ca_3Cr_2(SiO_4)_3$ (uvarovite), $Ca_3Al_2(SiO_4)_3$ (grossular), and $Ca_3(Fe^{3+})_2(SiO_4)_3$ (andradite) (Grew et al., 2013). In revised form, the formula for pyrope reads: $\{Mg_3\}[Al_2](Si_3)O_{12}$ (Grew et al., 2013). The end-members almandine + pyrope, as well as almandine + spessartine, and grossular + andradite

are solid solution series. The almandine - pyrope as well as the almandine - spessartine solid solutions can incorporate up to 30 mol.% grossular or andradite component (Okrusch & Matthes, 2014).

The structure of garnet is characterized by alternating Zϕ4 tetrahedra and Yϕ6 octahedra, which form angled chains parallel to the edges of the unit cell (Fig. 2). These tetrahedra and octahedra share corners to create a three-dimensional framework. Within this framework, triangular dodecahedral cavities form, which contain the X site. Each anion is coordinated by one Z, one Y, and two X cations, resulting in a high number of shared edges between the dodecahedra and the octahedra/tetrahedra (Grew et al., 2013). The large edge-sharing sites can incorporate significant amounts of heavy rare-earth elements (Baxter et al., 2013). The octahedra and tetrahedra do not share edges with each other (Grew et al., 2013; Baxter et al., 2013).

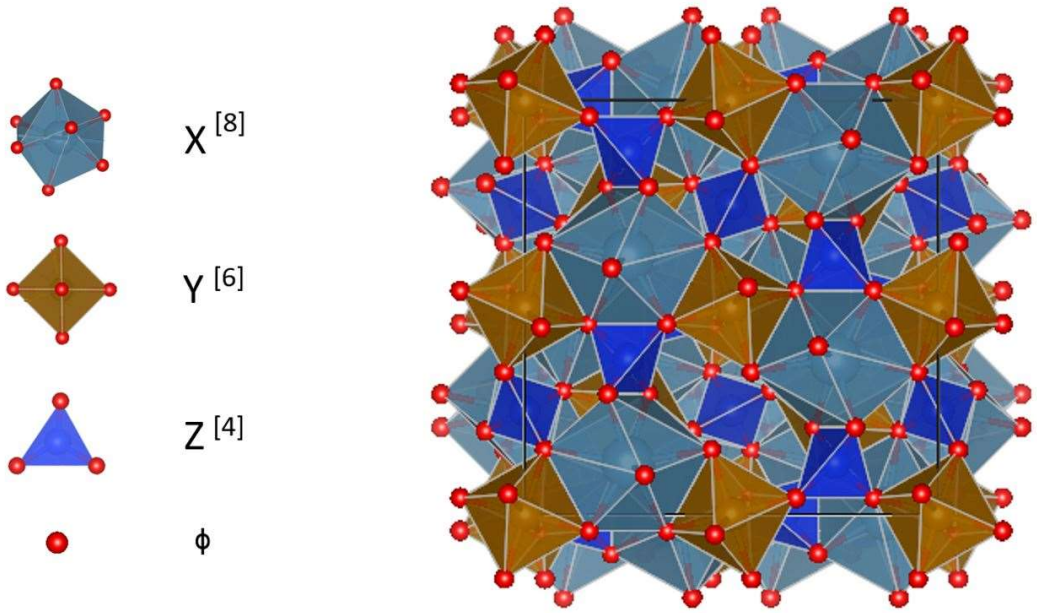

Figure 2. *Structural model of garnet. Projected onto (001). Crystallographic data from Novak and Gibbs (1971). Visualized with Vesta 3.90 (Momma & Izumi, 2011).*

Garnet is a common rock-forming mineral stable over a wide range of temperatures and pressures. It is highly refractory and shows low solubility as well as low diffusion (Coghlan, 1990; Baxter & Scherer, 2013). It predominantly occurs in metamorphic rocks of the continental crust and garnet peridotites from Earth's mantle (Baxter et al., 2013; Baxter et al., 2017), but can also occur as accessory mineral in peraluminous granitoids and pegmatites (Stevens et al., 2007; Erdmann et al., 2009; Villaros et al., 2009; Lackey et al., 2012; Müller et al., 2012; Melo et al., 2017).

2.5. Stable oxygen isotopes

2.5.1. Applications of oxygen isotope analyses

Oxygen is the most abundant element on Earth and occurs in gaseous, liquid and solid phases over a wide range of stability (Hoefs, 2018). Oxygen has three stable isotopes, which have abundances of 99.757% (^{16}O), 0.038% (^{17}O), and 0.205% (^{18}O) (Rosman & Taylor, 1998). The $^{18}O/^{16}O$ ratio shows a variance of about 10% in natural samples and is most commonly applied in geological studies because of the high abundances of these two isotopes and their great mass difference (Hoefs, 2018). The oxygen isotope ratios $^{17}O/^{16}O$ and $^{18}O/^{16}O$ are commonly expressed as δ17O and δ18O, which is the per mil deviation from a standard (McKinney et al., 1950).

Oxygen isotope geochemistry is applied for a variety of purposes, including paleoclimatology, hydrology, biological and ecological studies, and research on hydrothermal systems and geological processes (e.g., Koch, 1998; Muehlenbachs, 1998; Goodfriend, 1999; Yakir & Sternberg, 2000). Variations in the oxygen isotopic compositions of water can, for example, track mixing of different water sources (Gat, 1996). Furthermore, oxygen isotope analyses of ice cores can provide insights into past temperature and precipitation patterns (Petit et al., 1999; Landais et al., 2008). In rocks and minerals, oxygen isotopes can provide insights into formation environment, metamorphism, and alteration processes. The oxygen isotopic compositions of rocks and minerals are potentially preserved billions of years and their interaction with atmospheric O_2 can be reconstructed (Hoefs, 2018; Pack, 2021).

2.5.2. Oxygen isotope thermometry

Oxygen isotope fractionation principles are also applied to estimate peak metamorphic or magmatic temperatures (Garlick & Epstein, 1967; Bottinga & Javoy, 1975; Eiler et al., 1993; Farquhar et al., 1996; Valley, 2001; Larson & Sharp, 2005). The so-called oxygen isotope thermometry records equilibrium temperatures at peak metamorphic conditions or in a magmatic system and employs the inverse variation of isotopic fractionation extent with temperature. Different minerals have different closure temperatures for oxygen diffusion (Dodson, 1973; Giletti, 1986). Garnet is characterized by slow oxygen diffusivity and a high closure temperature of >800 °C. In garnet of magmatic origin, its oxygen isotopic composition is therefore expected to be close to that of the magma and the source (Coghlan, 1990; Farquhar et al., 1996; Harris & Vogeli, 2010). In contrast, quartz has a significantly lower closure temperature of <550 °C, faster diffusivity, and it has the highest $\delta^{18}O$ of any mineral in the same rock at equilibrium (Farver, 2010; Bucholz et al., 2017; Quinn et al., 2017). The order

of equilibrium ^{18}O enrichment in common igneous minerals is quartz > alkali-feldspar > plagioclase > biotite > apatite > orthopyroxene > zircon > clinopyroxene > amphibole > garnet > olivine > oxides (Zheng, 1993; Eiler, 2001; Valley et al., 2003). The extent of enrichment is determined by a mineral's cation-oxygen bond strength and cation mass. Bond strength is dependent on the cation valence state, coordination number, and corresponding ionic radii (Zheng, 1993; Hoefs, 2018). At equilibrium, the heavier isotope will tend to occupy the site with the stronger bond, because it minimizes the energy of the system (Hoefs, 2018). In quartz, each atom is strongly covalently bound in an infinite three-dimensional framework of silica tetrahedra, where each tetrahedron is bonded to four other tetrahedra. The ^{18}O isotope partitions therefore preferentially into quartz (Zheng, 1993).

Due to the large oxygen isotope fractionation between garnet and quartz, thermometry on this mineral pair can be performed with reasonable precision ($\Delta^{18}O(Qz–Grt) = 2.71$ at 1000 K; Coghlan, 1990). Retrograde or sub-solidus isotope exchange or hydrothermal alterations during cooling and exhumation can influence the accuracy of $\delta^{18}O$ thermometry (Eiler et al., 1993; Kohn, 1999; Valley, 2001). In magmatic systems, sub-solidus oxygen isotope re-equilibration through diffusive exchange between quartz and feldspar can be observed in slowly cooled plutons (Bucholz, 2017). Thus, empirically or theoretically obtained fractionation factors can also be employed to test for disequilibrium in mineral assemblages (Zheng, 1993).

Although garnet is highly suitable for oxygen isotope studies, the application of the method to non-metamorphic garnet has only recently gained momentum. Although there is now a number of $\delta^{18}O$ studies on garnet from granitic plutons (e.g., King & Valley, 2001; Lackey et al., 2006; Harris & Vogeli, 2010; Lackey et al., 2012; Quintero et al., 2021), $\delta^{18}O$ data for garnet from pegmatites are scant (Zhang et al., 2001; Samadi et al., 2014; Yu et al., 2021).

2.5.3. The concept of 'triple oxygen' isotope analysis

Fractionation between ^{17}O and ^{16}O is approximately half of the fractionation between ^{18}O and ^{16}O, and it was therefore recognized as mass-dependent isotope fractionation by Craig (1957). Measurements of ^{17}O were not initially considered to offer any further insights beyond those provided by the $^{18}O/^{16}O$ ratio (Hoefs, 2018; Miller & Pack, 2021). During the past two decades, with advancing analytical techniques, it was recognized that $^{17}O/^{16}O$ data can yield additional geoscientific information (Bindeman & Pack, 2021). So-called triple oxygen isotope analysis helps to recognize the effects of water compositions and temperatures on oxygen isotope fractionation. In a $\delta^{17}O$ vs. $\delta^{18}O$ diagram, all terrestrial rocks and minerals plot along a line with a slope (λ) and an intercept (γ) and the deviation from the chosen reference line is reported as $\Delta^{17}O$. A commonly used slope value is 0.52 (Cao & Liu, 2011). This reference line used to be referred to as Terrestrial Fractionation Line (TFL), but Pack and Herwartz (2014) demonstrated

that a single TFL is invalid because different geochemical reservoirs on Earth are characterized by different mass fractionation lines. Fractionation factors between two isotopes of the same element are commonly denoted α. The triple isotope fractionation exponent ($\theta \equiv \ln^{17/16}\alpha / \ln^{18/16}\alpha$) for fractionation between two reservoirs can be determined experimentally (e.g., Angert et al., 2003; Barkan & Luz, 2005; Luz & Barkan, 2005; Landais et al., 2006), or theoretically (Cao & Liu, 2011). It can vary between 0.5 (lower limit for kinetic fractionation) and 0.5305 (equilibrium high temperature limit) (Matsuhisa et al., 1978; Young et al., 2002; Cao & Liu, 2011). The variation results from energy differences between molecules incorporating different isotopes, which depends not only on the respective masses of the isotopes, but also on their reduced masses within the framework of a vibrating molecule (Matsuhisa et al., 1978; Miller & Pack, 2021). The fractionation exponent indicates the slope of a line resulting from the relevant fractionation process. The global meteoric water line has a slope of 0.528 and an intercept of 0.033‰ (Luz & Barkan, 2010). It is a result of combined equilibrium fractionation (evaporation, condensation; $\theta \approx 0.529$, and kinetic diffusion; $\theta \approx 0.518$) (Pack & Herwartz, 2014). For rocks and minerals, the slope is typically reported as being between 0.524 and 0.526 (Miller et al., 1999; Rumble et al., 2007; Sharp et al., 2016).

The oxygen isotopic composition of silicates in the Earth's crust results from complex interactions between solids, melts and aqueous fluids, and is significantly influenced by temperature (Miller & Pack, 2021). Studies on natural rocks and minerals show that their oxygen triple isotope distributions result from the various combined various slopes of involved fractionation processes, dominated by equilibrium processes (Miller & Pack, 2021, and references therein).

Due to the not completely linear relationship of $\delta^{17}O$ vs. $\delta^{18}O$, the resulting slope is dependent on the range of δ values and the isotopic composition of the reference material. The mass-dependent fractionation relationship that describes this oxygen triple isotope distribution has the designated exponent term λ (Miller & Pack, 2021). λ is an empirical parameter based on cumulative fractionation effects. To quantify deviations from a specific mass-dependent fractionation curve, the term $\Delta'^{17}O$ is used (Miller, 2002). It describes the linearized absolute $\delta^{17}O$ and $\delta^{18}O$ data in relation to the fractionation exponent λ:

$$10^3 \ln(1 + \Delta^{17}O) = 10^3 \ln(1 + \delta^{17}O) - \lambda 10^3 \ln(1 + \delta^{18}O) \quad (1)$$

$$\Delta' 17\mathrm{O} = \delta'^{17}O - \lambda \delta'^{18}O \quad (2)$$

The value of λ is assigned arbitrarily. Commonly used is 0.528 (Sharp et al., 2018; Miller & Pack, 2021). To account for any offset from the zero point of the δ scale, the intercept γ (γ' ≡ 10^3ln(1+ γ) is used:

$$\Delta'17O = \delta'^{17}O - \lambda\delta'^{18}O - \gamma' \quad (3)$$

To clarify that the reference line is pre-defined, the terminology λ_{RL} and γ_{RL} is commonly employed (Miller & Pack, 2021). There is, however, no general acceptance of the notations used in the young field of triple oxygen isotope geochemistry, which is important to bear in mind when comparing data from different publications (Miller & Pack, 2021).

2.5.4. Non-mass-dependent fractionation processes

Non-mass-dependent fractionation processes can lead to anomalous ^{17}O enrichments or depletions, typically observed in meteorites (e.g., Clayton et al., 1973; Thiemens & Heidenreich, 1983; Chakraborty et al., 2013). These processes can usually be traced to photochemical reactions and have only been observed in terrestrial materials that were in contact with or influenced by the troposphere and stratosphere, for instance through explosive volcanic eruptions (Bao et al., 2000; Savarino et al., 2003; Martin & Bindeman, 2009). Non-mass-dependent fractionation of oxygen isotopes that does not involve photochemistry has so far only been produced in laboratory experiments (Bhattacharya & Thiemens, 1988; Wen & Thiemens, 1990, 1991; Sun & Bao, 2011).

3. Geological background

3.1. Tectonic setting

The Helgeland pegmatite district in Nordland County, northern Norway, is located in the Paleoproterozoic Svecofennian basement domain of the Fennoscandian Shield, which is partly overlain by Early Paleozoic Caledonian nappe complexes in the study area (Fig. 3).

The Svecofennian domain (2.0 – 1.75 Ga) is one of the major domains of the Fennoscandian Shield, adjacent to the Archean domain (3.1 – 2.6 Ga) in the northeast and the Mesoproterozoic Sveconorwegian domain (1.14 – 0.9 Ga) in the southwest (Åhäll & Larson, 2000; Skår, 2002; Åhäll & Connelly, 2008). It represents continental crust of several arc systems that were accreted to the craton (Högdahl et al., 2004). The Svecofennian domain is exposed in several tectonic windows in central Nordland, namely Sjona, Høgtuva, Nasafjäll, Svartisen, Glomfjord, Fykan and Bjellåtind (Wilson & Nicholson, 1973; Skår, 2002). The

voluminous granites and granitic gneisses of this basement domain represent protracted magmatic activity between 1.85 and 1.63 Ga (Svecofennian and Gothian orogenies (Bingen & Solli, 2009), and they are part of the Transscandinavian Igneous Belt (TIB; Patchett et al., 1987). The TIB comprises numerous batholiths, predominantly postorogenic granitoids, stretching 1400 km from southeastern Sweden to northern Norway (Romer et al., 1992; Skår, 2002; Högdahl et al., 2004; Bingen & Solli 2009). The granitoid magmatism was related to convergent-margin tectonics in a continental arc setting along the western margin of Baltica and sourced by partial melts of Svecofennian crust with additional mantle components (Åhäll & Larson, 2000; Högdahl et al., 2004). Two phases of magmatism are distinguished, the so-called TIB-1 (1.85 – 1.76 Ga) and TIB-2 (1.71 - 1.67 Ga) (Larson & Berglund, 1992; Romer et al., 1992; Högdahl & Sjöström, 2001; Högdahl et al., 2004). The TIB plutonic rocks are mainly granitic or (quartz-) monzogranitic to monzodioritic rocks of alkali-calcic to calc-alkaline or alkaline and peraluminous to metaluminous composition. In the S-I-A-M classification, they range from I- to A-type granitic rocks (Skår, 2002; Högdahl et al., 2004). Basement rocks of the Sjona and Høgtuva tectonic windows are of quartz-monzonitic to granitic and syenitic to granitic composition, respectively, and have TIB-1 ages (1797 ± 3 Ma and 1800 ± 2 Ma, respectively) (Skår, 2002). Earlier age determinations of basement rocks in the study area yielded 1747±86 Ma (Cribb, 1981) and 1694±73 Ma (Wilson & Nicholson, 1973) for the Glomfjord window and 1749±53 Ma for the Bjellåtind window (Cribb, 1981). The lithologies were described as microcline granite (Bjellåtind; Cribb, 1981) and granitic to monzonitic and granodioritic gneisses (Fykan and Glomfjord; Rutland et al., 1960). The deformation of the basement gneisses is related to late Svecofennian orogenic processes. It is, however, more pronounced close to the contact of Caledonian nappes (Andresen & Tull, 1986; Northrup, 1997; Skår, 2002).

The Caledonides cover up to 2000 km of western Scandinavia and major parts of Norway (Gee et al., 2008; Corfu et al., 2014). The Caledonian orogenesis (490-390 Ma) started with subduction along both margins of the Iapetus Ocean during the early Ordovician, followed by the collision of Baltica (i.e., the Fennoscandian Shield) and Laurentia with partial subduction of Baltica during the mid Silurian to early Devonian (Gee et al., 2008). During the early Devonian, rapid exhumation of the metamorphosed hinterland occurred, before a phase of post-orogenic collapse and extension with persistent deformation into the late Devonian (Gee et al., 2008).

The nappes of the Caledonian orogeny are preserved on either side of the North Atlantic (Gee et al., 2008). The thrust systems are E-vergent in Scandinavia and W-vergent in Greenland, and their opposing characteristics are ascribed to underthrusting of Laurentia by Baltica (Gee et al., 2008). During the post-collisional extensional stage of the orogeny, the Caledonian

nappes were transported on ductile shear zones parallel to the basement-allochthon contact, exposing the underlying basement rocks (Larsen et al., 2002; Skår, 2002).

The current subdivision of the Caledonian nappe complexes describes four tectonostratigraphic units: Lower, Middle, Upper and Uppermost Allochthons, which differ in provenance, tectonic, and metamorphic history (Gee & Sturt, 1985; Roberts & Gee, 1985). The Lower and Middle Allochthons where derived from the Baltoscandian platform and margin (Roberts & Gee, 1985; Andréasson, 1994), the Upper Allochthon represents terranes of the Iapetus ocean and its eastern margin (Stephens & Gee, 1985; Andréasson, 1994), and subunits of Laurentian origin (Spjeldnæs, 1985; Stephens & Gee, 1985; Andréasson, 1994; Corfu et al., 2011). The Uppermost Allochthon was presumably derived from the Laurentian continental margin (Stephens & Gee, 1985; Stephens et al., 1985; Roberts et al., 2007).

The exposed nappe complexes in the study area, namely Helgeland and Rödingsfjäll nappes, are part of the Uppermost Allochthon. The structurally higher Helgeland nappe complex comprises five different nappe units, which consist of metasedimentary and migmatitic metasedimentary units with inferred late Neoproterozoic to Palaeozoic depositional ages (Yoshinobu et al., 2002; Barnes et al., 2007). The lower two metasedimentary nappes overlie tectonically fragmented ophiolitic rocks and include metawackes, metapelites, calc-silicate rocks, conglomerates and amphibolite-facies marbles (Løseth & Thorsnes, 1991). The structurally higher nappes of the Helgeland nappe complex consist of migmatitic quartzofeldspathic and semi-pelitic gneisses, calc-silicate gneisses, and marbles. The fact that they are migmatized indicates upper amphibolite- to lower granulite-facies (e.g., Barnes & Prestvik, 2000; Reid, 2004; Yoshinobu et al., 2005). The Rödingsfjäll nappe complex constitutes the lower part of the Uppermost Allochthon and comprises mica schists, quartzites and marbles in greenschist-facies (Gustavson & Gjelle, 1991; Gustavson, 1996; Agyei-Dwarko et al., 2012). The northern central part of the Caledonides hosts mafic and felsic plutons of Caledonian age (Stephens et al., 1985; Barnes et al., 2004; Husdal et al., 2017), which are only poorly studied (Husdal et al., 2017).

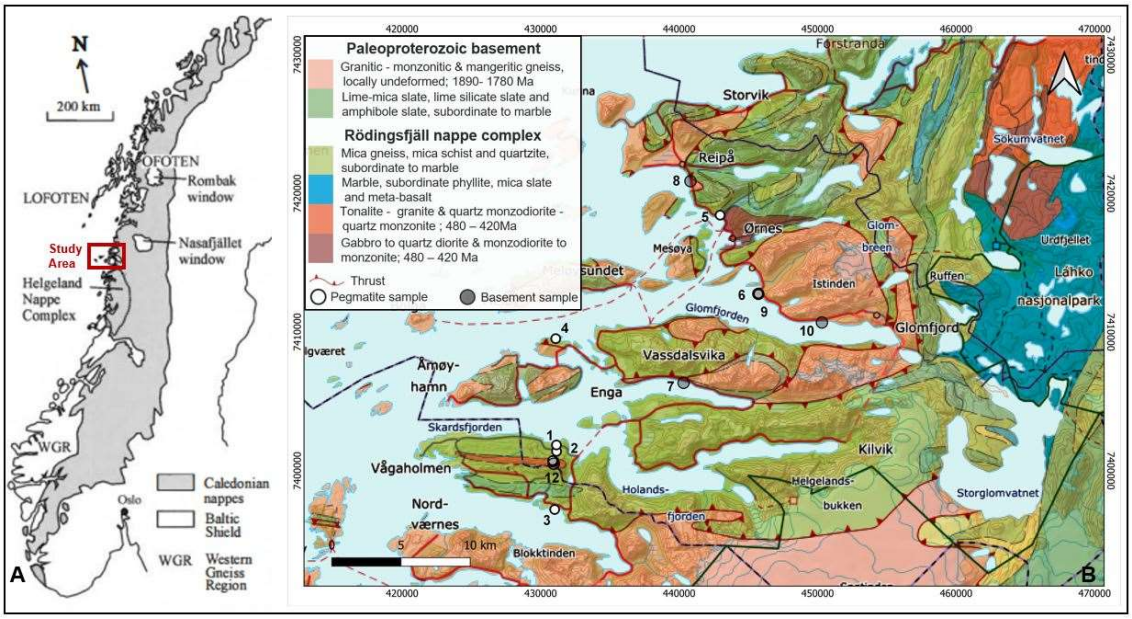

***Figure 3**. A) Geological overview map of Norway. Caledonian nappes, the basement domains and the study area are indicated. Modified from Larsen et al. (2002). B) Geological map of the study area. The sampled locations are indicated and numbered. Pegmatites (1-6) are indicated with white markers and basement locations (7-12) are indicated with grey markers. Sampled locations are: 1) Ågskardet Old Quarry, 2) Ågskardet Upper Body, 3) Ågskardet South, 4) Grønnøya, 5) Ørnes, 6) Neverdalen, 7) Åsjord, 8) Reipå Kleiva Quarry, 9) Neverdalen, 10) Ytre Holten, 12) Ågskardet Upper Body. Base map: NGU's bedrock geology of Norway 1:1 350 000 (2023).*

3.2. The North Helgeland pegmatite field

Ihlen (2004) mapped more than 600 pegmatite bodies and dykes >2 m wide and up to 1000 m long by means of field work and analysis of aerial photographs. They reported a larger number and larger sizes of pegmatite bodies within the Caledonian nappes than in the Paleoproterozoic basement. According to Ihlen (2004), tourmaline only occurs in the pegmatites hosted by Caledonian units, an inference that is not supported by the MSc thesis of Lomotey (2023). Lomotey (2023) did further mapping and sampling of selected pegmatite occurrences in the Glomfjord area. The largest pegmatite bodies in the area are those at Rismålstind, Lysvatn, Bjerangsdalskaret, Solstrand, and Kvina, reaching up to 100 m in width and 1000 m in length (Ihlen, 2004). Within the pegmatite field, occurrences are more numerous toward the west. The grade of metamorphism of the Caledonian cover in the study area also increases toward the west (Ihlen, 2004; Lomotey, 2023). Aside from the LCT-pegmatite at Ågskardet, the pegmatite bodies of Ørnes and Grønnøya are reported to show zonation and enrichment in Be-Li (Grønnøya) and Be-Li-Sn (Ørnes) (Ihlen, 2004; Lomotey, 2023). There are also occurrences of beryl or aquamarine in pegmatites at the contact to basement windows at Storglomvannet and Fykavannet (Müller, 2010). The granitic gneiss of the Høgtuva window is enriched in Be-REE-U-Sn and stream sediments originating from the mostly glacier-covered

Svartisen window show elevated REE concentrations (Müller, 2010). The pegmatites selected for this study are described below.

3.2.1. Ågskardet Old Quarry

The LCT-pegmatite at Ågskardet was mined for coarse-grained muscovite during World War II (Ihlen, 2004). The remains of the small abandoned quarries offer the best outcrop conditions in the otherwise forested area. The pegmatite forms a steep, lenticular body of 36 x 160 m striking WSW-ENE and cuts the foliation of the host rocks at a low angle (Ihlen, 2004). The host rocks are a sequence of polydeformed banded gneisses and migmatitic biotite gneisses (Ihlen, 2004). About 50 m north of the pegmatite body, there is a contact between the banded gneisses and amphibolites (Caixeta Borges, 2023). Ihlen (2004) reported an outer zone that is dominated by plagioclase and contains K-feldspar, both 1-15 cm in size. Interstitial aggregates of quartz together with biotite, muscovite, black tourmaline and garnet occur. The intermediate zone shows an increase in crystal sizes (up to 1 m) and is dominated by K-feldspar. Quartz, muscovite, garnet, black tourmaline and apatite also occur. The contact between these zones commonly displays graphic intergrowth of K-feldspar and quartz (Ihlen, 2004). Ihlen (2004) and Caixeta Borges (2023) suggested a late hydrothermal stage that led to mineralization of rare-metals and to albitization. No evidence of a quartz core has been found in the pegmatite exposures. The U-Pb age for the Old Quarry pegmatite is 387 ± 6 Ma (Lomotey, 2023).

3.2.2. Grønnøya

The occurrence on Grønnøya consists of three N-S trending pegmatite bodies located west of Jektvika. All three bodies have a massive quartz core enclosed by an intermediate zone of blocky K-feldspar, albite and muscovite (Ihlen, 2004; Lomotey, 2023). The wall zone consists of coarse-grained quartz, K-feldspar, albite, garnet, biotite and black tourmaline, some of which display oriented growth (Lomotey, 2023). The border zone consists of quartz and plagioclase (Ihlen, 2004; Lomotey, 2023). The three pegmatite bodies were mined for feldspar during World War II, and also for minor beryl (Adamson & Neumann, 1951; Ihlen, 2004). Lomotey (2023) mapped three additional pegmatite bodies. The old quarries provide the best exposures, and a previously mined body had been chosen for sampling by Lomotey (2023). It has a strike of 010˚N, is ~20 m wide and 70 m long and occurs as a discordant body hosted by amphibolite (Lomotey, 2023). Lomotey (2023) also reports late veins of massive tourmaline with garnet cutting the pegmatite body. For the Grønnøya pegmatite, no U-Pb age was determined.

3.2.3. Ørnes

The pegmatite body is located close to the town of Ørnes and has been described by Ihlen (2004) as possibly zoned and Be-Li-Sn mineralized. The pegmatite forms a cliff on the top of

a steep scree slope and is therefore difficult to examine. The body has a general trend of 030˚NE and is hosted by a partly migmatized amphibolitic gneiss (Lomotey, 2023). Sampling of the pegmatite showed a mineral assemblage of coarse-grained feldspar and quartz with minor amounts of muscovite, garnet, tourmaline and opaque minerals (Lomotey, 2023). Apatite, zircon, monazite and beryl occur as accessory minerals (Lomotey, 2023). Typical pegmatite textures are present in the form of graphic intergrowth between K-feldspar and quartz, and as unidirectional crystallization textures marked by feldspar with quartz-tourmaline pockets forming at the crystallization front of the feldspar (Lomotey, 2023). The body has been dated to 400 ± 7 Ma (Lomotey, 2023).

3.2.4. Ågskardet Upper Body

The upper body at Ågskardet is a lenticular pegmatite body of 50 x 150 m, located about 1 km south of the Ågskardet Quarry. It cuts the paragneiss basement at a 20˚ angle to the main foliation (Lomotey, 2023). The pegmatite contains quartz, K-feldspar, plagioclase and biotite, plus minor amounts of garnet, apatite and tourmaline. Muscovite, zircon and monazite are present as accessory components. Graphic intergrowth of quartz and feldspar has been observed. The poor outcrop conditions did not allow the identification of zoning (Lomotey, 2023). The margins of the pegmatite body are deformed and feldspars show signs of secondary hydrothermal alteration (Lomotey, 2023). U-Pb age dating yielded 412 ± 5 Ma (Lomotey, 2023).

3.2.5. Ågskardet South

This body is described as granitic gneiss with pegmatitic texture (R. Lomotey, personal communication, 2024). It has a mineral assemblage of quartz, plagioclase, K-feldspar, biotite, tourmaline, apatite, and muscovite (Lomotey, 2023). The crystallization age is 400 ± 5 Ma (Lomotey, 2023).

3.2.6. Neverdalen

A pegmatitic dyke at Neverdalen, about 7 km southeast of Ørnes, was emplaced into a shear zone between two contrasting basement rock units, a migmatitic mafic gneiss and a metasedimentary rock unit (Lomotey, 2023). The dyke is about 15 cm wide and appears to be syn-kinematic in origin coinciding with the second foliation of the migmatitic gneiss. It contains quartz, K-feldspar, plagioclase, muscovite, biotite, as well as accessory zircon and opaque phases (Lomotey, 2023). U-Pb zircon age dating yielded 413 ± 2 Ma (Lomotey, 2023).

4. Samples

This study focuses on 13 samples from 6 different pegmatite localities in the Glomfjord area of Helgeland, complemented by 5 representative basement samples from the study area (Tables 1 and 2).

Table 1. *Sample list of the studied pegmatite samples. Where several samples were taken from the same locality, abbreviations or numbers indicate which sample is referred to. Abbreviations: OQ = Old Quarry, UB = Upper Body, S = South.*

Sample ID	Locality	Referred to as	Analyzed minerals	Analytical methods	E	N
RL2207E	Ågskardet Old Quarry	Ågskardet OQ1	Tourmaline, garnet, quartz	EPMA, LA-ICP-MS, SIMS, LF-MS	431138	7401858
RL2208F1	Ågskardet Old Quarry	Ågskardet OQ2	Tourmaline	EPMA, LA-ICP-MS, SIMS	431138	7401858
RL2208F2	Ågskardet Old Quarry	Ågskardet OQ3	Tourmaline	EPMA, LA-ICP-MS, SIMS	431138	7401858
RL2208F3	Ågskardet Old Quarry	Ågskardet OQ4	Tourmaline	EPMA, LA-ICP-MS, SIMS	431138	7401858
111	Ågskardet Old Quarry	Ågskardet OQ5	Tourmaline, (mica)	EPMA, LA-ICP-MS, SIMS	431138	7401858
112	Ågskardet Old Quarry	Ågskardet OQ6	Tourmaline, (mica)	EPMA, LA-ICP-MS, SIMS	431138	7401858
RL2206A	Ågskardet Upper Body	Ågskardet UB1	Tourmaline, garnet, quartz	EPMA, LA-ICP-MS, SIMS, LF-MS, Raman spectroscopy	430960	7400672
RL2216	Ågskardet Upper Body	Ågskardet UB2	Tourmaline, garnet, quartz	EPMA, LA-ICP-MS, SIMS, LF-MS	430865	7400726
2904R	Ågskardet South	Ågskardet S	Garnet	EPMA, LA-ICP-MS, LF-MS	431011	7397201
RL2201A	Grønnøya	Grønnøya	Tourmaline, garnet, quartz	EPMA, LA-ICP-MS, SIMS, LF-MS	431085	7409524
RL2204I	Ørnes	Ørnes 1	Tourmaline	EPMA, LA-ICP-MS, SIMS	442956	7418430
RL2204J	Ørnes	Ørnes 2	Tourmaline	EPMA, LA-ICP-MS, SIMS	442956	7418430
RL2205J	Neverdalen Road Section	Neverdalen	Garnet, quartz	EPMA, LA-ICP-MS, LF-MS	445718	7412753

Table 2. *Sample list of the studied basement samples. Abbreviations: BM = Basement, Q = Quarry, UB = Upper Body.*

Sample ID	Locality	Will be referred to as	Type of rock	Analytical method	E	N

RL2202	Åsjord	Åsjord BM	Granitic TIB gneiss	LF-MS	445718	7412753
RL2203E	Reipå Kleiva Quarry	Reipå Kleiva Q	Granitic TIB gneiss	LF-MS	440814	7420880
RL2205F	Neverdalen Road Section	Neverdalen BM	Mafic TIB gneiss	LF-MS	445718	7412753
RL2213	Ytre Holten	Ytre Holten BM	Granitic TIB gneiss	LF-MS	450310	7410688
2903R	Ågskardet Upper Body	Ågskardet UB BM	Paleoproterozoic paragneiss	LF-MS	430939	7400502

Tourmaline was analyzed from 11 out of the 13 pegmatite samples. Garnet was analyzed in 6 samples, and quartz in 3 samples. Three polished 20 mm tourmaline grain mounts and one polished 20 mm garnet grain mount were prepared (Fig. 4, Table 3). Tourmaline, garnet and quartz mineral separates were prepared primarily for the oxygen isotope work. For the grain mounts, which were produced at Universität Münster by S. Tappe of UiT, grains with ca. 1 mm diameter were used, and for the mineral separates 1-3 mm large grains were handpicked. The grains were handpicked with tweezers under a microscope from crushed and milled rock samples, originally processed during the study by Lomotey (2023). For the grain mounts, milled rock samples in the size range between 0.5 and 1.18 mm were used. For samples that contained both tourmaline and garnet in this grain size fraction, both phases were picked. The mounts contain 6 to 7 grains per sample, mounted in rows, for 9 tourmaline samples (Mount A and B) and 6 garnet samples (Mount D). The third tourmaline mount, Mount C, contains two big tourmaline crystals up to 7 mm in size. These two crystals were provided by Professor Axel Müller and remounted by S. Tappe of UiT. Additionally, tourmaline standards were included into the tourmaline mounts, mainly for the purpose of data quality control during SIMS analyses. The grain mounts were used for EPMA, SIMS, Raman spectroscopy and LA-ICP-MS, whereas the mineral separates were used for laser fluorination MS. Tourmaline samples Ågskardet OQ5 and OQ6 contain mica inclusions or fragments, which were also analyzed by EPMA and LA-ICP-MS. Polished thin sections of the pegmatite samples, made available by Sebastian Tappe of UiT, were used for petrographic characterization. All samples, except for Ågskardet OQ5 and OQ6, were collected by Reginald Lomotey and Sebastian Tappe of UiT in May-June 2022, with support of Kuniko Norge AS. The fieldwork was done within the framework of Reginald Lomotey's MSc thesis project at UiT. Tourmaline samples Ågskardet OQ2, OQ3 and OQ4 are subsamples of the original sample RL2208F, which were subdivided on the basis of color and morphology (Fig. 4). Ågskardet OQ2 consists of dark idiomorphic crystals that may contain quartz inclusions in the cores. The crystals of Ågskardet OQ3 are grey to pale brown in color

and also contain quartz inclusions. Ågskardet OQ4 consists of subhedral dark crystals with quartz inclusions.

Samples 111 and 112 of Ågskardet OQ5 and OQ6 were kindly provided by Professor Axel Müller from the Natural History Museum in Oslo. They are individual idiomorphic tourmaline crystals that were studied in Caixeta Borges (2023) under the original sample names 20324 on mount 111 (OQ5) and 43643 on mount 112 (OQ6). The crystal of Ågskardet OQ5 (7 mm diameter) has a colorless to pale pink core and a narrow green margin with small inclusions of mica and quartz. The crystal of Ågskardet OQ6 consists of mica fragments and pink tourmaline enclosed by a broad dark green tourmaline rim. The Glomfjord basement samples were analyzed in the form of bulk rock powders and belong to the collection of Lomotey (2023). They represent Paleoproterozoic granitic and mafic orthogneisses as well as Paleoproterozoic metasedimentary rocks. The sampling locations are indicated in Figure 3.

.

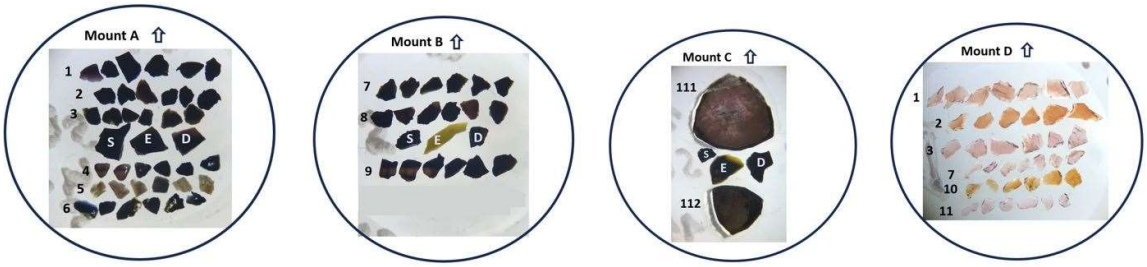

***Figure 4**. Documentation of tourmaline (A, B, C) and garnet (D) grain mounts, not in accurate scale. The numbers refer to localities/sample IDs (see Table 3). The crystals labeled S, E and D in the tourmaline mounts are the schorl (D), elbaite (E), and dravite (S) standards necessary for SIMS analysis.*

***Table 3.** Row IDs of the grain mount documentation and corresponding sample.*

Row ID	Locality	Row ID	Locality
1	Ågskardet OQ1	8	Ørnes 1
2	Grønnøya	9	Ørnes 2
3	Ågskardet UB1	10	Neverdalen
4	Ågskardet OQ2	11	Ågskardet S
5	Ågskardet OQ3	111	Ågskardet OQ5
6	Ågskardet OQ4	112	Ågskardet OQ6
7	Ågskardet UB2		

5. Analytical methods

5.1. Electron microprobe

Major element compositions of tourmaline, mica, quartz, sillimanite and garnet were determined with a JEOL JXA-8530F field emission electron microprobe at Universität Münster in Germany. Operating conditions were 15 kV accelerating voltage, 15 nA beam current and 5 µm beam diameter for the analyses of tourmaline, and 15 kV, 60 nA and 3 µm for garnet analyses. All elements analyzed were measured at 30 and 40 seconds peak counting times for tourmaline and garnet, respectively. The following elements were quantitatively analyzed: Si, Al, Ti, Cr, Fe, Mg, Mn, B, Ca, Ba, Sr, Na, K, Rb, Cs, F, Cl and P for tourmaline and mica, and Si, Al, Ti, Cr, Fe, Mg, Mn, Ca, Na and P for garnet. It must be noted that the very light element Li cannot be quantitatively analyzed by EPMA (Schweizer et al., 2022). Matrix-matched natural and synthetic oxide and silicate reference materials were used for instrument calibration, following Berndt and Klemme (2022) (Table 4). Following the procedure of Flemetakis et al. (2020), F concentrations were corrected for the interference of F and Fe signals, based on previously measured Fe concentrations, and both sets of analyses were merged using the offline-matrix correction feature of the JEOL instrument software. In addition to the quantitative analytical work, back-scattered electron (BSE) imaging and element mapping were performed, with focus on the tourmaline crystals. It must be pointed out that most of the BSE images show a very bright high-atomic-number phase that occupies fractures or forms irregular spots. These domains are residues from the gold coating left after the SIMS analyses due to incomplete removal.

Table 4. *Electron microprobe analytical conditions and materials*

Element	Channel	Diff. crystal	X-ray line	Reference material
F	1	LDE1	Kα	Ast_Topas
Na	2	TAP	Kα	H_Jadeit
Mg	2	TAP	Kα	U_OlivineSanCarlos
Al	2	TAP	Kα	H_DistheneR8
Si	2	PETJ	Kα	U_Hypersthene
K	3	PETJ	Kα	H_SanidineP14
Ca	3	PETJ	Kα	H_DiopsideST48
Cl	4	PETJ	Kα	Ast_Tugtupite
S	4	PETJ	Kα	Ast_Celestite
P	4	LIFH	Kα	U_Apatite_P
Ti	5	LIFH	Kα	Ast_Rutile
Fe	5	LIFH	Kα	U_Fayalite

Cr	5	LIFH	Kα	Ast_Cr2O3
Mn	5	LIFH	Kα	Ast_Rhodonite

Tourmaline structural formulae were calculated normalizing to 31 anions with B = 3 atoms per formula unit (apfu), OH + F = 4 apfu, and Li = 15 – (T + Z + Y) for grains on Mount C. For grains on Mount A and B, the normalization procedure involved T + Z + Y = 15 and OH + F = 4 apfu. The rationale behind the two different normalization procedures are the contrasting Li contents of the sample suites, as measured by LA-ICP-MS. The T + Z + Y = 15 normalization procedure, recommended for igneous tourmaline by Henry et al. (2011), does not allow for calculation of Li content, which is the reason why it was only applied to Mount A and B, where tourmaline crystals contain little or no Li. Both normalization procedures were applied to the SIMS tourmaline standards embedded on the three tourmaline grain mounts (A, B, C) to evaluate the effect of the chosen procedure on the results (Fig. A11). The calculated Li contents were compared to Li contents measured by LA-ICP-MS (Fig. A12). To avoid effects from potential interferences from Ca, Fe, and Mn on B^2O^3 measurements (Cheng et al., 2019), B contents were calculated stoichiometrically.

Mica and garnet recalculations were done on the basis of 22 oxygen equivalents and 8 cations, respectively. For estimations of Li_2O contents in mica, two different approaches were used. For Ågskardet OQ6 and mica inclusion 3 in the crystal from Ågskardet OQ5, the mean Li values determined by LA-ICP-MS were used. For inclusions 1 and 2 from Ågskardet OQ5, the regression equation $0.237 * F^{1.544}$ ($R^2 = 0.852$, n = 501; Tischendorf et al., 1997) was applied, because only two LA-ICP-MS analyses had been carried out, which is insufficient to calculate a meaningful average. The amount of mica Li analyses conducted by LA-ICP-MS was insufficient for establishing a regression equation.

5.2. LA-ICP-MS

Mineral trace element analyses were conducted by LA-ICP-MS at the Universität Münster in Germany, using a 193 nm ArF excimer laser (Analyte G2, Photon Machines) coupled to a ThermoFisher Scientific Element-2 SF-ICP-MS instrument.

Analyses were performed with a laser repetition rate of 10 Hz, a laser fluence of 4 J cm^{-2} and a spot size of 80 µm. For internal standardization of the LA-ICP-MS raw data, ^{29}Si was calibrated against the SiO_2 contents of the minerals analyzed. The SiO_2 contents were determined earlier by EPMA. The following isotopes were measured: ^{7}Li, ^{9}Be, ^{11}B, ^{29}Si, ^{43}Ca, ^{45}Sc, ^{47}Ti, ^{49}Ti, ^{51}V, ^{53}Cr, ^{55}Mn, ^{59}Co, ^{60}Ni, ^{65}Cu, ^{66}Zn, ^{69}Ga, ^{73}Ge, ^{85}Rb, ^{88}Sr, ^{89}Y, ^{90}Zr, ^{93}Nb, ^{95}Mo, ^{118}Sn, ^{121}Sb, ^{133}Cs, ^{137}Ba, ^{139}La, ^{140}Ce, ^{141}Pr, ^{146}Nd, ^{147}Sm, ^{151}Eu, ^{157}Gd, ^{159}Tb, ^{163}Dy, ^{165}Ho, ^{166}Er, ^{169}Tm, ^{172}Yb, ^{175}Lu, ^{178}Hf, ^{181}Ta, ^{182}W, ^{205}Tl, ^{208}Pb, ^{209}Bi, ^{232}Th and ^{238}U. For calibration of

elemental concentrations, the NIST SRM 612 silicate glass was used as the primary standard and the basaltic glasses BIR-1G and BHVO-2G were analyzed as secondary standards. After every 23 sample spot analyses, the standards were measured to monitor data accuracy and precision. Data reduction was performed with the software Glitter 4.4.4. Detection limits for tourmaline, garnet and mica analyses are provided in Appendix B.

5.3. Raman spectroscopy

A Renishaw InVia confocal Raman microscope equipped with a 785 nm (red) diode laser was used to identify the fibrous mineral phase included in the tourmaline samples from Ågskardet UB1. These analyses were conducted at the Department of Physics at UiT in Tromsø, and employed a 100x objective, 10% laser power, and 2x10 seconds measuring time per spot. For processing of the data, the software Renishaw WiRE 5.5.0.22400 was used, and phase identification was performed with the aid of a published Raman spectra library (Lafuente et al., 2015).

5.4. SIMS

The boron isotopic compositions of tourmaline were measured by secondary ion mass spectrometry (SIMS) using the CAMECA 1280-HR instrument at GeoForschungs-Zentrum (GFZ) Potsdam in Germany. Before analysis, the polished grain mounts were ultrasonically cleaned in ethanol and then sputtered with a ~35 nm gold coat. The SIMS instrument was operated in multicollector mode with Faraday cups. The analyses employed a 13 kV, 4 nA primary beam of $^{16}O^-$, which was focused to a ~5 µm spot on the sample surface. Secondary ions were accelerated at 10 kV with no voltage offset. The instrument was operated at a mass resolving power M/ΔM of 2460, sufficient to separate isobaric interference of $^{10}B^1H$ and $^9Be^1H$ on the masses ^{11}B and ^{10}B, respectively. Each analysis consisted of a 70 s 'preburn' to remove the gold coating and establish steady sputter conditions. This was followed by 20 cycles of measurement on ^{10}B and ^{11}B, with 4 s counting time each.

Instrumental mass fractionation (IMF) and analytical quality were monitored by regular bracketing (every 15 analysis points) of samples and three tourmaline reference materials (schorl, dravite, elbaite; described by Leeman & Tonarini, 2001). The internal precision of a single analysis (20 cycles) was typically 0.1‰. The repeatability (1σ /mean) of multiple analyses of the same tourmaline reference was between 0.38 and 0.97‰ for schorl, dravite and elbaite. A slight chemical matrix effect among the three tourmaline reference materials is inferred from the differences in IMF values: schorl = 0.976445 (Mount A), 0.975864 (Mount B), 0.976337 (Mount C); dravite = 0.978177 (Mount A), 0.976732 (Mount B), 0.977253 (Mount C); and elbaite = 0.977165 (Mount A), 0.976781 (Mount B), 0.976755 (Mount C). The average IMF factor derived from all analyses of reference tourmaline crystals was used to correct the data

(0.976788, n = 213). The corresponding repeatability (1σ/mean = 0.91‰) is taken as an estimate of the total analytical error for the data collected during the analytical session from 6 to 8 December 2023. The IMF-corrected $\delta^{11}B$ values were calculated relative to NIST SRM 951 as $\delta^{11}B = 0$ using the $^{11}B/^{10}B$ ratio of 4.04362 +/- 0.00137 (Catanzaro et al., 1970).

5.5. Laser fluorination mass spectrometry

Several mg of individual garnet and quartz crystals with a size range from 0.5 to 3 mm were handpicked for triple oxygen isotope analysis by laser fluorination mass spectrometry. Analyses on garnet were done for the following samples: Ågskardet OQ1, Ågskardet UB1, Ågsakrdet UB2, Ågskardet S, Grønnøya and Neverdalen. Quartz grains were analyzed from Ågskardet OQ1, Ågskardet UB1, Ågskardet UB2, Grønnøya and Neverdalen. Additionally, 5 powdered bulk rock samples from the Paleoproterozoic basement were analyzed. Oxygen was extracted from the silicate samples as O_2 by laser fluorination, with BrF_5 as the fluorinating agent. The analyses were conducted by Dr. Stefan Peters at the University of Göttingen in Germany following the procedure of Pack et al. (2016). To remove contaminations by other gases, freeze-thaw techniques and liquid nitrogen in combination with a 5 Å mesh molecular sieve and a gas chromatograph were used. The purified sample oxygen was then transferred at 65°C into a MAT253Plus gas-source mass spectrometer. The oxygen isotopic compositions of the sample gases were measured as m/z = 32, 33, and 34 relative to a reference gas calibrated against Vienna Standard Mean Ocean Water 2 (VSMOW2). For reproducibility testing, the San Carlos olivine was used as a reference material (Pack et al., 2016). The oxygen isotope ratios $^{17}O/^{16}O$ and $^{18}O/^{16}O$ were measured and are expressed as $\delta^{17}O$ and $\delta^{18}O$, which are the respective per mil deviations from VSMOW2 (McKinney et al., 1950). The parameter Δ′17O describes the ppm deviation of a sample's δ′17O from its δ′18O in linearized triple oxygen isotope space. The slope of the reference line used here is 0.528 after Sharp et al. (2018). The $\Delta'17O_{0.528}$ values for the samples are reported relative to VSMOW2, using the calibration of San Carlos olivine on the VSMOW2 scale by Pack et al. (2016)

5.6. Oxygen isotope thermometry

Employing the results from laser fluorination mass spectrometry, apparent crystallization temperatures were calculated using the relationship:

$$1. \quad \Delta^{18}O_{(Qz-Grt)} \approx 10^3 \ln[\alpha_{(Qz-Grt)}] = [A_{(Qz-Grt)} 10^6]/T^2, \qquad (4)$$

where $\Delta^{18}O_{(Qz-Grt)}$ is the equilibrium fractionation between quartz and garnet, $\alpha_{(Qz-Grt)}$ is the fractionation factor, T is the equilibrium temperature in degrees K, and the coefficient A is equal to $\Delta^{18}O$ at 1000 K. In this equation, it is assumed that $\Delta^{18}O$ varies linearly against $1/T^2$, which is commonly assumed for mineral systems above 600°C (Chacko et al., 2001), i.e., at

magmatic conditions. Thus, some caution is warranted when applying this relationship to evolved pegmatite magmatic-hydrothermal systems. Another factor of uncertainty is the coefficient A. The empirically determined value of 2.71‰ K^2 for almandine-rich garnet was employed, which had been calibrated at slightly higher temperatures than those expected for garnet crystallization from pegmatite-forming magma (Valley et al., 2003). The coefficient A also varies with cation substitution. For grossular garnet, Valley et al. (2003) reported an experimental value of 3.03‰ K^2. Effects by Fe^{2+} to Mg^{2+} substitution between almandine and pyrope are negligible (Rosenbaum & Mattey, 1995), as are substitution effects by Ca^{2+} to Mn^{2+} between grossular and spessartine (Lichtenstein & Hoernes, 1992). Among the studied garnets, only Neverdalen garnets are dominated by [Grs + Sps] in composition (78 mol.%). All other garnet samples have [Alm + Prp] ≥ 51.4 mol.%. Effects by the substitution of Fe^{3+} for Al^{3+} are slightly larger, but the andradite component of the studied samples is very small and therefore negligible. Linear interpolation between A-values results in a range of A = 2.76‰ K^2 to A = 2.96‰ K^2 for the garnets studied. To keep the dataset consistent, A= 2.71‰ K^2 is employed for thermometry calculations on all samples.

5.7. Petrography

For petrographic descriptions and photomicrographs, the polarization microscope Leica DM4500 P was used to study polished thin sections. For Ågskardet S, Ågskardet OQ5 and OQ6, and Ørnes 1, no thin sections were available. BSE images were taken for the three tourmaline grain mounts to guide subsequent analyses using the Hitachi TM3030 Tabletop Microscope SEM at UiT. The sample mounts were carbon coated before analysis in full vacuum. Additional BSE images were taken during EPMA work in Münster, Germany.

6. Results

6.1. Petrographic features of tourmaline and garnet

Tourmaline and garnet are common minor minerals in these pegmatitic samples, but not all samples contain both minerals. The results for tourmaline and garnet are summarized in Table 5 and Table 6, respectively.

6.1.1. Ågskardet OQ1

In the old quarry of Ågskardet, textures vary between the different samples. The sample RL2207E from Ågskardet OQ1 is taken from a layered portion of the pegmatite body. In thin section, a garnet-rich layer is separated from a tourmaline-rich layer. The interstitial spaces between garnet and tourmaline crystals, and in between garnet and tourmaline layers are filled

by quartz, plagioclase, K-feldspar and small amounts of white mica. Some of the quartz is deformed and dynamically recrystallized. Garnet forms subhedral, mostly rounded crystals up to 15 mm in size. Up to 12 mm large tourmaline crystals are blue in color and often poikilitic with quartz inclusions (Fig. 5A). Many of the subhedral to anhedral crystals show a distinct core and rim (Fig. 5B) with strong pleochroism from blue to violet. The modal abundance of both tourmaline and garnet is about 25 vol.%.

6.1.2. Ågskardet OQ2-4

The tourmaline of Ågskardet OQ2, OQ3 and OQ4 forms a breccia together with quartz, plagioclase, K-feldspar and small amounts of white mica in one of the two thin sections (Figs. 5C and 5D). The breccia indicates brittle deformation. Many of the euhedral to subhedral crystals are fractured, poikilitic with quartz inclusions, and show compositional zoning from core to rim (Fig. 5C and 5D). They are of blue-green color and up to 2 mm in size. The quartz inclusions were confirmed by EPMA. The modal abundance of tourmaline is about 5 vol.%. No garnet is present. Adjacent to the tourmaline breccia, there is a cumulation of large, blocky albite crystals up to 20 mm in diameter. They are partly strongly sericitized and contain inclusions of K-feldspar and white mica. The second thin section of Ågskardet OQ2-4 displays elongated pale blue crystals of tourmaline up to 15 mm long. These crystals are intergrown with quartz, forming elongated lamellae. This skeletal intergrowth is also seen in BSE images from Ågskardet OQ3 (Fig. 5E). The thin section is dominated by albite (>70 vol.%) and quartz, with smaller amounts of K-feldspar and white mica. Albite forms large crystals (30 mm) and encloses optically continuous microcline. This replacement texture suggests that the albite is secondary. Along fractures in albite, there are fine-grained phyllosilicates and the albite is sericitized, which are further signs of hydrothermal alteration.

6.1.3. Ågskardet UB1

The sample RL2206A from Ågskardet UB1 contains garnet and brown-green tourmaline, which both show abundant inclusions of acicular to fibrous sillimanite (Fig. 6A). The included phase was confirmed as aluminum silicate by EPMA and more specifically as sillimanite by Raman spectroscopy (Fig. A8). For garnet, the sillimanite inclusions concentrate in the rims and are overall less abundant, whereas in tourmaline the sillimanite needles are continuously included. The Ågskardet UB1 sample is sheared and deformed. Tourmaline and garnet crystals are often in direct contact, with tourmaline forming tails on the euhedral, >10 mm large, porphyroclastic garnet crystals. The modal abundance of garnet is about 5 vol.% and of tourmaline about 2-3 vol.%. Other main constituents are quartz, K-feldspar and albite. There is little biotite and white mica (<2 vol.%), which is severely altered. K-feldspar and albite are intergrown with or partly replaced by sillimanite.

6.1.4. Ågskardet UB2

The sample RL2216 from Ågskardet UB2 contains anhedral poikilitic and fractured brown tourmaline (<1 vol.%), as well as subhedral garnet (3 %), surrounded by quartz (25 %) and K-feldspar (60 %), with minor amounts of albite, biotite, and other accessories. K-feldspar shows perthitic exsolutions, which indicates crystallization at higher temperatures in a relatively dry system. Several albite crystals show myrmekitic textures. Fractures in garnet are filled by biotite.

6.1.5. Grønnøya

Sample RL2201A from Grønnøya shows a mineral assemblage of mainly albite, K-feldspar (microcline), quartz and white mica, with subhedral garnet (5 vol.%) and subhedral to anhedral tourmaline (15 %). Quartz fills interstitial space, which indicates late crystallization relative to the other minerals. Garnet is partly intergrown with white mica. White mica shows intergrowth structures with K-feldspar; both are optically continuous. Some crystals of white mica have recrystallized edges. Tourmaline has blue cores, dark blue outer cores and brown rims with concentric zoning. Some tourmaline crystals show poikilitic texture and inclusions (optically continuous mica, microcline and albite; Fig. 6B). Tourmaline is enclosing parts of an albite crystal that is optically continuous outside of the tourmaline, which suggests late replacement of the original mineral assemblage by tourmaline. Albite is often sericitized and some K-feldspar crystals show perthitic exsolutions. Some of the tourmaline crystals are elongated reaching 13 mm in length. Garnet shows replacement by fine-grained radial aggregates of chlorite along fractures.

6.1.6. Ørnes 2

Sample RL2204J from Ørnes 2 contains large anhedral crystals of tourmaline (9 mm) and ‘nests’ of euhedral to subhedral tourmaline, euhedral garnet and some accessories surrounded by quartz (35 vol.%), large crystals of partly sericitized albite (55 %), white mica and K-feldspar. Some of the quartz is dynamically recrystallized. The tourmaline is dark blue-brown and has a modal abundance of 3 vol.%. Some crystals are poikilitic and fractured. Garnet has a modal abundance of <2 vol.%.

Table 5. *Summary of the microscopic features of the studied tourmalines.*

Locality	Texture	Abundance	Zoning	Size
Ågskardet OQ1	Subhedral, often poikilitic	25 vol.%	Concentric	1 mm - 12 mm
Ågskardet OQ2-4	Euhedral - subhedral, often poikilitic; fractured	5 vol.%	Concentric	0.1 - 2 mm (brecciated); elongated 15 mm
Ågskardet OQ5	Euhedral	Whole crystal	Concentric (rim)	7 mm
Ågskardet OQ6	Euhedral, majority of the core consists of mica fragments	Whole crystal	Concentric (rim)	4 mm
Ågskardet UB1	Anhedral in aggregates, fractured, sheared, abundant sillimanite inclusions	2-3 vol.%	None	0.1 - 10 mm
Ågskardet UB2	Anhedral, poikilitic, fractured	<1 vol.%	None	0.3 – 3 mm
Grønnøya	Subhedral – anhedral, often poikilitic	15 vol.%	Concentric, diffuse	0.5 mm - 13 mm
Ørnes 2	Euhedral - anhedral	5 vol.%	None	0.1 mm to 9 mm

Table 6. Summary of the microscopic features of the studied garnets.

Locality	Texture	Abundance	Zoning	Size
Ågskardet OQ1	Subhedral, rounded	25 vol.%	None	Up to 15 mm
Ågskardet UB1	Euhedral, porphyroclastic, abundant sillimanite inclusions in the rims	5 vol.%	None	Up to 12 mm
Ågskardet UB2	Subhedral, fractured	3 vol.%	None	Up to 7 mm
Grønnøya	Subhedral	5 vol.%	None	Up to 5 mm
Ørnes 2	Euhedral	<2 vol.%	None	Up to 4 mm
Neverdalen	Subhedral, fractured	2 vol.%	None	Up to 5 mm

6.1.7. Neverdalen

The mineral assemblage of the Neverdalen pegmatite is dominated by plagioclase (60 vol.%), K-feldspar (10 %) and quartz (10 %). Other constituents are biotite (5 %), garnet (2 %), an opaque phase (determined as hematite with minor magnetite and rutile by Raman spectroscopy, 5 %), and allanite (<1 %). Garnets occur as subhedral fractured crystals.

6.1.8. Ågskardet OQ5-6

BSE images of Ågskardet OQ5 show a distinct compositional zoning. The rim is sharply distinct from the core and then diffusely changes composition towards the interior (Fig. 6E). The sharp rim may follow after a resorption event. The core hosts quartz and mica inclusions.

The core of Ågskardet OQ6 consists almost exclusively of mica fragments (Fig. 6F). In between the mica fragments are ‘islands’ of tourmaline. Tourmaline of different compositions fills cracks within mica and tourmaline. The mica fragments and tourmaline components of the core are overgrown by a distinctly different tourmaline rim. Within the rim, compositional zoning is observed. The gradations between different tourmaline compositions suggest they represent several generations of tourmaline growth, and the rather unique texture of the crystal may indicate hydrothermal replacement of tourmaline by mica, and subsequently beginning replacement of mica by tourmaline.

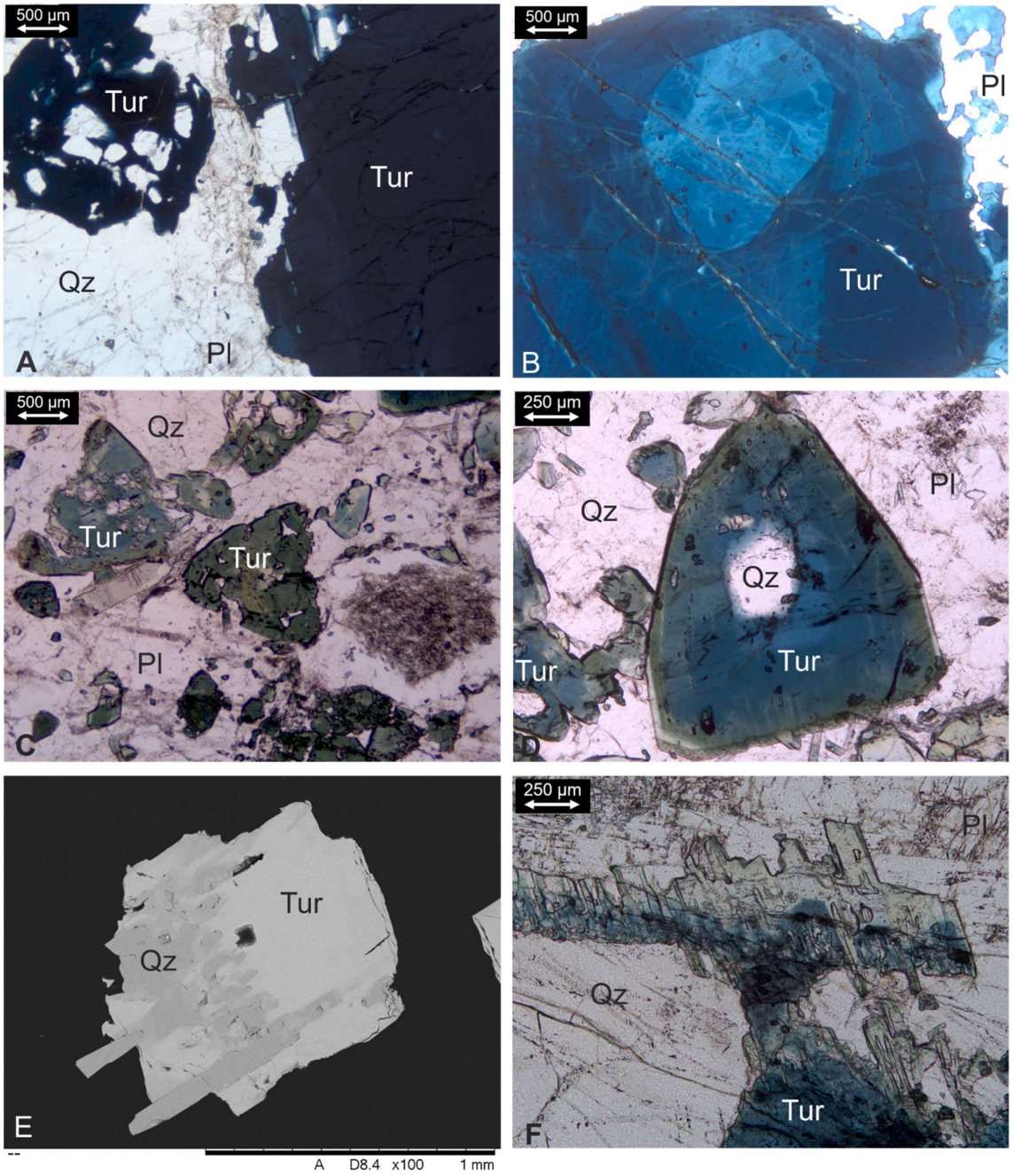

Figure 5. *Photomicrographs and BSE images of tourmaline from the study area. Abbreviations: Tur = tourmaline, Qz = quartz, Pl = plagioclase (Warr, 2021). A) Poikilitic tourmaline from a tourmaline layer, Ågskardet OQ1. PPL. B) Color zoning between core (lighter blue) and rim (dark blue) of a tourmaline crystal from Ågskardet OQ1. PPL. C) Tourmaline – quartz – feldspar -breccia with fractured euhedral crystals of tourmaline, Ågskardet OQ2, OQ3, OQ 4. PPL. D) Euhedral crystal of tourmaline with quartz inclusion in the core. Color zoning from core (blue) to outer rim (blue-green). PPL. E) Skeletal intergrowth of tourmaline and quartz, Ågskardet OQ 2. BSE. F) Skeletal crystal of tourmaline intergrown with quartz next to albite, Ågskardet OQ2, OQ3, OQ4. PPL.*

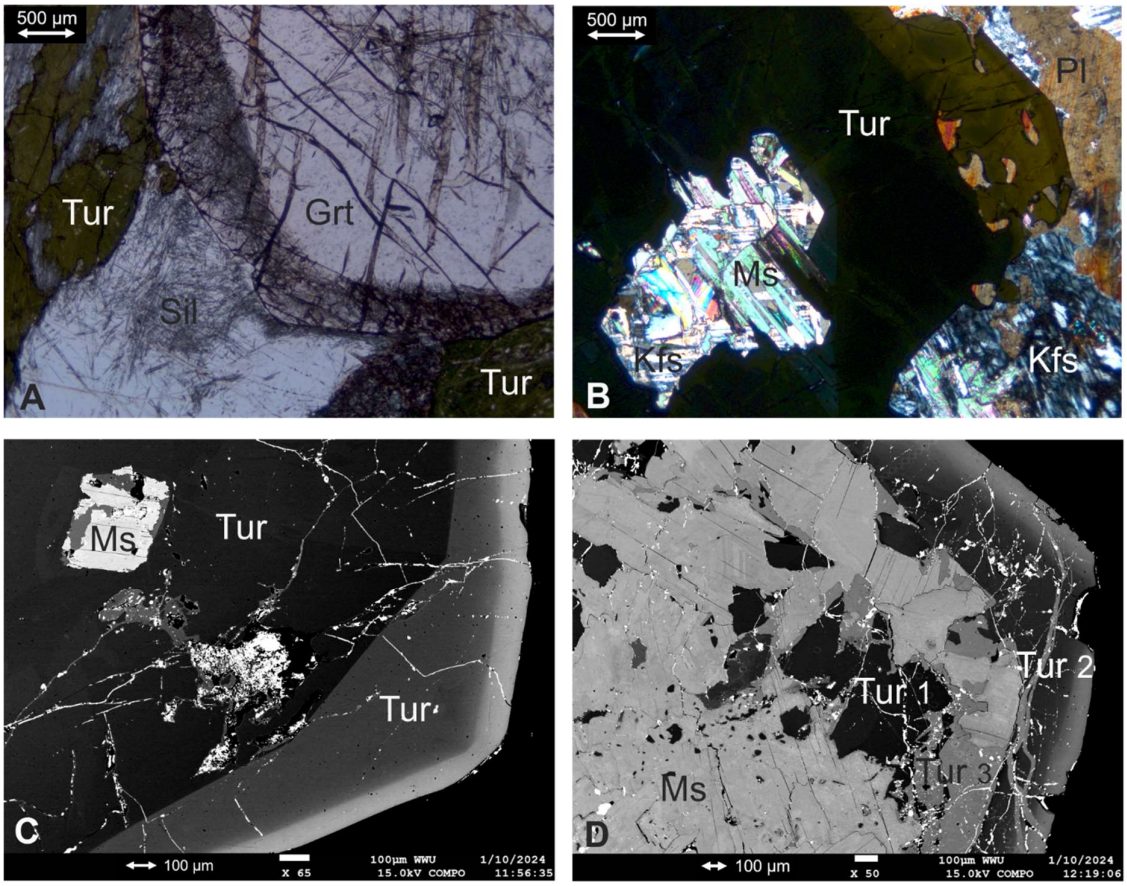

Figure 6. *Photomicrographs and BSE images of tourmaline and garnet of the study area. Abbreviations: Tur = tourmaline, Qz = quartz, Pl = plagioclase, Kfs = K-feldspar, Ms = muscovite, Grt = Garnet, Sil = sillimanite (Warr, 2021). A) Sillimanite inclusions in tourmaline, garnet and quartz from Ågskardet UB 1. Garnet and tourmaline are in direct contact, the sample is sheared. PPL. B) A dark blue crystal of tourmaline with brown rims showing poikilitic structure and mica and alkalifeldspar inclusions. The inclusions are optically continuous with crystals adjacent to the tourmaline. The strong mineral color of the tourmaline masks interference color. Grønnøya, XPL. C) Sharp core-rim contact in euhedral tourmaline crystal, Ågskardet OQ5. D) Aggregate consisting of mica fragments and a first generation of tourmaline (Tur 1), enclosed by a rim of second-generation tourmaline (Tur 2) and replaced along cracks by a third generation of tourmaline (Tur 3). Ågskardet OQ6.*

6.2. Tourmaline major and trace element compositions

Complete tourmaline major element compositions are listed in Appendix C. The trace element data set is provided in Appendix B. Some 271 major element analyses were carried out on tourmaline by EPMA and 215 trace element analyses by LA-ICP-MS. Following the classification of Henry et al. (2011), the majority of tourmalines studied here plot as alkali group, with the exception of a measurement from Ågskardet OQ1, which plots at the limit to X-vacant, and a measurement from Ågskardet OQ6, which plots as a member of the calcic group (Fig. 7). Within the alkali group, schorl compositions are dominant. Other compositions are found in tourmalines from Ågskardet UB1 and UB2, which mostly plot as dravite, with some of the rims showing schorl compositions (Fig. 7), and in several crystals from the old quarry in Ågskardet.

Tourmalines from Ågskardet OQ2, OQ3, and OQ4 vary from schorl to fluor-schorl. Following Henry et al. (2011), the tourmaline compositions from Ågskardet OQ5 can be identified as tsilaisite (11 analyses), fluor-schorl (7), elbaite (7), fluor-elbaite (4) and schorl (4). The remaining 4 out of the 36 analyses would classify as fluor-tsilaisite, a species that was only described in 2015 by Bosi et al. and is therefore not included in the classification of Henry et al. (2011). It is Mn-dominant on the Y site and contains more than 0.5 apfu F on the W site. The tourmaline compositions from Ågskardet OQ6 were identified as fluor-schorl (16 analyses), fluor-elbaite (15), schorl (9), 'fluor-tsilaisite' (9), elbaite (7), tsilaisite (3) and fluor-liddicoatite (1).

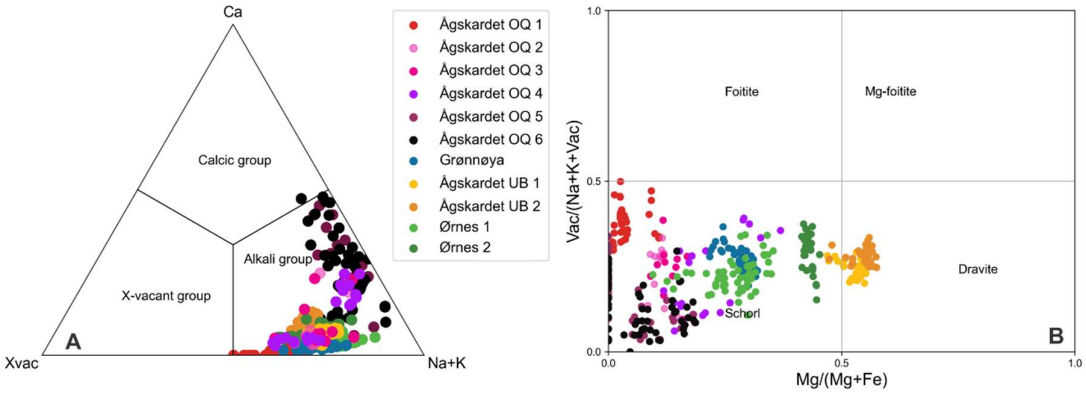

Figure 7. *Tourmaline classification according to Henry et al. (2011) based on A) Ternary diagram of primary groups after X site occupancy. All analyses except for one plot as alkali group. B) Vacancy / (Na + K + Vacancy) vs. Mg / (Mg + Fe). The majority of tourmaline from Ågskardet UB 1 and UB 2 plot as dravite. This classification does not identify Li-rich endmembers.*

The overall large variation in major element chemical composition displays a divide between the less evolved pegmatites Ågskardet UB, Grønnøya, and Ørnes, and the more evolved Ågskardet Old Quarry. The less evolved pegmatites show narrow compositional ranges in both major and trace elements, whereas the evolved pegmatite shows a large compositional range at only little overlap with the less evolved pegmatites. The 'least evolved' sample of the zoned pegmatite exposed in the old quarry at Ågskardet (OQ1) shows similarities to the simpler pegmatites but has lower Mg contents.

Within the sample population from Ågskardet Old Quarry, a trend of increasing F, Mn, Ca, Al, Fe/(Fe+Mg), Li and decreasing Mg-Fe emerges (Figs. 8, 9), with tourmalines from Ågskardet OQ1 containing more Fe and less Li and tourmalines from Ågskardet OQ5 and OQ6 containing more F, Mn Ca, Al and Li. The most primitive pegmatites contain the highest amounts of Mg and Fe on the Y site. With increasing evolution, Mn^{2+} as well as (Li^{+} + Al^{3+}) replace Fe^{2+} and Mg^{2+}. In the X site, Ca^{2+} replaces Na^{+}, which is charge-balanced by a greater ratio of Li^{+} to Al^{3+} in the Y site. Fluorine replaces OH^{-} in the W site. In these samples, Mn ranges from 0 to 0.7

apfu and Ca from 0 to 0.5 apfu. In the rims of tourmalines from Ågskardet OQ5 and OQ6, the increase in Ca is accompanied by an increase in REE and Fe, Ti and Mg (Figs. 18, A1, A2, A5, A6 and A7). The location of the measured profiles for the crystals from localities Ågskardet OQ5 and OQ6 are indicated in Figures A3, A10 and 19, A4 for OQ5 and OQ6, respectively.

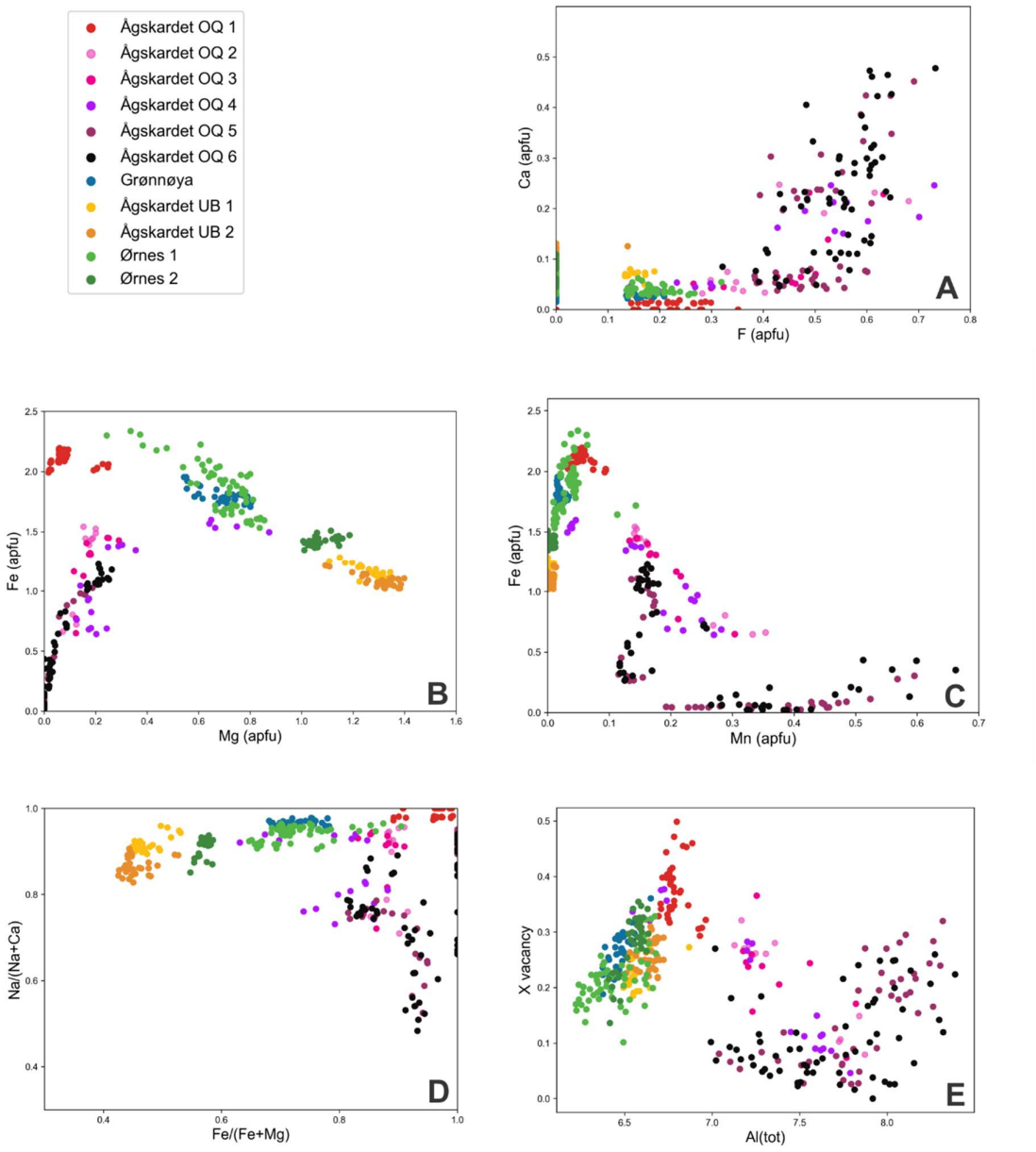

Figure 8. *Chemical composition of tourmaline. A) Ca vs. F (apfu) diagram. B) Fe vs Mg (apfu) diagram. C) Fe vs. Mn (apfu) diagram. D) Na / (Na + Ca) vs. Fe / (Fe + Mg) diagram. E) X vacancy (apfu) vs. Al_{tot} (apfu) diagram.*

The Al contents range from 6.2 to 8.4 apfu (Fig. 8E). There is a positive correlation between the total Al and the X vacancy for tourmaline from the less evolved pegmatites, including

Ågskardet OQ1. This can be explained by foitite substitution ($^{Y}R^{2+} + {}^{X}R^{1+}$) = ($^{X}vac + {}^{Y}Al$); R = cation. The Al_{tot} content in tourmaline from Ågskardet OQ2 to OQ6, ranging from 7.0 to 8.4 apfu, outranges the beforementioned correlation. These values and elevated Li contents (Fig. 9A) are consistent with elbaite substitution, where ($Li^{+} + Al^{3+}$) fill the Y site instead of (Mg^{2+}, Fe^{2+}).

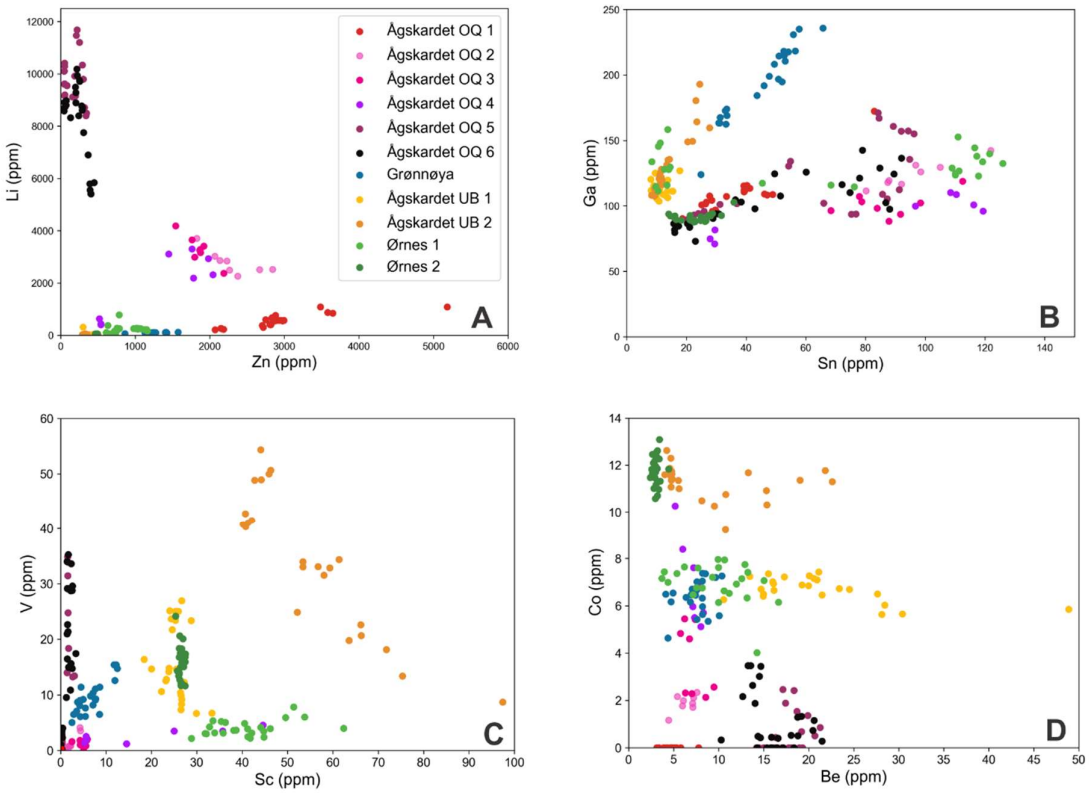

Figure 9. *Trace element composition of tourmaline. A) Li (ppm) vs. Zn (ppm) diagram. B) Ga (ppm) vs. Sn (ppm) diagram. C) V (ppm) vs. Sc (ppm) diagram. D) Co (ppm) vs. Be (ppm) diagram.*

For Ågskardet UB, Grønnøya, and Ørnes, the Li contents of tourmaline are very low and range mostly between 15 and 250 ppm, with some single spot analyses showing higher values of up to 780 ppm (Ørnes 1; Fig. 9A). Tourmaline from Ågskardet OQ1 ranges from 209 to 1086 ppm in Li concentration. Analyses from Ågskardet OQ2, OQ3 and OQ4 cluster between 2190 and 4190 ppm Li, with a few outliers between 330 and 640 ppm. Tourmalines from Ågskardet OQ5 and OQ6 show elevated Li contents, ranging from 5555 ppm to 10183 ppm for OQ6 and from 8501 ppm to 11678 ppm for OQ5. Zn contents range from 0 to 1573 ppm for Ågskardet OQ5 and OQ6, Ågskardet UB, Grønnøya and Ørnes, with each locality forming its own data cluster (Fig. 9A). Tourmalines from Ågskardet OQ2, OQ3 and OQ4 contain, excluding outliers, 1450 to 2840 ppm Zn. Values for Ågskardet OQ1 range from 2071 to 5185 ppm Zn. In terms of V and Sc contents, all localities range between 0 and 54 ppm (V) and 0 and 97 ppm (Sc). The

highest concentrations of both elements are present in tourmaline from Ågskardet UB2 (Fig. 9C). For all localities except for Ågskardet OQ5 and OQ6, the V/Sc ratio is between 0 and 2.5, while Ågskardet OQ5 and OQ6 show ratios up to 24. Be contents for all samples range between 4 and 30 ppm, with one outlier at 49 ppm, which was measured in a rim from Ågskardet UB1 (Fig. 9D). For the localities that show the lowest values, the occurrence of beryl and / or other Be-minerals has been reported.

Importantly, the Pb and Sr contents mark a clear distinction between Ågskardet OQ5 and OQ6 and the rest of the samples. Ågskardet OQ5 and OQ6 have elevated contents of both Sr (132 to 327 ppm) and Pb (32 to 277 ppm). Ågskardet OQ1-4, Ågskardet UB, Grønnøya and Ørnes vary between 0 to 27 ppm Sr and 0 to 12 ppm Pb. In Ågskardet OQ5, the tourmaline core is richer in Pb, whereas the rim is richer in Sr (Fig. 10). The same trend also holds for Ågskardet OQ6. Gallium and Sn contents show variation within the samples (Fig. 9B). Values range from 68 to 236 ppm (Ga) and 8 to 126 ppm (Sn). Ørnes 1 shows the largest variation in Sn, with a bimodal distribution of values clustering around 9 -14 ppm and 110 -126 ppm. Ørnes 1 shows the largest variation in Sn, with a bimodal distribution of values clustering around 9-14 ppm and 110-126 ppm. Most of the high values were measured in rims and most of the low values come from the cores. Analyses of trace elements in the tourmaline crystal of Ågskardet OQ5 show elevated Rb and Cs contents close to a mica inclusion (Fig. A10). Figure 11 displays chondrite-normalized REE patterns for the studied tourmalines. For all samples, normalized REE concentrations decrease from LREE to HREE and are generally very low. For Grønnøya, Ågskardet OQ1, 3, 5 and 6, concentrations mostly were below detection limit. The tourmaline crystals from Ågskardet OQ5 and 6 show an increase in LREE (La to Sm) in the rim (Fig. A1).

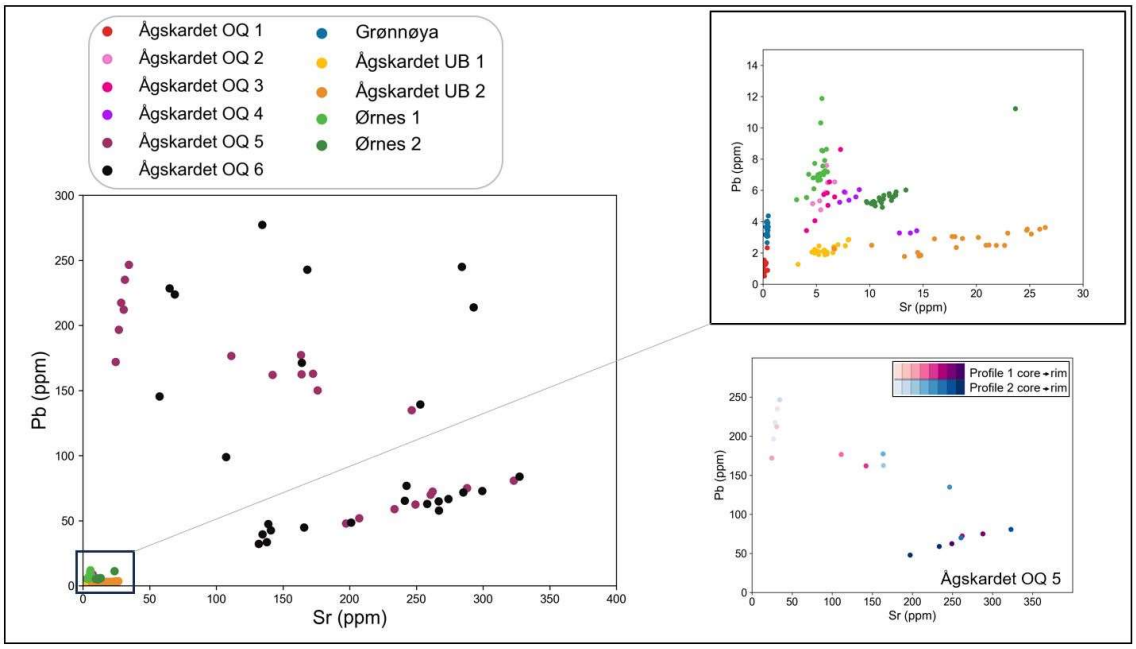

Figure 10. *Pb vs. Sr diagram for tourmaline. Samples from Ågskardet OQ5 and OQ6 show significantly higher concentrations than the other samples. Core-rim profiles from Ågskardet OQ5 show the core rich in Pb with decreasing concentration towards the rim, and an opposite trend for Sr.*

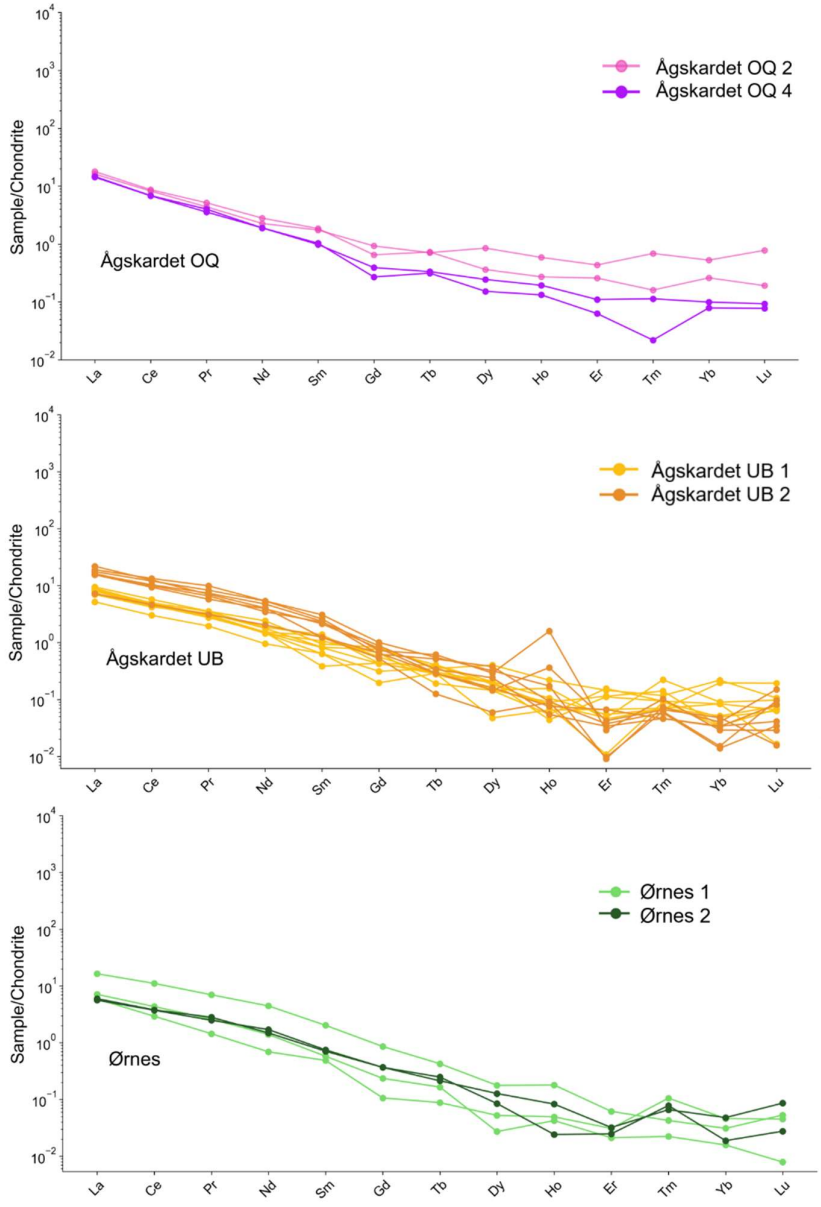

Figure 11. *Chondrite-normalized REE patterns for tourmaline from the sampled localities. Normalized to chondrite values published by Palme and Jones (2003). For Grønnøya, Ågskardet OQ1, OQ3, OQ5 and OQ6, no sufficient data was retrieved (analyses below detection limit).*

6.3. Garnet major and trace element compositions

Complete garnet major element compositions are listed in Appendix C. The trace element data set is provided in Appendix B. A total of 117 EPMA spot analyses and 114 LA-ICP-MS spot analyses of garnets from Ågskardet OQ1, Ågskardet UB1 and UB2, Ågskardet S, Grønnøya and Neverdalen were carried out. Garnets analyzed are dominated by either almandine (Ågskardet UB1, UB2, S, OQ1 and Grønnøya) or spessartine (Neverdalen, Fig. 12). Almandine and spessartine components sum up to more than 80 mol.% for most samples, and 96 mol.%

and 98 mol.% for Grønnøya and Ågskardet OQ1, respectively. Ågskardet OQ1 shows the largest range in composition, from 40 to 65 mol.% spessartine, and from 58 to 34 mol.% almandine. Ågskardet UB1 and UB2 garnets contain 13-14 mol.% pyrope component, and Neverdalen garnet has a grossular component of 11 mol.%. The ratio of MnO to FeO + MnO is highest for Neverdalen garnet, followed by Ågskardet OQ1 and Grønnøya garnets (Fig. 13). This ratio is an indicator for the degree of fractionation of pegmatite-forming magmas (Müller et al., 2012). Another indicator for the stage of evolution of pegmatite magmas is the relationship MnO + CaO vs. FeO + MgO (Fig. 13), with increasing MnO + CaO indicating more evolved magmas (Baldwin & von Knorring, 1983; Moretz et al., 2013). Neverdalen garnet contains the highest MnO + CaO contents of 35.7 wt.%, followed by Ågskardet OQ1 and Grønnøya garnets. Garnet from Ågskardet UB2 contains only 6.3 wt.% MnO + CaO and 35.5 wt.% FeO + MgO. Some of the garnet crystals show increasing MnO + CaO towards the rims, but there is no clear global pattern emerging, which may be due to the rather limited number of analyses per crystal (n=3).

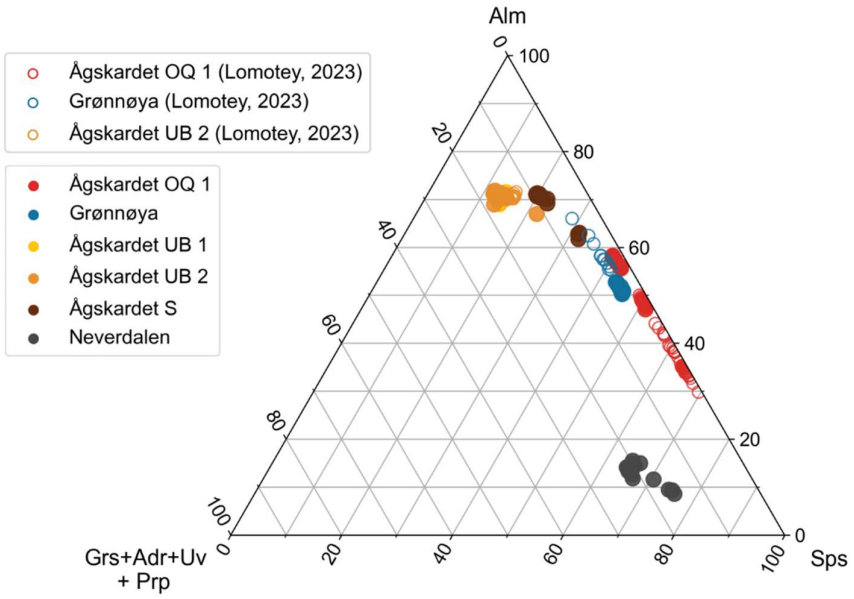

Figure 12. *Chemical composition of garnet in a ternary diagram of almandine vs. spessartine vs. grossular + andradite + uvarovite + pyrope. Full circles display the analyses from this study and half circles show data from Lomotey (2023) for the same localities.*

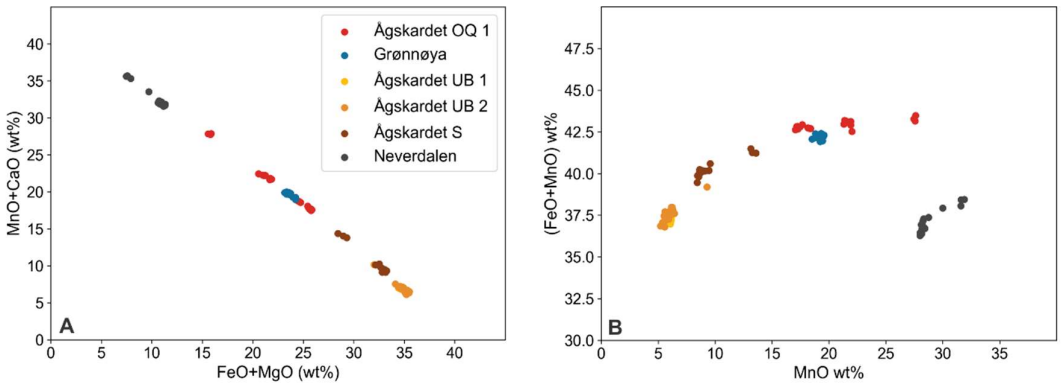

Figure 13. *Chemical composition of garnet. A) MnO + CaO vs. FeO + MgO diagram. B) (FeO + MnO) vs. MnO diagram.*

The garnet Li contents vary from 24 ppm (Neverdalen) to 203 ppm (Ågskardet OQ1, Fig. 14). These two samples also display the most extreme Y contents, with 4680 ppm for Neverdalen and Ågskardet OQ1 ranging from below detection limit at 0.11 ppm to 11 ppm. Grønnøya garnet clusters around 1000 ppm Y and 175 ppm Li, and garnets from Ågskardet UB1, UB2 and S show increasing Li and Y contents from 25 ppm Li and 500 ppm Y towards 80 ppm Li and 2100 ppm Y. One analysis of Ågskardet UB2 garnet reaches 2835 ppm Y. Ta and Nb contents are highest for Grønnøya and Ågskardet OQ1, up to 17 ppm Nb, 13 ppm Ta and 10 ppm Nb, 6 ppm Ta, respectively (Fig. 14B). In Figure 15, the ∑REE, Y, Sc and P contents of garnets are compared to literature data for different types of pegmatites and granites.

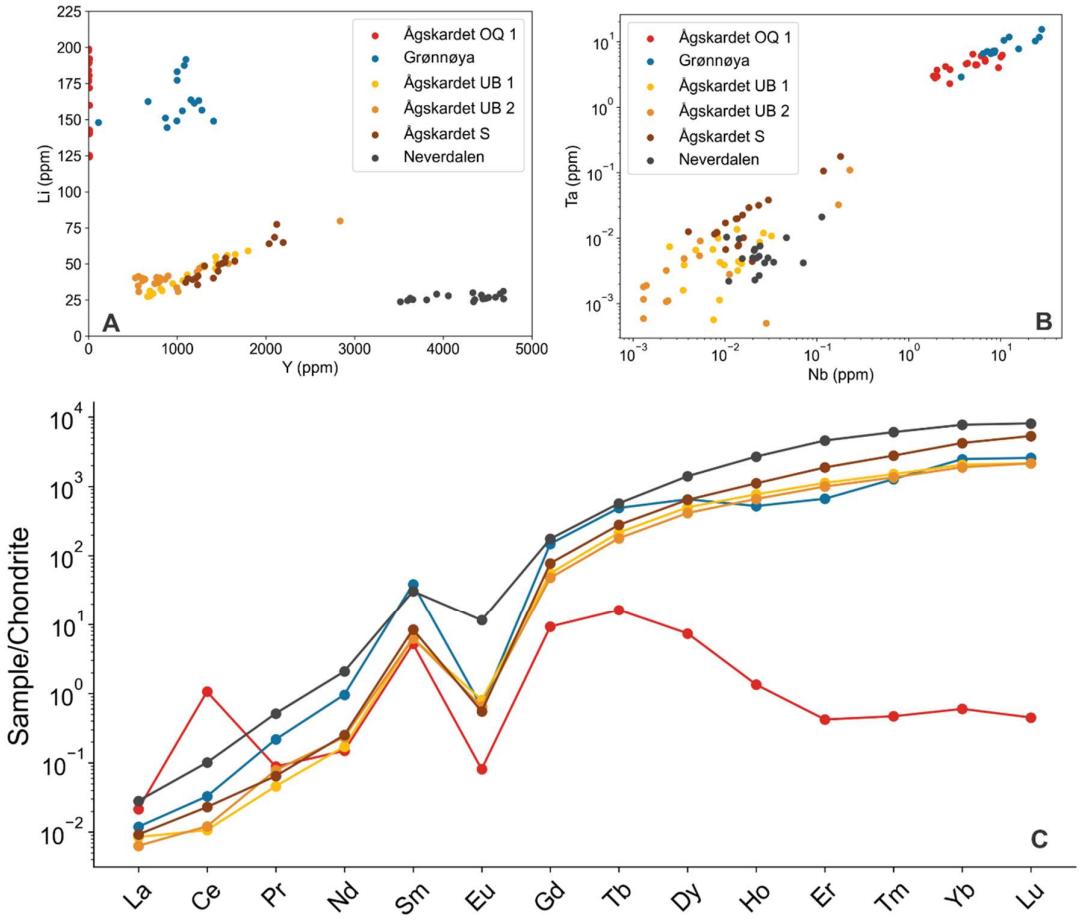

Figure 14. *Garnet trace element composition. A) Li vs. Y (ppm) diagram. The garnet from Neverdalen displays enrichment in Y. B) Ta vs. Nb (ppm) diagram. C) Mean chondrite-normalized REE-patterns. Normalized to chondrite data published by Palme and Jones (2003).*

Neverdalen garnet contains the highest amount of all the rare-earth elements, except for Sm, which is highest in Grønnøya garnet (Figs. 14 and 15). Garnets from Ågskardet OQ1 show depletion in HREE, which is distinct from all other localities. They also show a relative enrichment of Ce. Grønnøya shows a slight depletion in HREE. There is a negative Eu anomaly for all samples, which is strongest for Grønnøya and Ågskardet OQ1 garnets, and very subtle for Neverdalen garnet.

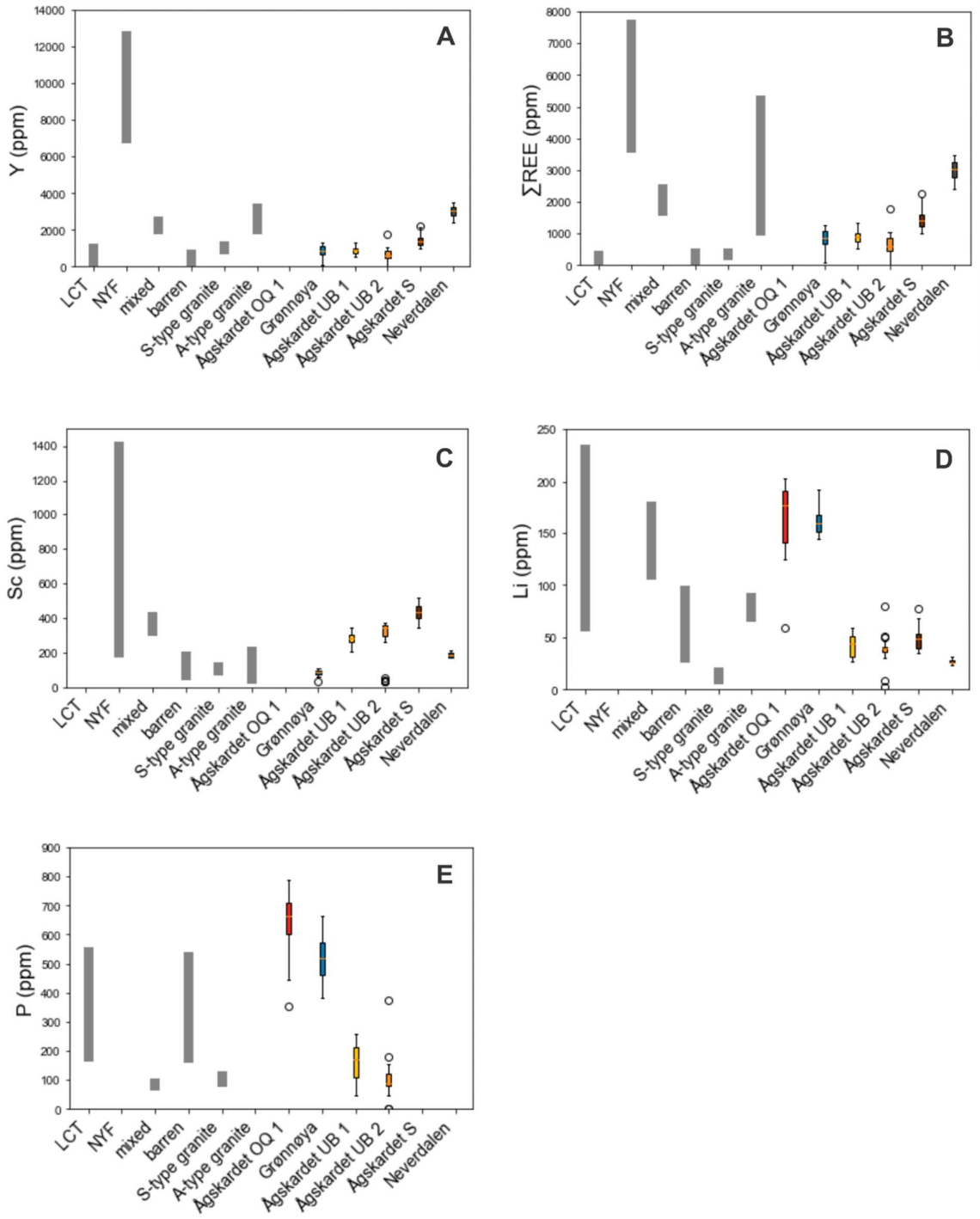

Figure 15. *Box-whisker plots of garnet trace element compositions compared to literature data of various types of pegmatites and granites. The boxes represent the [1]st to [3]rd quartile of data; whiskers represent the maximum and minimum values, and the median values are the bars inside the boxes. Open circles are outliers. The literature boxplots are limited to the interquartile range for better visibility. Literature data from Feng et al. (2023). A) Y (ppm), B) ∑REE (ppm), C) Sc (ppm), D) Li (ppm), E) P (ppm).*

6.4. Mica major and trace element compositions

The simplified chemical formula of minerals of the mica group is: $I_2M_{4-6}\square T_8O_{20}A_4$ (Rieder et al., 1998), in which I is K, Na, Cs, NH_4, Rb, Ba, Ca; M is Li, Fe^{2+}, Fe^{3+}, Mg, Ti, Mn^{2+}, Mn^{3+}, Zn, Al, Cr, V; □ is vacancy; T is Al, Be, B, Fe^{3+}, Si; A is Cl, F, OH, O, S. Other substitutions are possible (Rieder et al., 1998). The number of formula units can vary depending on structure (Rieder et al., 1998). The analyzed mica crystals are inclusions in a large tourmaline crystal (Ågskardet OQ5), or fragments enclosed by a large tourmaline (Ågskardet OQ6). Complete mica major element compositions are listed in Appendix C. The trace element data set is provided in Appendix B. A total of 30 analyses were carried out by EPMA for major element compositions and 18 analyses by LA-ICP-MS for trace element compositions. Micas from Ågskardet OQ6 are dioctahedral and show a narrow compositional range. They classify as muscovite in the diagram by Tischendorf et al. (1997, 2001), which is based on the Mg, Li, Fe and ^{VI}Al contents (Fig. 16). Micas from Ågskardet OQ5 range in composition from muscovite to Li-muscovite, and structurally from dioctahedral to trioctahedral. Inclusion 3 has Li contents between 860 and 2222 ppm. The mica inclusions closer to the core show higher Li contents (19240 to 21425 ppm or 4.1 to 4.6 wt% for Inclusion 2; Fig. 17). The mica fragments within the tourmaline crystal of Ågskardet OQ6 show a Li range between 600 and 1498 ppm.

All mica analyses, except for two, show a correlation between Cs and Rb from 1204 to 2341 ppm Cs and 2655 to 3241 ppm Rb, as well as 600 to 2222 ppm Li (Fig. 17). Values for Ågskardet OQ5 are slightly higher than for OQ6. The two anomalous analyses, which belong to mica Inclusion 2 in the tourmaline crystal of Ågskardet OQ5, show highly elevated values of Rb (4226 and 4380 ppm) and Li (see above). The Cs contents are relatively low (995 and 1211 ppm. Elevated contents of these trace elements are indicative of advanced pegmatite magma evolution (e.g., Černý & Burt, 1984; Kile & Foord, 1998; Černý et al., 2003). The B contents of micas range from 305 to 578 ppm (Ågskardet OQ5) and from 275 to 696 ppm (Ågskardet OQ6).

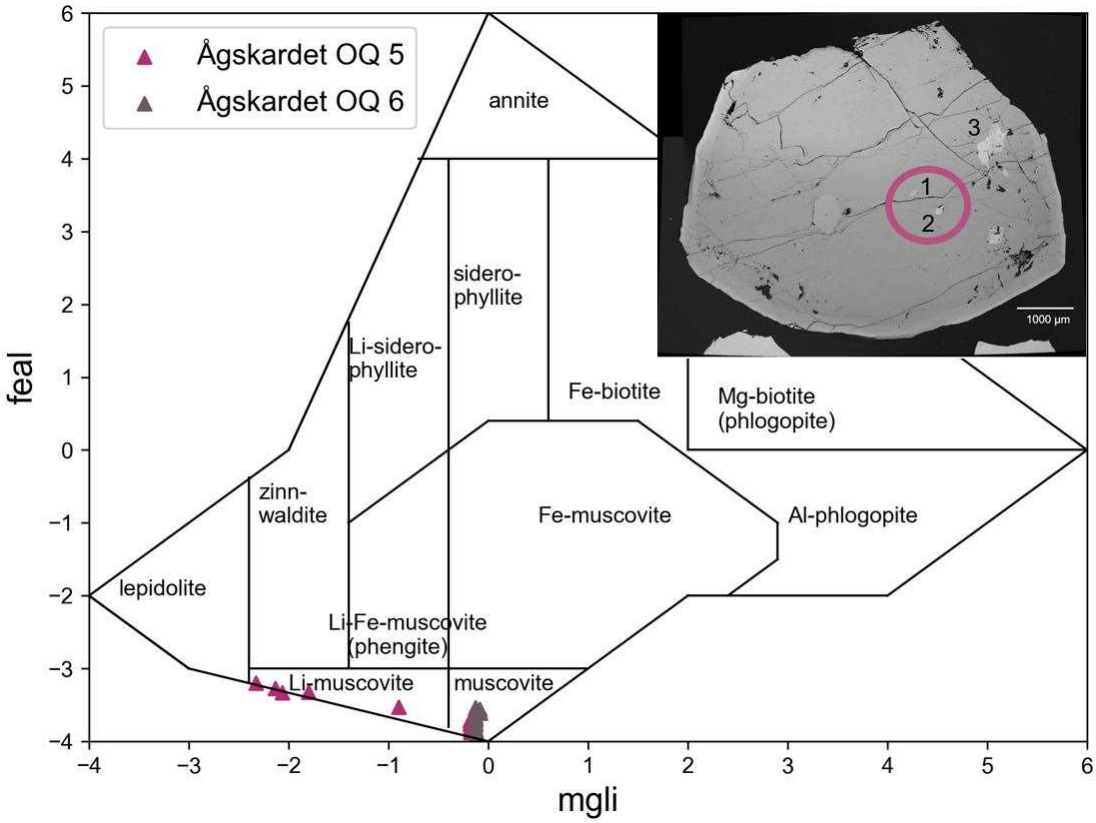

Figure 16. *Mica classification diagram after Tischendorf et al. (1997), in which* feal *is the* Fe_{tot} *+ Mn + Ti -* $Al^{(VI)}$ *(in apfu) and* mgli *is Mg - Li (in apfu). Micas from Ågskardet OQ6 plot as muscovite and micas from Ågskardet OQ5 plot as muscovite and Li-muscovite. The inclusions closer to the core (indicated by a circle) contain higher amounts of Li.*

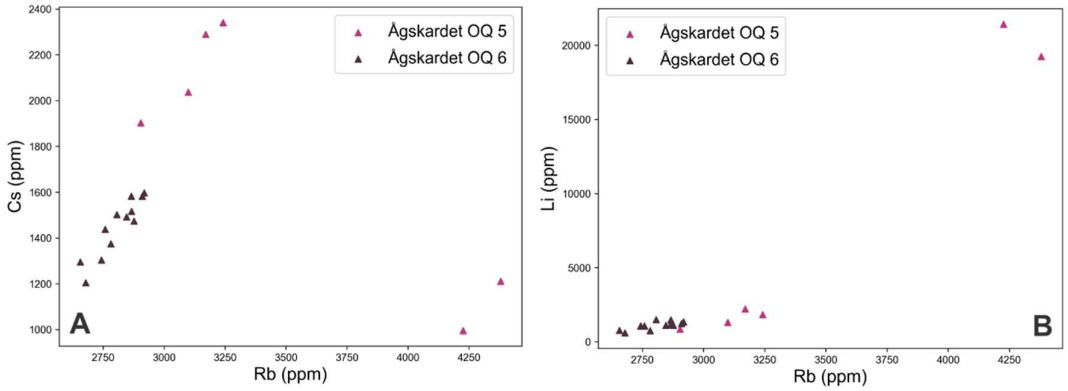

Figure 17. *Trace element composition of mica. A) Cs vs. Rb (ppm) diagram. B) Li vs Rb (ppm) diagram. Two analyses of the same crystal of Ågskardet OQ5 show significantly higher Rb and Li concentrations than the remaining analyses.*

6.5. Boron isotopic compositions

Boron isotopic compositions range from -15.5 to -1.9‰ $\delta^{11}B$ for the sample suite studied (n=213 spot analyses, Fig. 18). The complete dataset is provided in Appendix C. The tourmaline crystal from Ågskardet OQ5 yielded the lowest $\delta^{11}B$ values, from -15.5 in the core to -9.3‰ in the rim. The $\delta^{11}B$ values for the tourmaline crystal from Ågskardet OQ6 range from -14.4 in the core to -9.7‰ in the crack-filling third-generation tourmaline. The $\delta^{11}B$ values for tourmalines from Ågskardet OQ1, OQ2, OQ3, OQ4 and UB2 lie between -11.4 and -8.1‰, and they overlap slightly with the range of values obtained for Ågskardet UB1 at -8.2 to -6.8‰ $\delta^{11}B$. Values for tourmalines from Grønnøya include one outlier at -2.6‰ $\delta^{11}B$, while the rest of the values ranges between -6.4 and -5.0‰ $\delta^{11}B$. Tourmalines from Ørnes 1 and 2 show the highest $\delta^{11}B$ values, ranging from -4.4 to -1.9‰. Tourmalines from Ågskardet OQ2, OQ3, OQ4 and Ørnes 1 show a wide range in $\delta^{11}B$ (up to 1.9‰ for Ågskardet OQ3), which cannot be identified as a core-rim relationship.

The chemical and B-isotopic compositions of the tourmalines show some correlation. The Li-rich tourmalines from Ågskardet OQ5 and OQ6 yield lower mean $\delta^{11}B$ values than the fluor-schorls, schorls and dravites from the other samples, although ranges overlap. Both elemental and B-isotopic compositions of tourmalines from Ågskardet OQ5 and OQ6 change from core to rim (Fig. 19). The dravitic tourmalines from Ågskardet UB1 and UB2 lie within the $\delta^{11}B$ range of the schorlitic tourmalines. The median $\delta^{11}B$ values of the two dravitic tourmaline samples differ by 2.9‰. Schorlitic compositions are found in tourmalines from Ågskardet OQ5, which yield the lowest $\delta^{11}B$ values, and in tourmalines from Ørnes 2, which yield the highest $\delta^{11}B$ values.

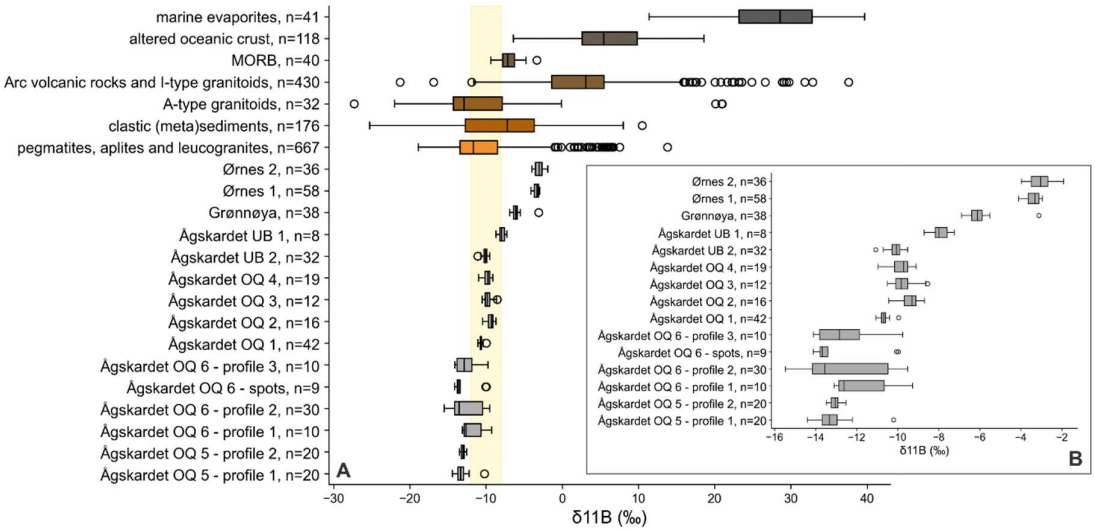

Figure 18. *Box-whisker plots of boron isotopic compositions of the tourmalines studied. The boxes represent the [1]st to [3]rd quartile of data; whiskers represent the maximum and minimum values, and the median values are the bars inside the boxes. Open circles are outliers. A) Data in comparison to literature data. The yellow band is the commonly cited range for boron isotopic compositions of the continental crust (Marschall and Jiang, 2011). Data for pegmatites, aplites and leucogranites from: Chaussidon and Albarède (1992), Trumbull et al. (2008), Yang et al. (2015), Siegel et al. (2016), Gou et al. (2017), Maner and London (2017), Hu et al. (2018), Zhou et al. (2019), Dai et al. (2019), Han et al. (2020), Cheng et al. (2021), Krmícek et al. (2021), Hu et al. (2022), Liu et al. (2022). All other data from references listed in Trumbull et al. (2020). B) Enlarged display of the tourmaline B-isotopic data obtained during this study.*

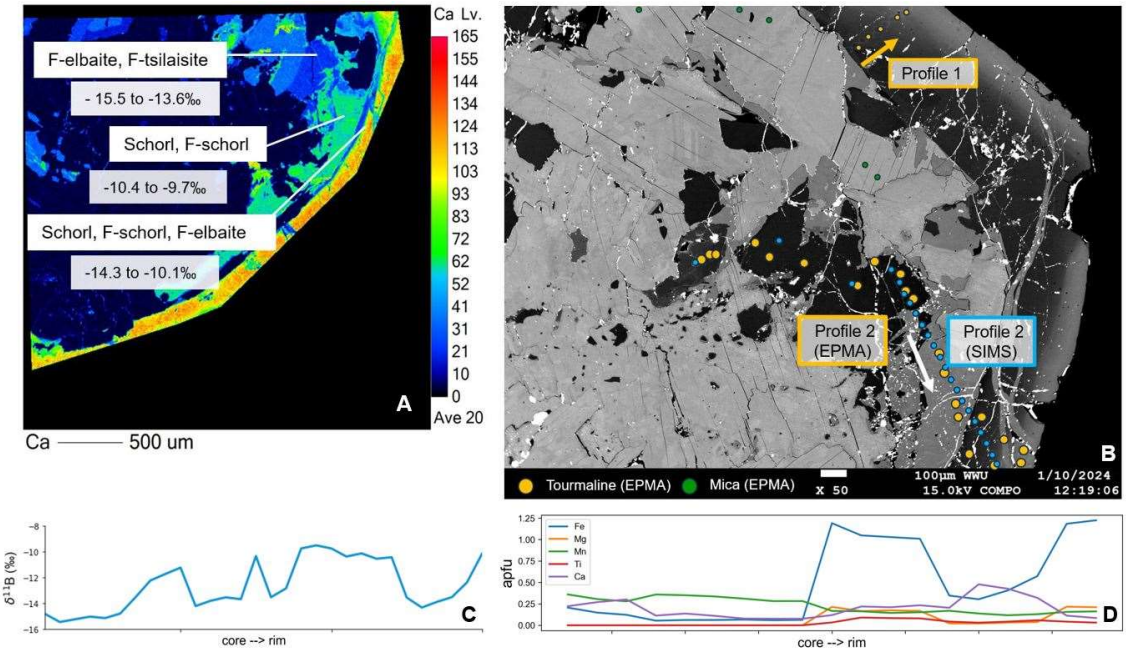

Figure 19. *Comparison of major element and B-isotope core-rim relationship in profile 2 from Ågskardet OQ 6. A) Element map showing 3 generations of tourmaline that differ in Ca content. Their names according to Henry et al. (2011) classification and the range of δ11B values (1σ/mean = 0.91‰) per generation is given. B) BSE image of the tourmaline crystal from Ågskardet OQ6 with indicated EPMA (yellow, green) and SIMS (blue) analysis spots. C) B-isotopic core-rim profile 2 from Ågskardet OQ6. The jumps in composition likely indicate the different generations. D) Major element profile 2 from Ågskardet OQ6. The Fe content varies with tourmaline generation. Ca content increases in the rim but decreases again toward the outermost rim.*

6.6. Oxygen isotopic compositions

The $\delta^{18}O$ values of the bulk rock basement samples range from 6.50‰ for the mafic gneiss from Neverdalen to 10.86‰ for the paragneiss from Ågskardet UB. The $\delta^{18}O$ values for the pegmatite-derived garnet samples range from 5.03 (Neverdalen) to 11.15‰ (Ågskardet UB1; Fig. 20, Table 7). Grønnøya shows the second lowest value after Neverdalen with 7.92‰ $\delta^{18}O$. Pegmatite-derived quartz ranges from 7.28 (Neverdalen) to 15.32‰ $\delta^{18}O$ (Ågskardet UB1). The 1-sigma standard deviation is 0.1‰ for $\delta^{18}O$ measurements of garnet and quartz, and 0.4‰ for $\delta^{18}O$ measurements of the bulk rock basement samples.

Regarding the results from the triple oxygen isotope measurements, the corresponding $\Delta'^{17}O_{0.528}$ values for garnet vary between -76 ppm (Ågskardet UB1) and -56 ppm (Grønnøya). For quartz, $\Delta'^{17}O_{0.528}$ ranges from -75 ppm (Ågskardet UB2) to -55 ppm (Grønnøya). The bulk rock basement samples range from -67 ppm (Neverdalen) to -49 ppm (Ågskardet UB). The 1-sigma standard deviation falls between 4 and 7 ppm for $\Delta'^{17}O$ measurements of garnet and quartz, and between 7 and 10 ppm for $\Delta'^{17}O$ measurements of the basement samples. If the somewhat anomalous Neverdalen pegmatite sample is excluded, then garnet fractions from the other pegmatite samples define a trend with a slope of 0.527 in linearized triple oxygen isotope space (Fig. 20B). This observation suggests low-temperature oxygen isotope fractionation, as will be discussed in Chapter 7.1.3.

6.7. Oxygen isotope thermometry

The $\Delta^{18}O_{(Qz-Grt)}$ is highest for Ågskardet UB1 (4.17‰) and lowest for Ågskardet UB2 (1.36‰), followed by Neverdalen (2.25‰). Lower quartz–garnet fractionation suggests higher equilibrium temperatures in the magmatic system. The calculated apparent equilibrium temperatures range from 532 ± 20 °C (Ågskardet UB1) to 1139 ± 115 °C (Ågskardet UB2). The result for Ågskardet OQ1 is 585 ± 25 °C, for Gønnøya 588 ± 25 °C and for Neverdalen 823 ± 53 °C (Table 7).

The difference in thermometry results from applying either A= 2.71‰ K^2 or the interpolation mentioned in Chapter 5.6. is strongest for Neverdalen, where the applied A-coefficient of 2.96‰ K^2 yields +63°C. A second set of temperature calculations was performed based on the modified increment method after Zheng (1993), which is a theoretical method considering chemical composition and crystal structure. This thermometer has an applicable temperature range of 0 - 1200°C, but it has been shown to not be as precise and accurate as empirical calibrations (e.g., Chacko et al., 2001). The results from this method yield temperatures that are 50 to 105 °C higher than results using the empirical method after Valley et al. (2003). Quartz-garnet oxygen isotope thermometry is expected to yield minimum equilibrium temperatures, because of isotopic exchange between quartz and minerals with a lower closure

temperature (e.g., muscovite, plagioclase, K-feldspar), which further enriches ^{18}O in quartz (Moecher & Sharp, 1999).

Table 7. *Results of triple oxygen isotope analysis for garnet, quartz and basement samples, normalized to San Carlos olivine with $\delta^{18}O$ = 5.23‰ and $\Delta'^{17}O$ = -52 ppm, and calculated apparent temperatures for quartz-garnet pairs from the pegmatites. Temperatures calculated using the equation $\Delta^{18}O_{(Qz-Grt)} \approx 10^3 ln[\alpha_{(Qz-Grt)}] = [A_{(Qz-Grt)}10^6]/T^2$; where $A_{(Qz-Grt)}$ = 2.71 (Valley et al., 2003). The given temperature range per sample represents analytical error, not uncertainties connected to coefficient A.*

	Garnet				Quartz					
	$\delta^{18}O_{VSMOW}$ (‰)	± 1 s.d.	$\Delta'^{17}O_{0.528}$ (ppm)	± 1 s.d.	$\delta^{18}O_{VSMOW}$ (‰)	± 1 s.d.	$\Delta'^{17}O_{0.528}$ (ppm)	± 1 s.d.	T calculated (°C, ±2 s.d.)	Ref. used for calculation
Grønnøya	7.92	0.1	-56	4	11.57	0.1	-55	4	588 ± 25 °C	Valley et al., 2003
Ågskardet OQ 1	8.72	0.1	-62	4	12.39	0.1	-72	4	585 ± 25 °C	Valley et al., 2003
Ågskardet S	8.60	0.1	-64	4	-				-	
Ågskardet UB 1	11.15	0.1	-76	4	15.32	0.1	-56	4	532 ± 20 °C	Valley et al., 2003
Ågskardet UB 2	10.03	0.1	-64	4	11.39	0.0	-75	0	1139 ± 115 °C	Valley et al., 2003
Neverdalen	5.03	0.1	-69	4	7.28	0.0	-59	0	823 ± 53 °C	Valley et al., 2003

	Basement			
	$\delta^{18}O_{VSMOW}$ (‰)	± 1 s.d.	$\Delta'^{17}O_{0.528}$ (ppm)	± 1 s.d.
Neverdalen	6.5	0.4	-66,8	10.2
Ytre Holten	7.3	0.4	-49,7	10.2
Åsjord	9.0	0.4	-50,8	10.2
R. Kleiva Q	8.4	0.4	-56,8	10.2
Ågskardet UB	10.9	0.0	-48,7	7.0

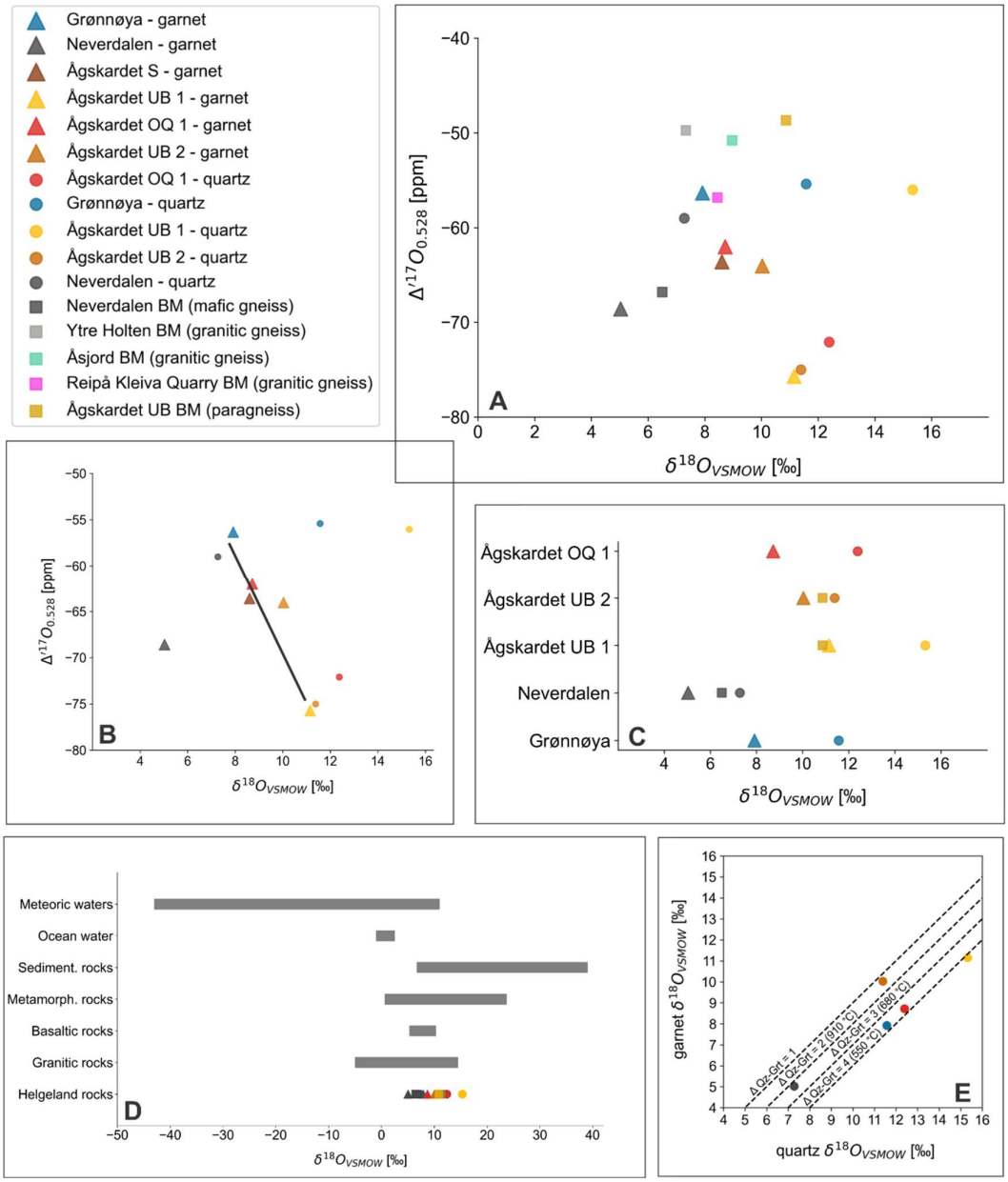

Figure 20. *Oxygen isotopic composition of garnet, quartz, and basement samples. A) $\Delta'^{17}O_{0.528}$ (ppm) vs. $\delta^{18}O_{VSMOW}$ [‰] diagram of all measured samples. BM = Basement. Neverdalen basement consists of mafic TIB gneiss, and Ytre Holten, Meløy, and Reipå Kleiva Quarry are granitic TIB gneisses. The basement of Ågskardet UB consists of Paleoproterozoic paragneiss. Except for Neverdalen, the basement samples show a similar range as garnet. The mafic gneiss of Neverdalen shows a slightly lower $\delta^{18}O$ value than the granitic gneisses and the paragneiss shows a slightly higher value. B) $\Delta'^{17}O_{0.528}$ (ppm) vs. $\delta^{18}O_{VSMOW}$ [‰] diagram of garnet and quartz. The garnet samples show a common trend indicated by a fitted line, which only the Neverdalen sample is not part of. C) $\delta^{18}O_{VSMOW}$ [‰] values per locality. Where the immediate basement was sampled, it is included. Quartz shows systematically higher values than garnet. D) Garnet, quartz, and basement samples compared to typical $\delta^{18}O$ values of important geological reservoirs. Adapted from Hoefs (2018). E) Diagram of $\delta^{18}O$ of garnet vs. $\delta^{18}O$ of quartz from the pegmatite samples. Lines of constant difference (ΔQz-Grt =2, 3 and 4) correspond to temperatures of 910, 680 and 550 °C, respectively. Notice the contrasting results for the samples from Ågskardet UB. Temperatures calculated using the equations of Valley et al. (2003) for quartz-almandine.*

7. Discussion

7.1. Sources of the pegmatite-forming magmas

Classic models of LCT pegmatite formation suggest that they are derived from fertile parental granites by magmatic differentiation. In the larger Glomfjord area, however, no granitoids of the same age as the pegmatites are exposed or known to exist otherwise. It could be suggested that parental granites of Caledonian age exist at depth. Drivenes et al. (2016) inferred an underlying S-type granitic pluton in the larger Glomfjord area to explain the occurrence of high-salinity fluids and corresponding W-mineralization at Bjellåtind, about 10 km northeast of the Ørnes pegmatite. Lomotey (2023) dated the North Helgeland pegmatites to ages between 422 ± 5 and 412 ± 5 Ma for an older generation, and between 403 ± 6 and 387 ± 6 Ma for a younger generation, which might have formed by partial melting of the deeper crust during the collisional stage and by decompression melting of the crust during post-collisional extension of the Caledonian orogen, respectively. Partial melting of heterogeneous crustal basement sources, such as the TIB orthogneisses and Paleoproterozoic metasedimentary rocks was suggested. Lomotey (2023) did not find any geochemical evidence for an underlying pluton in the larger Glomfjord area.

7.1.1. Constraints from major and trace element compositions

Tourmaline compositions in the selected pegmatite bodies vary between dravite at Ågskardet upper body and schorl at Grønnøya, Ørnes, and in the outer zones of the Ågskardet old quarry pegmatites. The inner zone of the Ågskardet old quarry pegmatite contains F-schorl, F-elbaite, elbaite and F-rich tsilaisite, as well as F-liddicoatite (1 spot analysis). The dravitic compositions of the upper pegmatite at Ågskardet may indicate crystallization at higher temperatures (Selway, 1999). Schorlitic compositions are expected in less evolved pegmatites and the outer zones of evolved pegmatites (Selway, 1999; London, 2008). For Grønnøya and Ørnes, pegmatite bodies for which rare-element mineralization has been reported (Ihlen, 2004), these compositions could therefore be indicative of sampling of tourmalines in the outer zones and do not preclude the occurrence of Li-rich tourmaline in other parts of the pegmatite bodies. However, such an occurrence cannot be assumed either.

Caixeta Borges (2023) compared the Li concentration and the REE pattern of the Ågskardet pegmatite to those of the amphibolite and banded gneiss host rocks, and they suggested that several of the observed similarities indicate partial melting of the wall-rocks as a possible source for the pegmatite magma. My study shows that garnet from the other pegmatite bodies in the larger Glomfjord area have notably different REE patterns compared to garnet from the Ågskardet OQ pegmatite, which might indicate different sources or a different degree of

magmatic or magmatic-hydrothermal evolution (Fig. 14). The first option would support the theory of local pools of partial melts and varying degrees of melting. The garnet REE pattern for the Ågskardet OQ pegmatite is similar to the bulk pegmatite REE pattern in Caixeta Borges (2023), which renders fractionation of REE into certain accessory minerals unlikely as the main reason for the rather depleted REE pattern. The depletion could also be caused by a tetrad effect that can occur in highly differentiated granitic rocks and leads to trace element behavior that is similar to that in aqueous systems (Irber, 1999). This effect reflects selective partitioning and chemical complexation of REE by F during fluid exsolution (Irber, 1999).

Garnets from Neverdalen are enriched in Y and ∑REE compared to the other pegmatite localities (Fig. 15). Yttrium and the HREE are compatible in garnet, especially Mn-rich garnet, following the substitution of (Y^{3+}, REE^{3+}) + Al^{3+} for Mn^{2+} + Si^{4+} (Jaffe, 1951; Geller & Miller, 1959). The Neverdalen garnets also have the highest (MnO + CaO) / (FeO + MgO) ratio of all studied garnets (Fig. 13A). According to Baldwin and von Knorring (1983) and Moretz et al. (2013), this major element ratio is an indicator for melt evolution. The Neverdalen dyke is a small narrow body and zonation appears to be absent. The high Mn contents of the garnets are therefore unlikely to represent a high level of fractionation but are rather indicative of a Mn-rich protolith. This interpretation is supported by comparison of the Neverdalen garnets to garnets from the other localities, which define a common trend in the (FeO + MnO) vs. MnO diagram, which Neverdalen is not a part of (Fig. 13B). This ratio is also a sensitive indocator for the degree of fractionation of pegmatite-forming melts (Müller et al., 2012). The elevated Ca content and the smaller Eu anomaly of the Neverdalen garnets support the suggestion of a more primitive parent melt with regard to granitic magma differentiation, which is in agreement with observations by Lomotey (2023) on compositional trends of micas from Neverdalen and the North Helgeland pegmatites. Lomotey (2023) reports plagioclase from the Neverdalen pegmatite dyke to be of oligoclase composition, with a CaO content of 3 to 3.5 wt%. For comparison, plagioclase from the Ågskardet S locality has a CaO content of up to 4% but does not show Ca enrichment in garnet. Therefore, a generally Ca-enriched bulk pegmatite composition is not necessarily the main reason for Ca-rich garnets in Neverdalen.

For the other localities than Neverdalen, the (MnO + CaO) / (FeO + MgO) ratio and (FeO + MnO) vs. MnO ratios seem to represent the state of evolution of the single pegmatite bodies, which is also indicated by tourmaline major element compositions (Fig. 8) and might be listed as follows: Ågskardet OQ > Grønnøya (+ Ørnes) > Ågskardet S > Ågskardet UB. This is supported by the garnet Nb and Ta contents, which correlate for all localities, but are very low for all localities except for Grønnøya and Ågskardet OQ1 (Fig. 14).

The geochemical peculiarities of the Neverdalen dyke could be a result of local biotite-dehydration melting related to crustal thickening during the collisional stage of the Caledonian orogeny, which is in agreement with the age of 413 ± 2 Ma determined by Lomotey (2023). Biotite can be enriched in rare metals, especially after further enrichment through previous muscovite-dehydration melting, and the solubility of accessory enriched phases in the melt is higher due to the higher melting temperatures of restitic biotite-rich components (Wolf et al., 2018; Romer & Pichavant, 2021). This interpretation might be in agreement with the elevated apparent temperature of the Neverdalen pegmatite dyke as inferred from oxygen isotope thermometry (see Chapter 7.1.3.). A higher crystallization temperature accords with less fractionation observed in the pegmatite. However, the high apparent temperature could also reflect disequilibrium between garnet and quartz. In terms of pegmatite families, biotite-dehydration melting might account for NYF or mixed LCT-NYF signatures (Romer & Pichavant, 2021).

The Neverdalen dyke is emplaced in a shear zone between a mafic biotite-rich TIB gneiss and a fertile metasedimentary unit. Partial melting of both units to varying degrees at high temperatures could be in agreement with high Mn and Ca contents, REE enrichments, low levels of Li and absence of P in the garnets, as well as the abundance of biotite and the occurrence of Fe-oxides and allanite in the pegmatite dyke. A more likely explanation with respect to biotite-dehydration melting is a peritectic origin of the garnet that can scavenge Mn (Clemens & Stevens, 2012; Dorais & Tubrett, 2012). Fe-Ti oxides and relatively calcic plagioclase are also common peritectic phases (Clemens & Stevens, 2012). Referring to the new pegmatite classification system by Wise et al. (2022), this pegmatite body shows a higher affinity to Group 2 pegmatites. Interpretations of Hf isotopic compositions by Lomotey (2023) are in agreement with the partial melting of the metasedimentary unit as source to the Neverdalen dyke.

Circling back to REE characteristics of garnets from the selected pegmatite bodies, when comparing the chondrite-normalized patterns for all localities, similarities between Neverdalen, Ågskardet UB1-2, Ågskardet S and to a large extent also Grønnøya are obvious (Fig. 14). Due to the affinity of garnet to HREE, left-inclined chondrite-normalized REE patterns might be expected. However, for LCT pegmatites, a depletion in HREE to some extent would be presumed, as observed in the Ågskardet OQ pegmatite (Mitchell, 2017; Feng et al., 2023). In many analyses, the chondrite-normalized REE contents exceed the value of 10^3 x chondrite, which has been named as a threshold to distinguish between LCT pegmatites that have lower values and NYF pegmatites that exceed the threshold (Mitchell, 2017). It might therefore be suggested that the North Helgeland pegmatite field does not show pure LCT affinity, but a

mixed LCT-NYF affinity (see Fig. 15). A mixed affinity would be reasonable if the I-type TIB gneisses were involved in the partial melting (Černý & Ercit, 2005).

7.1.2. Possible sources of boron in the pegmatite-forming magmas

S-type granitic melts and their associated pegmatites form from melting of mica-rich metasedimentary rocks (Martin & De Vito, 2005; Acosta-Vigil et al., 2010; Černý et al., 2012; London & Morgan, 2012). Boron and Li, as well as Rb and Cs, are considered to be sourced from micas, although some studies also mention a role for evaporites in the metasedimentary rock sequences as sources for B and Li (Jiang & Palmer, 1998; Simmons & Webber, 2008; Bradley, 2019). Boron-isotopic compositions can record the source of B in magmas (Fig. 18). Generally, the B-isotopic compositions of the North Helgeland pegmatites lie within the expected range for partial melts from the deeper heterogeneous continental crust. The old quarry and upper body pegmatites at Ågskardet are in good agreement with the commonly cited range of $\delta^{11}B$ (-8 to -12‰) from the continental crust (Marschall & Jiang, 2011), which would be expected for siliciclastic sediments and S-type granites. The Grønnøya (-5.6 ± 0.6‰ $\delta^{11}B$) and Ørnes (-3.6 ± 0.5‰ $\delta^{11}B$) pegmatites have a somewhat heavier tourmaline B-isotopic composition. This could indicate a metasedimentary rock sequence of marine affinity, such as evaporites or carbonates, within the magma source. Alternatively, given that I-type granitoids commonly have a heavier B-isotopic signature than S-type granitoids, a larger proportion of TIB gneisses could have been involved during crustal melting. Distinguishing between different source lithologies involved requires mass-balance constraints and can therefore be difficult and highly model-dependent (Trumbull et al., 2020). A third option to explain the heavier B-isotopic signature is interaction between pegmatite-forming magma and the host country rocks. The Grønnøya and Ørnes pegmatites are both hosted by amphibolite, a rock type that contains an average of 9 µg/g boron (n=189; Trumbull & Slack, 2018). The B-isotopic composition of amphibolites may vary depending on the protolith. However, no extensive alteration of the wall-rocks to these pegmatites is reported, which makes it difficult to sustain this idea in the absence of additional analyses of these country rocks.

7.1.3. Insights from oxygen isotopes

The analysis of oxygen isotopic compositions may also offer insights into possible magma sources. Garnet has a high closure temperature for oxygen diffusion and the isotopic composition of magmatic garnet is therefore expected to be close to that of the magma and, thus, the source (Coghlan, 1990; Farquar et al., 1996; Harris and Vogeli, 2010). The use of garnet mineral separates rather than whole-rock powders additionally allows to circumvent problems associated to post-magmatic alteration and surface weathering.

The mafic TIB gneiss from Neverdalen has a slightly lower $\delta^{18}O$ value than the granitic TIB gneisses, whereas the paragneiss from Ågskardet UB has a higher $\delta^{18}O$ value than the granitic TIB gneisses (Fig. 20A, C). The basement gneisses from the Glomfjord area and the pegmatitic garnets have similar $\delta^{18}O$ compositions. The basement gneisses can therefore be considered a potential source to the pegmatite melts. An exception to this is the Neverdalen occurrence. The pegmatitic garnet from the Neverdalen dyke has a rather low $\delta^{18}O$ value (5.0 ± 0.1‰), which is difficult to explain by melting of the mafic TIB gneiss (6.5 ± 0.4‰ $\delta^{18}O$), as it is below the mantle value. According to Bindeman (2008), magmatic rocks with $\delta^{18}O$ values below the mantle value of 5.7‰ are likely derived from rocks altered hydrothermally at high temperatures involving small isotope fractionations, which means that a significant portion of their oxygen has a surface origin. Based on the indications from Hf-isotopic compositions, the next logical step would have been oxygen isotope analysis of the adjacent metasedimentary rocks, a task that remains to be done in the near future. In general, the garnet $\delta^{18}O$ values are quite variable, which may reflect pegmatite magma formation by melting of an isotopically heterogeneous source. This source likely involved several different crustal lithologies.

Results from triple oxygen isotope analysis support partial melting of metasedimentary rocks and TIB orthogneisses as a possible source of the granitic pegmatite magmas. The triple oxygen isotopic signature reflects exchange reactions with the hydrosphere, indicating recycling of continental crust (Bindeman, 2021), best achieved by the transfer of water-lain sediments to great crustal depths during orogenesis. In linearized triple oxygen isotope space, the pegmatite-derived garnet samples define a trend with a slope of 0.527, typical for low-temperature oxygen isotope fractionation, as it occurs in sediments (Fig. 20B). These data are a powerful indicator for the involvement of metasedimentary rocks in the source to the pegmatite magmas in northern Helgeland. By contrast, mantle-derived rocks and their differentiates, such as I-type granites, define a trend with a slope of 0.523 in linearized triple oxygen isotope space (Bindeman, 2021).

Another application of oxygen isotope analysis is geothermometry. By analyzing mineral pairs from a magmatic rock paragenesis, an empirically or theoretically determined fractionation factor can be employed to calculate a crystallization temperature, assuming equilibrium. The interpretation of thermometry results needs consideration of various factors. Most importantly, oxygen diffusion closure temperatures and magmatic crystallization temperatures are not identical. The apparent temperatures yielded by the $\Delta^{18}O$ of mineral pairs can record post-crystallization exchange with deuteric fluids or even alteration, if the closure temperatures of the studied minerals are comparatively low. There are various estimates for the closure temperature of garnet, ranging from 812 to 1198°C (Hoffbauer et al., 1994; Farquhar et al., 1996; Kohn & Valley, 1998). Assuming the garnet closure temperature is higher than that of

crustal anatexis, the garnet $\delta^{18}O$ composition would not be altered by diffusion after crystallization from an anatectic melt. In contrast, quartz has a closure temperature of <550°C, which means that oxygen diffusion continues after magmatic crystallization at higher temperatures. Slow closed-system cooling, as typical for intrusive granitic rocks, will therefore further fractionate ^{18}O in quartz. If the temperature of anatexis and the $\Delta^{18}O$ of the main rock-forming minerals are known, equilibrium fractionation factors can be inferred.

For the pegmatites studied, the correlations between garnet and quartz $\delta^{18}O$ values for each pegmatite occurrence imply little or no influence by external fluids or a change in melt source (Fig. 20C). The crystallization temperature of pegmatite-forming magmas is 700 to 400°C, and for rare-element pegmatites a narrow range between 560 and 500°C has been determined (McCaffrey & Jowitt, 2023). The temperatures obtained for the Ågskardet OQ1 (585 ± 25°C) and Grønnøya (588 ± 25 °C) pegmatites therefore seem reasonable. The temperature determined for the Neverdalen pegmatite dyke is significantly higher (823 ± 53 °C), and the different nature of this granitic magma is also indicated by the distinctly different garnet major and trace element compositions (Figs. 13, 15 and 20E).

The apparent temperatures obtained for the two pegmatite samples from the upper body at Ågskardet are more difficult to explain, because they are significantly different from each other. The quartz-garnet mineral pair from UB1 yielded a temperature of 532 ± 20°C and the pair from UB2 yielded 1139 ± 115°C (Fig. 20E). This discrepancy is mainly caused by the strongly deviating quartz $\delta^{18}O$ values for these two samples from the same pegmatite body. The difference in garnet $\delta^{18}O$ values between the two samples can be explained by a heterogeneous magma source, or by contamination of the melt with wall-rock materials resulting in a garnet $\delta^{18}O$ composition that was not fully homogenized due to the high closure temperature of garnet. These processes have been suggested as the main reasons for a wider than expected $\delta^{18}O$ range observed in magmatic garnet suites from other localities worldwide (King & Valley, 2001; Lackey et al., 2006; Harris & Vogeli, 2010). The sample RL2206A from Ågskardet UB1 was taken from the outer deformed margin of the pegmatite body. Therefore, it is possible that late-stage contamination of the magma led to an increase in $\delta^{18}O$, as is recorded by the quartz. The occurrence of sillimanite in Ågskardet UB1 supports this proposal. Crystallization of sillimanite in contaminated granites has been reported from other localities (Lackey et al., 2006). In these cases, sillimanite is often localized near metasedimentary wall-rocks at pluton margins. For Ågskardet UB1, the paragneiss host rock could potentially be a source of the excess Al. Sillimanite is a late phase in this sample and typically associated with K-feldspar. It may have resulted from the breakdown of magmatic muscovite, possibly facilitated by decompression, or change in melt/fluid behavior, or temperature increase: muscovite + quartz = sillimanite + K-feldspar + H_2O ± melt (Lackey et al., 2006). Temperature

increase related to the observed ductile deformation, potentially combined with fluid infiltration, could be a likely explanation for the crystallization of sillimanite and disequilibrium $\Delta^{18}O$ for quartz-garnet pairs.

The dravitic composition of tourmalines and the larger pyrope component in garnets for the upper pegmatite body at Ågskardet may indicate a higher crystallization temperature. However, the temperature obtained for Ågskardet UB2 appears to be unreasonably high, especially when considering the high water contents expected for pegmatitic magmas. The presence of graphic texture in the pegmatite body emphasizes its low-temperature nature near the eutectic point, as opposed to coarse-grained granites crystallized at much higher temperatures. This strongly suggests that the quartz-garnet pair does not record oxygen isotope equilibrium conditions for Ågskardet UB2.

7.2. Magmatic-hydrothermal evolution

7.2.1. Major element fractionation trends

For the old quarry pegmatite at Ågskardet, the major and trace element trends defined by tourmaline suggest crystallization from a progressively more evolved granitic magma, as previously shown by others for zoned pegmatites (e.g., Jolliff et al., 1986; Soares et al., 2008). The innermost zone of the Ågskardet pegmatite, mapped as albite replacement zone by Ihlen (2004) and Caixeta Borges (2023), might record the influence of a late aqueous fluid on the mineral assemblage, including tourmaline addition. The Fe contents of tourmaline decrease from the outer zones of the Ågskardet pegmatite towards the inner zones, and Li and Mn contents increase in the same direction. This trend is expected from igneous fractionation of an inward crystallizing magmatic body (Selway, 1999). The stability of different tourmaline compositions with progressive crystallization is also related to the temperature-pressure conditions. For example, Mg is preferred in the Y-site at higher temperatures, Fe at intermediate temperatures, and Li at lower temperatures (Selway, 1999). The observed trend in X-site variation in tourmaline from the old quarry is consistent with the description of X-site variations in the lepidolite sub-type of Li-rich pegmatites (Selway et al., 1999). With ongoing evolution, they describe early vacancy-rich foitite, intermediate Na-rich schorl and elbaite, and late tourmaline (rossmanite) with lower Na content and more vacancies. Tourmaline of the old quarry follows this trend, except for a change in composition at late stage. Tourmalines from Ågskardet OQ1, a layered segment of the outer zone of the pegmatite body, are vacancy-rich on the X-site. Tourmalines from Ågskardet OQ2, OQ3 and OQ4 have schorl and Na-rich F-schorl compositions. There is a positive correlation between Na and F in tourmaline controlled by crystal chemistry (Selway et al., 1999). The large crystals of OQ5 and OQ6, however,

increase in Ca toward the rims. The increase in Ca is accompanied by an increase in Fe, Mg, Ti and REE, and a decrease in Mn. The correlation between Ca and REE is also explained by crystal chemistry. Tourmaline zoning is usually ascribed to an influx of components either from elsewhere in the pegmatite or from the host rock (London, 2016).

The first explanation refers to the availability of these elements from interaction of an aqueous fluid with the host rocks, in this case banded gneisses, leading to dissolution of those elements and contamination of the fluid. Foord et al. (1986) argued for hydrothermal alteration of intermediate to mafic host rocks to explain the crystallization of Ca- and Mg-rich minerals in pegmatite pockets at a relatively late stage to the main pegmatite assemblage. According to London (2016), the fluor-liddicoatite-bearing pegmatites of Madagascar were contaminated with Ca by their marble host rocks. Caixeta Borges (2023) offered a similar explanation for the evolved Ca-rich tourmaline compositions observed in the Ågskardet old quarry pegmatite, but also mentioned the possibility of Ca enrichment in the residual melt or fluid. Calcium^{2+} partitions strongly into hydrosaline or borosilicate melts over granitic silicic melts (Veksler et al., 2002; Veksler, 2004; Veksler et al., 2012). Melt immiscibility and preferential partitioning of Ca into the hydrosaline melt or fluid might be a source to late Ca enrichment from within the pegmatite, as explained below.

Albite replacement zones in pegmatites, as mapped by Ihlen (2004) and Caixeta Borges (2023) in the Ågskardet old quarry, may be formed by metasomatism through a Na-rich aqueous fluid or hydrosaline melt, which can develop during melt-melt or melt-fluid immiscibility (Thomas et al., 2012; Müller et al., 2018; Ballouard et al., 2020a). Melt and fluid inclusion studies on pegmatite minerals show that below ~720°C the coexistence of at least three liquid or liquid and vapor phases with contrasting physical and chemical characteristics is possible: (i) a peraluminous silicate-rich, water-poor melt; (ii) a silicate-poor hydrosaline melt; (iii) a lower salinity aqueous fluid (Thomas et al., 2000; Thomas et al., 2006; Thomas et al., 2012). The viscosities of such hydrosaline melts might be low enough to move as supercritical or trans-magmatic fluids (Thomas & Davidson, 2012), and they can dissolve high concentrations of rare elements (Thomas & Davidson, 2016). Element partitioning between silicate and saline melts is dependent on the ionic charge and the atomic radius of the cation (Veksler, 2004). Thomas and Davidson (2012) describe the following path of pegmatite melt and fluid evolution: melt → magmatic fluid → fluid → fluid-gas → fluid hydrothermal → hydrothermal. Later involvement of external fluids and possibly meteoric water are also plausible, depending on tectonic setting and emplacement depth (Bakker & Elburg, 2006; Piilonen et al., 2012; Audétat & Edmonds, 2020).

For elbaite-subtype pegmatites, Selway (1999) describes tourmaline compositions as commonly Na-rich schorl in massive pegmatites, Mn-rich elbaite in pockets and late-stage enrichment of Ca and F in elbaite and fluor-liddicoatite. The subtype classification is dependent on the predominant Li-mineral and correspondent pressure, temperature and geochemical compositions (Novák & Povondra, 1995). No subtype has been determined for the Ågskardet OQ pegmatite, which contains both lepidolite and elbaite, as well as spodumene (Ihlen, 2004; Caixeta Borges, 2023). Ca-rich rims on late-stage elbaite are, however, within the expected compositional range of evolving pegmatite magmas so that external fluids may not be required to explain this trend. It must be noted, however, that along the wall zones of pegmatites and wherever the reactive melts or fluids are in contact with the host rocks, chemical exchange typically occurs (London, 2008; Thomas & Davidson, 2012).

7.2.2. Textures of tourmaline and accompanying minerals

The intergrowth between quartz and tourmaline in Ågskardet OQ2-4 suggests that they crystallized at the same time (Figs. 5 and 29). Skeletal tourmaline with quartz cores or graphic intergrowths of tourmaline and quartz in the outer zones of pegmatites are commonly observed (Jolliff et al., 1986; London, 1996; Hulsbosch et al., 2019; van der Does et al., 2024). Graphic intergrowth can be attributed to highly supersaturated, undercooled viscous silicate melts, high crystal growth rate, heterogeneous nucleation of crystals from the pegmatite fluid, or liquid immiscibility in low viscous silicate melts (Manning, 1982; Fenn, 1986; Thomas & Veksler, 2002; London, 2009; Thomas & Davidson, 2012; Sirbescu et al., 2017). Tourmalines with quartz cores in Ågskardet OQ2 and 4 could have formed by heterogeneous nucleation and rapid crystal growth, followed by crystallization of quartz. The quartz filled the open end of the tapered tourmaline crystals (Manning, 1982; Jolliff et al., 1986; Selway, 1999).

The textures of the large Ågskardet OQ5 and OQ6 tourmaline crystals represent complex crystallization and resorption processes. Ågskardet OQ5 shows elevated Rb and Cs contents in the tourmaline in contact with Rb- and Cs-enriched mica inclusions. This suggests interaction between the two phases. Most likely, tourmaline is replacing mica and inheriting some of its trace element content (Fig. A10). The Ca-rich green rim is clearly distinct from the rest of the pink crystal (Figs. 6C and A2). This is indicative of a resorption event rather than continuous crystallization. The complex crystal Ågskardet OQ6 contains multiple generations of tourmaline. Most of the grain with a euhedral tourmaline rim consists of mica fragments. An apparently younger generation of tourmaline, the rim, replaces or grows around earlier mica. The third generation is of a later stage, since it fills fractures within the mica fragments, between mica and tourmaline and within the tourmaline rim (Fig. A7). In major element composition, this third generation is similar to the outermost rim of the Ågskardet OQ5 crystal (Figs. A2, A7). The oldest generation of tourmaline might be the primary phase, which then

was partly replaced by mica. The complex texture of 'islands' and inclusions of tourmaline within the mica suggests this (Figs. 6D, 19, A4 and A7). The texture of this tourmaline crystal suggests changing conditions and several pulses of liquid. Multistage tourmaline growth is not uncommon in hydrothermal environments (Slack & Trumbull, 2011). Another possible explanation of the peculiar texture is selective replacement of the tourmaline core by mica, while the rim stayed intact. This could be due to a different chemical composition or a more porous structure of the core which was more susceptible to dissolution by hydrothermal fluids. This phenomenon has been observed in several evolved pegmatites, where the cores of zoned tourmalines have been replaced by quartz or lepidolite, while the rim stayed intact (Shigley et al., 2001; London, 2008). This explanation requires significantly different core and rim compositions to be feasible. Selective dissolution and precipitation of minerals in a pegmatite system can occur due to disequilibrium conditions, which lead to an oscillating system approaching a state of equilibrium between solid and fluid phases (Korzhinskiĭ, 1959; Burt, 1981; London, 1996; London, 2005). Repeated precipitation and dissolution of minerals, changing the mineral assemblage, has been proposed as one of the main processes during pegmatite magmatic-hydrothermal evolution (London, 1996; London, 2008). A third possible explanation is rapid crystallization of tourmaline from a highly supersaturated solution leading to rapid growth at crystal corners and along edges. This typically leads to skeletal growth, growth of hollow crystals and crystals filled by a different mineral, as observed for Ågskardet OQ2-4 tourmaline (Manning, 1982; Fenn, 1986; Jolliff et al., 1986).

Further observations include two generations of feldspar and late masses of tourmaline filling fractures in garnet in the Ågskardet OQ2-4 sample. This indicates the operation of late-stage processes and their influence on the final mineral assemblage, also involving disequilibrium processes during pegmatite evolution. For Ågskardet OQ2-4, both magmatic or late-stage magmatic to fluid-facilitated crystallization seem possible. The same is true for Grønnøya, where optically continuous inclusions in tourmaline and feldspar indicate two stages of crystal growth. The trace element patterns of tourmaline from the other pegmatite localities studied do not show indications of precipitation from hydrothermal fluids. It is more likely that a magmatic fluid was involved in the development of these textures. It should, therefore, be considered that a pegmatite system is more complex than early- to late-stage crystallization from a single melt. Dissolution and reprecipitation processes as well as coexisting immiscible phases likely play an important role in the formation and evolution of pegmatites (London, 1996; Thomas & Davidson, 2012).

7.2.3. Tourmaline trace element characteristics

Other indicators for involvement of an aqueous fluid in the formation of the late-stage tourmalines Ågskardet OQ5 and OQ6 are the highly elevated contents of Sr and Pb compared

to the other tourmaline samples (Fig. 10). The compositional difference is about one order of magnitude, possibly indicating precipitation from a fluid foreign to the dominant pegmatite magma, which may have leached Sr and Pb plus other elements from the host rock paragneisses and amphibolites. Caixeta Borges (2023) reported bulk rock Sr concentrations of 191 ppm for the amphibolite country rock, 153 ppm for banded gneisses and 140 ppm for the pegmatite, where the analyzed sample was a combined bulk powder from three different zones of the Ågskardet pegmatite. Our own unpublished bulk rock data from the intermediate zone of the pegmatite show a Sr concentration of <5 ppm and an average value of 190 ppm Sr for the basement TIB gneisses of the study area (Tappe et al., 2024, unpublished). For Pb concentrations, published and unpublished bulk rock data for the pegmatite, country rocks and basement gneisses range between 11 and 24 ppm. The large difference in Sr concentrations between the intermediate zone and the mixed bulk pegmatite might indicate enrichment of Sr in the late-stage minerals of the albite replacement zone. Incompatible elements, such as Sr and Pb, generally are expected to enrich in a highly fractionated melt. Ihlen (2004), however, reported very low Sr contents for feldspars from the Ågskardet OQ pegmatite core and higher contents for feldspars from the outer zones. This is somewhat expected due to the compatible nature of Sr in albite (e.g., Blundy & Wood, 1991). In the Varuträsk LCT pegmatite in Sweden, Siegel et al. (2016) observed increasing Pb and Sr concentrations from the wall zone to the outer intermediate zone, and Pb further increasing towards the core. For tourmalines from the border zone they report much higher Sr/Pb ratios, which they explain by Sr contamination from the amphibolite host rocks. The low Sr content in feldspars from the inner zones of the Ågskardet OQ pegmatite contrasts the elevated Sr contents of the tourmalines from Ågskardet OQ5 and OQ6, as enrichment in albite would be expected with Sr availability. Strontium concentrations are, however, expected to be higher in hydrothermally formed tourmaline due to Sr enrichment in high-salinity aqueous fluids or melts (Bai & Van Groos, 1999). This indicates crystallization of the Ågskardet OQ5 and OQ6 tourmalines from an exsolved or external fluid that was in contact with the host rocks.

The major element and B-isotopic compositions of the third generation tourmaline of Ågskardet OQ6 are quite similar to those of the tourmalines of Ågskardet OQ2, OQ3 and OQ4. The elevated Sr and Pb contents in Ågskardet OQ6, as well as the higher Zn contents in OQ2, OQ3 and OQ4, make it however unlikely that these crystallized at the same time from the same source fluid. According to Selway (1999), Zn contents in pegmatitic tourmaline initially increase from the border zone, until they reach their maximum in the inner wall zone. Then they decrease toward the core of the pegmatite. This is consistent with observations from the Ågskardet OQ pegmatite, where tourmalines from the outer zones (OQ1) have the highest average Zn contents of about 3000 ppm, the intermediate zone tourmalines (OQ2-4) have

average Zn contents of around 2000 ppm and the crystals from the inner zone (OQ5, OQ6) do not exceed 500 ppm (Fig. 9).

Vanadium is preferentially partitioned into tourmaline over the melt and is therefore only expected in tourmaline of the outer zone (Selway, 1999; Drivenes et al., 2015). This is not observed in the old quarry pegmatite, where tourmaline from the outer zone does not contain any V (i.e., below method detection limit). The intermediate zone tourmalines contain up to 7 ppm V, and OQ5 and OQ6 tourmalines contain up to 35 ppm V (Fig. 9). This could be explained by the abundant biotite in the outer zone (Caixeta Borges, 2023; Lomotey; 2023), which incorporates V (Drivenes et al., 2015). Marks et al. (2013) reported an increase in V from magmatic to hydrothermal tourmaline. They also report a decoupling of the V/Sc ratio in hydrothermal tourmaline. OQ5 and OQ6 tourmalines show a decoupled V/Sc ratio compared to all other samples, which supports their hydrothermal origin. The V/Sc ratio is increasing toward the outer rim. For Sn, a gradual increase in concentration between tourmaline of the outer zone and the crystals of OQ5 and OQ6 is observed. Beryllium increases slightly and Ga concentrations scatter (Fig. 9). The concentrations of all these trace elements are higher in the mica inclusions. Generally, most trace elements lack systematic trends in pegmatitic tourmaline, because they commonly are partitioned into mica and feldspar (e.g., Rb and Cs), apatite (REE) and (Nb,Ta)-oxides (Černý et al., 1985; Selway, 1999). The Li-muscovite inclusions in the tourmaline crystal from Ågskardet OQ5 have higher Li contents than any other micas from the Ågskardet OQ pegmatite studied by Lomotey (2023) and comparable Li contents to micas from the albite replacement zone studied by Caixeta Borges (2023). Li contents are greater in albitized than non-albitized pegmatites (Selway, 1999), but this does not indicate that all elbaite is of hydrothermal origin. The principal Li-minerals spodumene, petalite and lepidolite are in most cases considered to be of magmatic origin (London, 2008).

Another restricting factor in the interpretation of magmatic-hydrothermal interplay in the North Helgeland pegmatites (other than Ågskardet OQ) is the limited number of samples per pegmatite, which are mostly not linked to internal pegmatite zonation. Sampling of tourmaline from outer zones and the core or replacement zone, if possible, would have allowed for a comparison of compositional characteristics. It is evident that the Ørnes and Grønnøya pegmatites are also highly fractionated and enriched in certain rare elements. Due to limited outcrop conditions, mapping and sampling may not cover the existing compositional variation.

7.2.4. Constraints from boron isotope variations in tourmaline

The boron isotopic compositions of the large Ågskardet OQ6 crystal support the interpretation of several tourmaline generations formed during different growth events. The tourmaline ‘islands’ in the core have a light B-isotopic composition. The third tourmaline generation is

about 5‰ heavier and the margin shows a range of values, which get heavier toward the outer rim but are on average lighter than the third tourmaline generation (Figs. 19 and A13). This is consistent with the indications by textural and compositional observations for the crystallization sequence of the three generations. The comparatively narrow $\delta^{11}B$ range observed for the large Ågskardet OQ5 tourmaline crystal is similar to the range of values for the rim of the Ågskardet OQ6 crystal.

Based on the boron isotope fractionation trends outlined in Chapter 2.3., a possible interpretation of the $\delta^{11}B$ data for the old quarry pegmatite can be as follows:

The tourmalines from the outer pegmatite zone (Ågskardet OQ1), which crystallized first, have an average $\delta^{11}B$ value of -10.2 ± 0.2‰. According to the experimental study by Cheng et al. (2022), the temperature-dependent boron isotope fractionation between melt and tourmaline is $\Delta^{11}B_{melt-Tur}$ = +0.90 ± 0.05‰ at 660°C. Their experiments were performed between 660 and 800°C. If we extrapolate their results to 585°C, which is our oxygen thermometry result for Ågskardet OQ1, then a fractionation factor of $\Delta^{11}B_{melt-Tur}$ = +1.31‰ is obtained. Note that extrapolation beyond the tested temperature range should be treated with caution. Tourmalines from Ågskardet OQ2-4 have a combined average $\delta^{11}B$ value of -9.2 ± 0.6‰. This fits well with the assumption that these tourmalines crystallized from the same melt as OQ1 at a later stage when it had been further fractionated, as also supported by their major and trace element compositions. Uncertainties may stem from the accuracy of the temperature estimate, the mentioned extrapolation of the isotope fractionation factor, the relative timing of crystallization, and the analytical error of 0.91‰ of the SIMS-determined boron isotope data.

A 4 to 5‰ difference in $\delta^{11}B$ is observed between tourmalines from Ågskardet OQ2-4 and tourmaline cores in Ågskardet OQ5 and OQ6. As mentioned, the boron isotopic composition of Ågskardet OQ6 is rather heterogeneous. The Ågskardet OQ5 tourmaline shows a trend of increasing $\delta^{11}B$ values from -13.5 to -10‰ from core to rim. The $\delta^{11}B$ increase from core to rim is consistent with crystallization from an evolving hydrothermal fluid. Although boron is in trigonal coordination in both the tourmaline structure and in fluids, minor isotopic fractionation is expected ($\Delta^{11}B_{fluid-Tur}$ = +1.6 to +2.3‰ at 550 to 440°C; Meyer et al., 2008). Combined with the observed textures and measured trace element compositions, the boron isotopic compositions of the large Ågskardet OQ5 and OQ6 tourmaline crystals suggest a hydrothermal origin. Alternatively, the increasing $\delta^{11}B$ values from core to rim may record continued crystal growth from an increasingly differentiated granitic melt that underwent significant mica crystallization among other phases in which boron is tetrahedrally coordinated. Micas occur in all pegmatite zones at Ågskardet, from the wall zone to the late-stage albite replacement zone (Caixeta Borges, 2023), but their abundance has not been quantified. Siegel et al. (2016)

explained a 5‰ shift in $\delta^{11}B$ between two tourmaline types in the Varuträsk pegmatite in Sweden by co-crystallization of muscovite. These two main hypotheses may apply to Ågskardet, but they cannot explain the elevated Sr and Pb contents of the OQ5 and OQ6 tourmalines, which appear to require input from an external fluid component (i.e., contamination).

A remaining question is why the boron isotopic compositions of the cores of the two large crystals are relatively light. There are several options to explain this. The first option is abundant crystallization of tourmaline, which was described by Trumbull et al. (2008, 2013), Drivenes et al. (2015) and Siegel et al. (2016) to lead to a shift in $\delta^{11}B$ toward lower values in the residual melt. This option is, however, inconsistent with the newer experimental data by Cheng et al. (2022). A second possibility is the exsolution of an aqueous fluid from the granitic melt. The ^{11}B isotope would partition preferentially into the fluid and tourmaline crystallizing from the melt would inherit a lighter $\delta^{11}B$ signature. This explanation requires that the cores of the tourmalines are of magmatic origin, which is not in agreement with the earlier interpretation of the elevated trace element contents (see Chapter 7.2.3.). A solution could be a scenario where immiscible melt-melt-liquid coexist. For example, a low-viscosity hydrosaline melt (i.e., brine melt) could transport trace elements, while a coexisting aqueous fluid would be enriched in ^{11}B, especially if of low alkalinity. A third option is the influence of fluids external to the pegmatite system. These would lead to a change in isotopic signature and could also explain the different trace element signatures of the different tourmaline generations.

8. Summary and conclusions

The results of and findings from this MSc project can be summarized as follows:

- Tourmalines from Ågskardet OQ show an evolution from vacancy-rich schorl to Na-rich and Ca-bearing schorl and fluor-schorl to elbaite, fluor-elbaite, tsilaisite and fluor-liddicoatite. Tourmalines from Grønnøya and Ørnes are Na-rich schorls and tourmalines from Ågskardet UB mainly show dravitic compositions.
- Garnets from the North Helgeland pegmatites are dominated by almandine and spessartine components and are enriched in HREE in all localities except for Ågskardet OQ.
- The B-isotopic composition of tourmaline from the two pegmatite bodies in Ågskardet is similar to average values for S-type granites reported in the literature. Slightly heavier values for the pegmatites in Grønnøya and Ørnes can be explained by a larger, but limited fraction of I-type granitic basement in the magma source.

- Results from triple oxygen isotope analyses of pegmatitic garnet indicate low-temperature fractionation of oxygen, which is in agreement with a metasedimentary melt source. The δ18O values of those garnets, however, do not preclude the basement orthogneisses as protoliths.
- An exception to these two trends defined by oxygen isotope characteristics is the Neverdalen locality, where the light O-isotopic signature could reflect influence of heated meteoric water. Additionally, the Neverdalen pegmatite shows anomalous major and trace element compositions compared to the other pegmatites.
- Oxygen isotope thermometry yielded a higher apparent temperature for Neverdalen than for Ågskardet OQ and Grønnøya and indicates disequilibrium conditions for Ågskardet UB.
- Many of the textural and compositional features the textural and compositional features observed for the Ågskardet OQ pegmatite can be explained by involvement of more than one melt or fluid phase.
- The B-isotopic and trace element characteristics of late-stage tourmaline suggest co-existence of a silicic and a hydrosaline melt. Early-magmatic minerals seem to have crystallized from a silicic melt.

The two main aims of this MSc study were to i) investigate the origin and evolution of the parental magmas to the Helgeland pegmatite bodies to better understand their tectonic setting, and ii) understand the role of melt-fluid interactions and volatile fluxes in highly evolved magmatic or magmatic-hydrothermal systems and their effect on rare-element mineralization processes in the resultant pegmatite bodies.

The here proposed formation of the North Helgeland pegmatites by partial melting of varying amounts of Paleoproterozoic I-type orthogneisses and Paleoproterozoic metasedimentary rocks in a mostly post-collisional tectonic environment during the Caledonian orogeny is supported by B- and O- isotope data, as well as by the trace element signatures of the pegmatitic minerals. This is in agreement with pegmatite U-Pb ages of 422 ± 5 to 387 ± 6 Ma. The crustal source was rather heterogeneous and it is not straightforward to pinpoint specific basement lithologies as melt sources in the study area. However, magma contamination by the wall-rocks during emplacement is possible for some of the pegmatite bodies.

The genetic sequence in the Ågskardet OQ pegmatite is interpreted as a first stage crystallization of the main mineral assemblage from a viscous silicic melt, a second stage of albitization and late tourmaline and mica growth from a hydrosaline melt, and potentially a third stage dominated by an aqueous fluid, which might have induced the compositional changes in

the rims of late tourmalines. Tourmalines and micas crystallized during the second stage have higher Li contents than tourmalines and micas from the first stage. In terms of rare-element mineralization, significance can be attributed to this second stage and possibly also to the third stage. Zones of albitization in evolved pegmatites might therefore be a favorable target for rare-metal exploration.

9. Outlook

To gain a more complete picture on potential magma sources to the North Helgeland pegmatites, more metasediments in the study area could be sampled for oxygen isotope analysis. The TIB gneisses as main source to the melts are unlikely, and additional investigation could help identify further influences and sources of rare-element enrichments. Detailed mapping, lithostratigraphic work and analysis of the internal tectonic structure of the potential source metasedimentary units, if exposed, would help to gain a better understanding. Based on geochemical major and trace element investigations of the potential source rocks and constraints on pressure and temperature during melt formation and emplacement, melt fractionation and transfer could be modeled.

Additional future research on the North Helgeland pegmatite field could be directed towards melt and fluid inclusions. This could help to gain a better understanding of the role of water and volatile flux contents and of fluid-fluid and fluid-solid interactions in the Helgeland pegmatites. To evaluate the hydrothermal influence on the pegmatite assemblages, cathodoluminescence imaging of quartz occurring together with tourmaline could be helpful. Additionally, O-isotope analysis of feldspar could yield information because the mineral's low closure temperature would record changes in isotope composition resulting from hydrothermal alteration. Multiple isotope system studies could be applied not only to tourmaline, but also other pegmatitic minerals, such as mica. Mica can be both magmatic and hydrothermal, and is like tourmaline an important host of boron, oxygen, hydrogen and lithium. Analysis of B-isotopes in micas co-crystallizing with tourmaline would be a great help in interpreting fractionation patterns and can even be employed for muscovite-tourmaline boron isotope thermometry (Codeço et al., 2019). Concerning B-isotope fractionation behavior, more experimental work on the partitioning between minerals and melt, melts and fluids and minerals and fluids would be needed, because the number of existing studies is small and the results are somewhat contradictory.

10. References

Acosta-Vigil, A., Buick, I., Hermann, J., Cesare, B., Rubatto, D., London, D., & Morgan, G. B. (2010). Mechanisms of crustal anatexis: a geochemical study of partially melted metapelitic enclaves and host dacite, SE Spain. *Journal of Petrology*, *51*(4), 785-821.

Adamson, O. J., & Neumann, H. (1951). *Preliminary review of mineral deposits i Northern Norway* (BA 3961).

Agyei-Dwarko, N., Augland, L., & Andresen, A. (2012). The Heggmovatn supracrustals, North Norway—a late Mesoproterozoic to early Neoproterozoic (1050–930 Ma) terrane of Laurentian origin in the Scandinavian Caledonides. *Precambrian Research*, *212*, 245-262.

Akizuki, M., Kuribayashi, T., Nagase, T., & Kitakaze, A. (2001). Triclinic liddicoatite and elbaite in growth sectors of tourmaline from Madagascar. *American Mineralogist*, *86*(3), 364-369.

Anderson, J. L. (2012). Cold pegmatites. *Elements*, *8*(4), 248-249.

Andréasson, P. (1994). The Baltoscandian margin in Neoproterozoic-early Palaeozoic times. Some constraints on terrane derivation and accretion in the Arctic Scandinavian Caledonides. *Tectonophysics*, *231*(1-3), 1-32.

Andresen, A., & Tull, J. F. (1986). Age and tectonic setting of the Tysfjord gneiss granite, Efjord, North Norway. *Norsk Geologisk Tidsskrift*, *66*, 69-80.

Angert, A., Rachmilevitch, S., Barkan, E., & Luz, B. (2003). Effects of photorespiration, the cytochrome pathway, and the alternative pathway on the triple isotopic composition of atmospheric O2. *Global Biogeochemical Cycles*, *17*(1).

Audétat, A., & Edmonds, M. (2020). Magmatic-hydrothermal fluids. *Elements: An International Magazine of Mineralogy, Geochemistry, and Petrology*, *16*(6), 401-406.

Bai, T., & Van Groos, A. K. (1999). The distribution of Na, K, Rb, Sr, Al, Ge, Cu, W, Mo, La, and Ce between granitic melts and coexisting aqueous fluids. *Geochimica Et Cosmochimica Acta*, *63*(7-8), 1117-1131.

Bakker, R. J., & Elburg, M. A. (2006). A magmatic-hydrothermal transition in Arkaroola (northern Flinders Ranges, South Australia): from diopside–titanite pegmatites to hematite–quartz growth. *Contributions to Mineralogy and Petrology*, *152*, 541-569.

Baldwin, J. R., & von Knorring, O. (1983). Compositional range of Mn-garnet in zoned granitic pegmatites. *The Canadian Mineralogist*, *21*(4), 683-688.

Ballouard, C., Elburg, M., Tappe, S., Reinke, C., Ueckermann, H., & Doggart, S. (2020a). Magmatic-hydrothermal evolution of rare metal pegmatites from the Mesoproterozoic Orange River pegmatite belt (Namaqualand, South Africa). *Ore Geology Reviews*, *116*, 103252.

Ballouard, C., Massuyeau, M., Elburg, M. A., Tappe, S., Viljoen, F., & Brandenburg, J.-T. (2020b). The magmatic and magmatic-hydrothermal evolution of felsic igneous rocks as seen through Nb-Ta geochemical fractionation, with implications for the origins of rare-metal mineralizations. *Earth-Science Reviews*, *203*, 103115.

Bao, H., Thiemens, M. H., Farquhar, J., Campbell, D. A., Lee, C. C.-W., Heine, K., & Loope, D. B. (2000). Anomalous 17O compositions in massive sulphate deposits on the Earth. *Nature*, *406*(6792), 176-178.

Barkan, E., & Luz, B. (2005). High precision measurements of 17O/16O and 18O/16O ratios in H2O. *Rapid Communications in Mass Spectrometry: An International Journal Devoted to the Rapid Dissemination of Up-to-the-Minute Research in Mass Spectrometry*, *19*(24), 3737-3742.

Barnes, C. G., Dumond, G., Yoshinobu, A., & Prestvik, T. (2004). Assimilation and crystal accumulation in a mid-crustal magma chamber: the Sausfjellet pluton, north-central Norway. *Lithos*, *75*(3-4), 389-412.

Barnes, C. G., Frost, C. D., Yoshinobu, A. S., McArthur, K., Barnes, M. A., Allen, C. M., Nordgulen, Ø., & Prestvik, T. (2007). Timing of sedimentation, metamorphism, and plutonism in the Helgeland Nappe Complex, north-central Norwegian Caledonides. *Geosphere*, *3*(6), 683-703.

Barnes, C. G., & Prestvik, T. (2000). Conditions of pluton emplacement and anatexis in the Caledonian Bindal Batholith, north-central Norway. *Norsk Geologisk Tidsskrift*, *80*(4), 259-274.

Barth, S. (1993). Boron isotope variations in nature: a synthesis. *Geologische Rundschau*, *82*, 640-651.

Baxter, E. F., Caddick, M. J., & Ague, J. J. (2013). Garnet: Common mineral, uncommonly useful. *Elements*, *9*(6), 415-419.

Baxter, E. F., Caddick, M. J., & Dragovic, B. (2017). Garnet: A rock-forming mineral petrochronometer. *Reviews in Mineralogy and Geochemistry*, *83*(1), 469-533.

Baxter, E. F., & Scherer, E. E. (2013). Garnet geochronology: timekeeper of tectonometamorphic processes. *Elements*, *9*(6), 433-438.

Berndt, J., & Klemme, S. (2022). Origin of carbonatites—liquid immiscibility caught in the act. *Nature Communications*, *13*(1), 2892.

Bhattacharya, S., & Thiemens, M. H. (1988). Isotopic fractionation in ozone decomposition. *Geophysical Research Letters*, *15*(1), 9-12.

Bindeman, I. N. (2008). Oxygen isotopes in mantle and crustal magmas as revealed by single crystal analysis. *Reviews in Mineralogy and Geochemistry*, *69*(1), 445-478.

Bindeman, I. N. (2021). Triple oxygen isotopes in evolving continental crust, granites, and clastic sediments. *Reviews in Mineralogy and Geochemistry*, *86*(1), 241-290.

Bindeman, I. N., & Pack, A. (2021). *Triple oxygen isotope geochemistry* (Vol. 86). Walter de Gruyter GmbH & Co KG.

Bingen, B., & Solli, A. (2009). Geochronology of magmatism in the Caledonian and Sveconorwegian belts of Baltica: synopsis for detrital zircon provenance studies. *Norwegian Journal of Geology/Norsk Geologisk Forening*, *89*(4).

Blundy, J. D., & Wood, B. J. (1991). Crystal-chemical controls on the partitioning of Sr and Ba between plagioclase feldspar, silicate melts, and hydrothermal solutions. *Geochimica Et Cosmochimica Acta*, *55*(1), 193-209.

Bosi, F., Andreozzi, G. B., Agrosì, G., & Scandale, E. (2015). Fluor-tsilaisite, NaMn3Al6 (Si6O18)(BO3) 3 (OH) 3F, a new tourmaline from San Piero in Campo (Elba, Italy) and new data on tsilaisitic tourmaline from the holotype specimen locality. *Mineralogical Magazine*, *79*(1), 89-101.

Bottinga, Y., & Javoy, M. (1975). Oxygen isotope partitioning among the minerals in igneous and metamorphic rocks. *Reviews of Geophysics*, *13*(2), 401-418.

Bradley, D. C. (2019). Tectonic and paleoclimatic controls of lithium-cesium-tantalum (LCT) pegmatite genesis, exhumation, and preservation in the Appalachians. *The Canadian Mineralogist*, *57*(5), 715-717.

Bucholz, C. E., Jagoutz, O., VanTongeren, J. A., Setera, J., & Wang, Z. (2017). Oxygen isotope trajectories of crystallizing melts: insights from modeling and the plutonic record. *Geochimica Et Cosmochimica Acta*, *207*, 154-184.

Burt, D. M. (1981). Acidity-salinity diagrams; application to greisen and porphyry deposits. *Economic Geology*, *76*(4), 832-843.

Caixeta Borges, P. (2023). *The mineralogy of the Ågskardet lithium pegmatite at Meløy in Nordland, Norway* MSc thesis, Universitetet i Oslo].

Cameron, E. N., Jahns, R. H., McNair, A. H., & Page, L. R. (1949). Internal structure of granitic pegmatites.

Cao, X., & Liu, Y. (2011). Equilibrium mass-dependent fractionation relationships for triple oxygen isotopes. *Geochimica Et Cosmochimica Acta*, *75*(23), 7435-7445.

Catanzaro, E., Champion, C., Garner, E., Marinenko, G., Sappenfield, K., & Shields, W. (1970). Boric acid: isotopic and assay standard reference materials. National Bureau of Standards. *Institute for Materials Research, USA*, *10*, 17-260.

Černý, P. (1991). Rare-element granite pegmatites. Part I: anatomy and internal evolution of pegmatite deposits. Part II: regional to global relationships and petrogenesis. *Geoscience Canada*, *18*(2), 49-81.

Černý, P., & Burt, D. (1984). Paragenesis, crystallochemical characteristics, and geochemical evolution in micas in granite pegmatites. In *Micas* (pp. 257-297). Reviews in Mineralogy, Vol. 13, Min. Soc. America.

Černý, P., Chapman, R., Teertstra, D. K., & Novák, M. (2003). Rubidium-and cesium-dominant micas in granitic pegmatites. *American Mineralogist*, *88*(11-12), 1832-1835.

Černý, P., & Ercit, T. S. (2005). The classification of granitic pegmatites revisited. *The Canadian Mineralogist*, *43*(6).

Černý, P., London, D., & Novák, M. (2012). Granitic pegmatites as reflections of their sources. *Elements*, *8*(4), 289-294.

Cerny, P., Meintzer, R. E., & Anderson, A. J. (1985). Extreme fractionation in rare-element granitic pegmatites; selected examples of data and mechanisms. *The Canadian Mineralogist*, *23*(3), 381-421.

Chacko, T., Cole, D. R., & Horita, J. (2001). Equilibrium oxygen, hydrogen and carbon isotope fractionation factors applicable to geologic systems. *Reviews in Mineralogy and Geochemistry*, *43*(1), 1-81.

Chakraborty, S., Yanchulova, P., & Thiemens, M. H. (2013). Mass-independent oxygen isotopic partitioning during gas-phase SiO2 formation. *Science*, *342*(6157), 463-466.

Chaussidon, M., & Albarède, F. (1992). Secular boron isotope variations in the continental crust: an ion microprobe study. *Earth and Planetary Science Letters*, *108*(4), 229-241.

Cheng, L., Zhang, C., Li, X., Almeev, R. R., Yang, X., & Holtz, F. (2019). Improvement of electron probe microanalysis of boron concentration in silicate glasses. *Microscopy and Microanalysis*, *25*(4), 874-882.

Cheng, L., Zhang, C., Liu, X., Yang, X., Zhou, Y., Horn, I., Weyer, S., & Holtz, F. (2021). Significant boron isotopic fractionation in the magmatic evolution of Himalayan leucogranite recorded in multiple generations of tourmaline. *Chemical Geology*, *571*, 120194.

Cheng, L., Zhang, C., Zhou, Y., Horn, I., Weyer, S., & Holtz, F. (2022). Experiments reveal enrichment of 11B in granitic melt resulting from tourmaline crystallisation. *Geochemical perspectives letters 20 (2022)*, *20*, 37-42.

Christiansen, E. H., Haapala, I., & Hart, G. L. (2007). Are Cenozoic topaz rhyolites the erupted equivalents of Proterozoic rapakivi granites? Examples from the western United States and Finland. *Lithos*, *97*(1-2), 219-246.

Clayton, R. N., Grossman, L., & Mayeda, T. K. (1973). A component of primitive nuclear composition in carbonaceous meteorites. *Science*, *182*(4111), 485-488.

Clemens, J., & Stevens, G. (2012). What controls chemical variation in granitic magmas? *Lithos*, *134*, 317-329.

Codeço, M. S., Weis, P., Trumbull, R. B., Glodny, J., Wiedenbeck, M., & Romer, R. L. (2019). Boron isotope muscovite-tourmaline geothermometry indicates fluid cooling during magmatic-hydrothermal W-Sn ore formation. *Economic Geology*, *114*(1), 153-163.

Coghlan, R. A. N. (1990). *Studies in diffusional transport: Grain boundary transport of oxygen in feldspars, diffusion of oxygen, strontium and the REEs in garnet, and thermal histories of granitic intrusions in south-central Maine using oxygen isotopes* [Doctoral Dissertation, Brown University].

Corfu, F., Andersen, T., & Gasser, D. (2014). The Scandinavian Caledonides: main features, conceptual advances and critical questions. *Geological Society, London, Special Publications*, *390*(1), 9-43.

Corfu, F., Gerber, M., Andersen, T., Torsvik, T., & Ashwal, L. (2011). Age and significance of Grenvillian and Silurian orogenic events in the Finnmarkian Caledonides, northern Norway. *Canadian Journal of Earth Sciences*, *48*(2), 419-440.

Craig, H. (1957). Isotopic standards for carbon and oxygen and correction factors for mass-spectrometric analysis of carbon dioxide. *Geochimica Et Cosmochimica Acta*, *12*(1-2), 133-149.

Cribb, S. J. (1981). Rb-Sr geochronological evidence suggesting a reinterpretation of part of the north Norwegian Caledonides. *Norsk Geologisk Tidsskrift*(61), 97–110.

Cuney, M., & Barbey, P. (2014). Uranium, rare metals, and granulite-facies metamorphism. *Geoscience Frontiers*, *5*(5), 729-745. https://doi.org/10.1016/j.gsf.2014.03.011

Dahl, P. S., Wehn, D. C., & Feldmann, S. G. (1993). The systematics of trace-element partitioning between coexisting muscovite and biotite in metamorphic rocks from the Black Hills, South Dakota, USA. *Geochimica Et Cosmochimica Acta*, *57*(11), 2487-2505.

Dai, Z., Li, G., Ding, J., Zhang, L., Cao, H., & Zhang, Z. (2019). Chemical and boron isotopic composition, and significance of tourmaline from the Conadong Tourmaline Granite. *Earth Scie*, *44*(6). https://doi.org/doi:10.3799/dqkx.2019.043

Dill, H. G. (2015). Pegmatites and aplites: Their genetic and applied ore geology. *Ore Geology Reviews*, *69*, 417-561.

Dodson, M. H. (1973). Closure temperature in cooling geochronological and petrological systems. *Contributions to Mineralogy and Petrology*, *40*(3), 259-274.

Dorais, M. J., & Tubrett, M. (2012). Detecting peritectic garnet in the peraluminous Cardigan Pluton, New Hampshire. *Journal of Petrology*, *53*(2), 299-324.

Drivenes, K., Larsen, R. B., Müller, A., Sørensen, B. E., Wiedenbeck, M., & Raanes, M. P. (2015). Late-magmatic immiscibility during batholith formation: assessment of B isotopes and trace elements in tourmaline from the Land's End granite, SW England. *Contributions to Mineralogy and Petrology*, *169*, 1-27.

Drivenes, K., Sørensen, B. E., & Larsen, R. B. (2016). Orogenic degassing, scapolitization and K-metasomatism during Caledonian exhumation, Helgeland, Norway. *Norwegian Journal of Geology*, *96*(3).

Dutrow, B. L., & Henry, D. J. (2011). Tourmaline: a geologic DVD. *Elements*, *7*(5), 301-306.

Eiler, J. M. (2001). Oxygen isotope variations of basaltic lavas and upper mantle rocks. *Reviews in Mineralogy and Geochemistry*, *43*(1), 319-364.

Eiler, J. M., Valley, J. W., & Baumgartner, L. P. (1993). A new look at stable isotope thermometry. *Geochimica Et Cosmochimica Acta*, *57*(11), 2571-2583.

Erdmann, S., Jamieson, R. A., & MacDonald, M. A. (2009). Evaluating the origin of garnet, cordierite, and biotite in granitic rocks: a case study from the South Mountain Batholith, Nova Scotia. *Journal of Petrology*, *50*(8), 1477-1503.

Farquhar, J., Chacko, T., & Ellis, D. J. (1996). Preservation of oxygen isotope compositions in granulites from Northwestern Canada and Enderby Land, Antarctica: implications for high-temperature isotopic thermometry. *Contributions to Mineralogy and Petrology*, *125*(2), 213-224.

Farver, J. R. (2010). Oxygen and hydrogen diffusion in minerals. *Reviews in Mineralogy and Geochemistry*, *72*(1), 447-507.

Feng, Y., Cen, J., Liang, T., Wang, M., Tan, X., Hao, Y., & Yan, S. (2023). Lithium, Phosphorus, and rare earth elements in magmatic garnets from granitic Pegmatites: Coupled substitution and petrogenetic implications. *Ore Geology Reviews*, *153*, 105284.

Fenn, P. M. (1986). On the origin of graphic granite. *American Mineralogist*, *71*(3-4), 325-330.

Flemetakis, S., Berndt, J., Klemme, S., Genske, F., Cadoux, A., Louvel, M., & Rohrbach, A. (2020). An improved electron microprobe method for the analysis of halogens in natural silicate glasses. *Microscopy and Microanalysis*, *26*(5), 857-866.

Foord, E. E., Starkey, H. C., & Taggart, J. E. (1986). Mineralogy and paragenesis of “pocket” clays and associated minerals in complex granitic pegmatites, San Diego County, California. *American Mineralogist*, *71*(3-4), 428-439.

Gao, S., Luo, T.-C., Zhang, B.-R., Zhang, H.-F., Han, Y.-w., Zhao, Z.-D., & Hu, Y.-K. (1998). Chemical composition of the continental crust as revealed by studies in East China. *Geochimica Et Cosmochimica Acta*, *62*(11), 1959-1975.

Garlick, G. D., & Epstein, S. (1967). Oxygen isotope ratios in coexisting minerals of regionally metamorphosed rocks. *Geochimica Et Cosmochimica Acta*, *31*(2), 181-214.

Gat, J. R. (1996). Oxygen and hydrogen isotopes in the hydrologic cycle. *Annual Review of Earth and Planetary Sciences*, *24*(1), 225-262.

Gee, D. G., Fossen, H., Henriksen, N., & Higgins, A. K. (2008). From the early Paleozoic platforms of Baltica and Laurentia to the Caledonide Orogen of Scandinavia and Greenland. *Episodes Journal of International Geoscience*, *31*(1), 44-51.

Gee, D. G., & Sturt, B. A. (1985). *The Caledonide orogen: Scandinavia and related areas*. Wiley.

Geller, S., & Miller, C. (1959). Silicate garnet—yttrium-iron garnet solid solutions. *American Mineralogist: Journal of Earth and Planetary Materials*, *44*(11-12), 1115-1120.

Giletti, B. J. (1986). Diffusion effects on oxygen isotope temperatures of slowly cooled igneous and metamorphic rocks. *Earth and Planetary Science Letters*, *77*(2), 218-228.

Goodfriend, G. A. (1999). Terrestrial stable isotope records of Late Quaternary paleoclimates in the eastern Mediterranean region. *Quaternary Science Reviews*, *18*(4-5), 501-513.

Gou, G.-N., Wang, Q., Wyman, D. A., Xia, X.-P., Wei, G.-J., & Guo, H.-F. (2017). In situ boron isotopic analyses of tourmalines from Neogene magmatic rocks in the northern and southern margins of Tibet: Evidence for melting of continental crust and sediment recycling. *Solid Earth Sciences*, *2*(2), 43-54.

Grew, E. S., & Anovitz, L. (1996). Borosilicates (exclusive of tourmaline) and boron in rock-forming minerals in metamorphic environments. *Reviews in Mineralogy*, *33*, 387-502.

Grew, E. S., Locock, A. J., Mills, S. J., Galuskina, I. O., Galuskin, E. V., & Hålenius, U. (2013). Nomenclature of the garnet supergroup. *American Mineralogist*, *98*(4), 785-811.

Gustavson, M. (1996). Geologisk kart over Norge. Berggrunnskart Sulitjelma, M 1:250,000. In: Norges Geologiske Undersøkelse.

Gustavson, M., & Gjelle, S. (1991). Geologisk kart over Norge. Berggrunnskart Mo i Rana, M 1:250,000. In: Norges Geologiske Undersøkelse.

Han, J., Hollings, P., Jourdan, F., Zeng, Y., & Chen, H. (2020). Inherited Eocene magmatic tourmaline captured by the Miocene Himalayan leucogranites. *American Mineralogist*, *105*(9), 1436-1440.

Harris, C., & Vogeli, J. (2010). Oxygen isotope composition of garnet in the Peninsula Granite, Cape Granite Suite, South Africa: constraints on melting and emplacement mechanisms. *South African Journal of Geology*, *113*(4), 401-412.

Hatert, F., & Burke, E. A. (2008). The IMA–CNMNC dominant-constituent rule revisited and extended. *The Canadian Mineralogist*, *46*(3), 717-728.

Hawthorne, F. C., Burns, P. C., & Grice, J. D. (1996). The crystal chemistry of boron. *Reviews in Mineralogy*, *33*, 41-116.

Hawthorne, F. C., & Dirlam, D. M. (2011). Tourmaline the indicator mineral: From atomic arrangement to Viking navigation. *Elements*, *7*(5), 307-312.

Hawthorne, F. C., & Henry, D. J. (1999). Classification of the minerals of the tourmaline group.

Henry, D. J., Novák, M., Hawthorne, F. C., Ertl, A., Dutrow, B. L., Uher, P., & Pezzotta, F. (2011). Nomenclature of the tourmaline-supergroup minerals. *American Mineralogist*, *96*(5-6), 895-913. https://doi.org/10.2138/am.2011.3636

Hoefs, J. (2018). *Stable isotope geochemistry* (8 ed.). Springer.

Hoffbauer, R., Hoernes, S., & Fiorentini, E. (1994). Oxygen isotope thermometry based on a refined increment method and its application to granulite-grade rocks from Sri Lanka. *Precambrian Research*, *66*(1-4), 199-220.

Hu, G., Gao, L. e., Zeng, L., & LI, Y. (2022). Geochemical and boron isotopic evidence that tourmaline records country rock assimilation of leucogranites in the Himalayan orogen. *Acta Geologica Sinica-English Edition*, *96*(1), 123-134.

Hu, G., Zeng, L., Gao, L.-E., Liu, Q., Chen, H., & Guo, Y. (2018). Diverse magma sources for the Himalayan leucogranites: Evidence from B-Sr-Nd isotopes. *Lithos*, *314*, 88-99.

Hulsbosch, N., Boiron, M.-C., Thomas, R., Van Daele, J., Dewaele, S., & Muchez, P. (2019). Evaluation of the petrogenetic significance of melt inclusions in pegmatitic schorl-dravite from graphic tourmaline-quartz assemblages: Application of LA-ICP-QMS analyses and volume ratio calculations. *Geochimica Et Cosmochimica Acta*, *244*, 308-335.

Husdal, T., Müller, A., Olerud, S., Øivind, T., & Müller, A. (2017). Pegmatites of the Tysfjord-Hamarøy area, northern Norway. Müller, A. *Norwegian pegmatites. Tysfjord Hamarøy, Evje-Iveland, Langesundsfjord*. (3-47). Geological Society of Norway. 3-47.

Högdahl, K., Andersson, U. B., & Eklund, O. (2004). *The Transscandinavian Igneous Belt (TIB) in Sweden: a review of its character and evolution* (Vol. 37). Geological survey of Finland Espoo.

Högdahl, K., & Sjöström, H. (2001). Evidence for 1.82 Ga transpressive shearing in a 1.85 Ga granitoid in central Sweden: implications for the regional evolution. *Precambrian Research*, *105*(1), 37-56.

Haapala, I., Frindt, S., & Kandara, J. (2007). Cretaceous Gross Spitzkoppe and Klein Spitzkoppe stocks in Namibia: Topaz-bearing A-type granites related to continental rifting and mantle plume. *Lithos*, *97*(1-2), 174-192.

Ihlen, P. M. (2004). *Undersøkelse av Li-pegmatitter i Nord-Helgeland* (0800-3416).

Irber, W. (1999). The lanthanide tetrad effect and its correlation with K/Rb, Eu/Eu∗, Sr/Eu, Y/Ho, and Zr/Hf of evolving peraluminous granite suites. *Geochimica Et Cosmochimica Acta*, *63*(3-4), 489-508.

Jaffe, H. W. (1951). The role of yttrium and other minor elements in the garnet group. *American Mineralogist: Journal of Earth and Planetary Materials*, *36*(1-2), 133-155.

Jahns, R. (1982). Internal evolution of pegmatite bodies. *Granitic pegmatites in science and industry*, 293-328.

Jahns, R. H., & Burnham, C. W. (1969). Experimental studies of pegmatite genesis; I, A model for the derivation and crystallization of granitic pegmatites. *Economic Geology*, *64*(8), 843-864.

Jiang, S.-Y., & Palmer, M. R. (1998). Boron isotope systematics of tourmaline from granites and pegmatites: a synthesis. *European Journal of Mineralogy*, *10*, 1253-1266.

Jolliff, B. L., Papike, J. J., & Shearer, C. K. (1986). Tourmaline as a recorder of pegmatite evolution; Bob Ingersoll pegmatite, Black Hills, South Dakota. *American Mineralogist*, *71*(3-4), 472-500.

Kaeter, D., Barros, R., Menuge, J. F., & Chew, D. M. (2018). The magmatic–hydrothermal transition in rare-element pegmatites from southeast Ireland: LA-ICP-MS chemical mapping of muscovite and columbite–tantalite. *Geochimica Et Cosmochimica Acta*, *240*, 98-130.

Kakihana, H., Kotaka, M., Satoh, S., Nomura, M., & Okamoto, M. (1977). Fundamental studies on the ion-exchange separation of boron isotopes. *Bulletin of the chemical society of Japan*, *50*(1), 158-163.

Kile, D. E., & Foord, E. E. (1998). Micas from the Pikes Peak Batholith and its cogenetic granitic pegmatites, Colorado; optical properties, composition, and correlation with pegmatite evolution. *The Canadian Mineralogist*, *36*(2), 463-482.

King, E. M., & Valley, J. W. (2001). The source, magmatic contamination, and alteration of the Idaho batholith. *Contributions to Mineralogy and Petrology*, *142*(1), 72-88.

King, P. L., White, A. J. R., Chappell, B. W., & Allen, C. M. (1997). Characterization and origin of aluminous A-type granites from the Lachlan Fold Belt, southeastern Australia. *Journal of Petrology*, *38*(3), 371-391.

Klemme, S., Marschall, H. R., Jacob, D. E., Prowatke, S., & Ludwig, T. (2011). Trace-element partitioning and boron isotope fractionation between white mica and tourmaline. *The Canadian Mineralogist*, *49*(1), 165-176.

Koch, P. L. (1998). Isotopic reconstruction of past continental environments. *Annual Review of Earth and Planetary Sciences*, *26*(1), 573-613.

Kohn, M. J. (1999). Why most “dry” rocks should cool “wet”. *American Mineralogist*, *84*(4), 570-580.

Kohn, M. J., & Valley, J. W. (1998). Obtaining equilibrium oxygen isotope fractionations from rocks: theory and examples. *Contributions to Mineralogy and Petrology*, *132*(3), 209-224.

Kolitsch, U., Andresen, P., Husdal, T. A., Ertl, A., Haugen, A., Ellingsen, H., Larsen, A., & Skrift, N. B. (2013). Tourmaline-group minerals from Norway, part II: occurrences of luinaite-(OH) in Tvedalen, Larvik and Porsgrunn, and fluor-liddicoatite, fluor-elbaite and fluor-schorl at Ågskardet, Nordland. *Norsk Bergverksmuseet Skrift*, *50*, 23-41.

Kontak, D. J., Creaser, R. A., Heaman, L. M., & Archibald, D. A. (2005). U-Pb tantalite, Re-Os molybdenite, and 40Ar/39Ar muscovite dating of the Brazil Lake pegmatite, Nova Scotia: a possible shear-zone related origin for an LCT-type pegmatite. *Atlantic Geology*, *41*(1), 17-29.

Konzett, J., Hauzenberger, C., Ludwig, T., & Stalder, R. (2018). Anatectic Granitic Pegmatites from the Eastern Alps: A Case of Variable Rare Metal Enrichment during High-Grade Regional Metamorphism. Ii: Pegmatite Staurolite as an Indicator of Anatectic Pegmatite Parent Melt Formation - a Field and Experimental Study. *The Canadian Mineralogist*, *56*(4), 603-624. https://doi.org/10.3749/canmin.1800011

Korzhinskiĭ, D. S. (1959). Physicochemical Basis of the Analysis of the Paragenesis of Minerals. *(No Title)*.

Kowalski, P. M., & Wunder, B. (2018). Boron isotope fractionation among vapor–liquids–solids–melts: experiments and atomistic modeling. *Boron Isotopes: The Fifth Element*, 33-69.

Kowalski, P. M., Wunder, B., & Jahn, S. (2013). Ab initio prediction of equilibrium boron isotope fractionation between minerals and aqueous fluids at high P and T. *Geochimica Et Cosmochimica Acta*, *101*, 285-301.

Kristiansen, R. (2019). Lithium mineralization in Norway: a review. *Norsk Mineralsymposium 2019*, 119-131.

Krmícek, L., Novák, M., Trumbull, R. B., Cempírek, J., & Houzar, S. (2021). Boron isotopic variations in tourmaline from metacarbonates and associated calc-silicate rocks from the Bohemian Massif: Constraints on boron recycling in the Variscan orogen. *Geoscience Frontiers*, *12*(1), 219-230. https://doi.org/10.1016/j.gsf.2020.03.009

Lackey, J. S., Erdmann, S., Hark, J. S., Nowak, R. M., Murray, K. E., Clarke, D. B., & Valley, J. W. (2011). Tracing garnet origins in granitoid rocks by oxygen isotope analysis: examples from the South Mountain Batholith, Nova Scotia. *The Canadian Mineralogist*, *49*(2), 417-439.

Lackey, J. S., Romero, G. A., Bouvier, A.-S., & Valley, J. W. (2012). Dynamic growth of garnet in granitic magmas. *Geology*, *40*(2), 171-174.

Lackey, J. S., Valley, J. W., & Hinke, H. J. (2006). Deciphering the source and contamination history of peraluminous magmas using δ 18 O of accessory minerals: examples from garnet-bearing plutons of the Sierra Nevada batholith. *Contributions to Mineralogy and Petrology*, *151*, 20-44.

Lafuente, B., Downs, R. T., Yang, H., Stone, N., Armbruster, T., & Danisi, R. M. (2015). The power of databases: the RRUFF project. *Highlights in mineralogical crystallography*, *1*, 25.

Lancaster, P. J., Fu, B., Page, F. Z., Kita, N. T., Bickford, M. E., Hill, B. M., McLelland, J. M., & Valley, J. W. (2009). Genesis of metapelitic migmatites in the Adirondack Mountains, New York. *Journal of Metamorphic Geology*, *27*(1), 41-54.

Landais, A., Barkan, E., & Luz, B. (2008). Record of δ18O and 17O-excess in ice from Vostok Antarctica during the last 150,000 years. *Geophysical Research Letters*, *35*(2).

Landais, A., Barkan, E., Yakir, D., & Luz, B. (2006). The triple isotopic composition of oxygen in leaf water. *Geochimica Et Cosmochimica Acta*, *70*(16), 4105-4115.

Larsen, A. O., Nordrum, F. S., & Austrheim, H. (1999). Turmaliner i Norge. *Bergverksmuseets Skrift*, *15*, 21-30.

Larsen, Ø., Skår, Ø., & Pedersen, R.-B. (2002). U-Pb zircon and titanite geochronological constraints on the late/post-Caledonian evolution of the Scandinavian Caledonides in north-central Norway. *Norwegian Journal of Geology/Norsk Geologisk Forening*, *82*(2).

Larson, S. Å., & Berglund, J. (1992). A chronological subdivision of the Transscandinavian Igneous Belt—three magmatic episodes? *Geologiska Föreningen i Stockholm Förhandlingar*, *114*(4), 459-461.

Larson, T., & Sharp, Z. (2005). Interpreting prograde-growth histories of Al2SiO5 triple-point rocks using oxygen-isotope thermometry: an example from the Truchas Mountains, USA. *Journal of Metamorphic Geology*, *23*(9), 847-863.

Leeman, W. P., & Tonarini, S. (2001). Boron isotopic analysis of proposed borosilicate mineral reference samples. *Geostandards Newsletter*, *25*(2-3), 399-403.

Li, Y.-C., Wei, H.-Z., Palmer, M. R., Jiang, S.-Y., Liu, X., Williams-Jones, A. E., Ma, J., Lu, J.-J., Lin, Y.-B., & Dong, G. (2021). Boron coordination and B/Si ordering controls over equilibrium boron isotope fractionation among minerals, melts, and fluids. *Chemical Geology*, *561*, 120030.

Lichtenstein, U., & Hoernes, S. (1992). Oxygen isotope fractionation between grossular-spessartine garnet and water; an experimental investigation. *European Journal of Mineralogy*, *4*(2), 239-249.

Lichtervelde, M. V., Holtz, F., & Melcher, F. (2018). The effect of disequilibrium crystallization on Nb-Ta fractionation in pegmatites: Constraints from crystallization experiments of tantalite-tapiolite. *American Mineralogist*, *103*(9), 1401-1416.

Linnen, R. L., & Cuney, M. (2005). Granite-related rare-element deposits and experimental constraints on Ta-Nb-W-Sn-Zr-Hf mineralization. Linnen, R. Samson, I. *Rare-element geochemistry and mineral deposits.* Geological Association of Canada.

Linnen, R. L., Van Lichtervelde, M., & Cerny, P. (2012). Granitic Pegmatites as Sources of Strategic Metals. *Elements*, *8*(4), 275-280. https://doi.org/10.2113/gselements.8.4.275

Liu, S. Q., Zhang, G. B., Zhang, L. F., Liu, Z. Y., & Xu, J. (2022). Boron isotopes of tourmalines from the central Himalaya: Implications for fluid activity and anatexis in the Himalayan orogen. *Chemical Geology*, *596*. https://doi.org/10.1016/j.chemgeo.022.120800

Lomotey, R. M. (2023). *Origin and Economic Potential of Lithium-mineralized Granitic Pegmatites in Helgeland, North Norway* MSc thesis, UiT Norges arktiske universitet].

London, D. (1996). Granitic pegmatites. *Earth and Environmental Science Transactions of the Royal Society of Edinburgh*, *87*(1-2), 305-319.

London, D. (2005). Granitic pegmatites: an assessment of current concepts and directions for the future. *Lithos*, *80*(1-4), 281-303. https://doi.org/10.1016/j.lithos.2004.02.009

London, D. (2008). *Pegmatites* [Special Publication 10]. The Canadian Mineralogist.

London, D. (2009). The Origin of Primary Textures in Granitic Pegmatites. *Canadian Mineralogist*, *47*(4), 697-724. https://doi.org/10.3749/canmin.47.4.697

London, D. (2014). A petrologic assessment of internal zonation in granitic pegmatites. *Lithos*, *184*, 74-104.

London, D. (2016). Reading pegmatites—Part 2: what tourmaline says. *Rocks & Minerals*, *91*(2), 132-149.

London, D., & Burt, D. M. (1982). Alteration of spodumene, montebrasite and lithiophilite in pegmatites of the White Picacho District, Arizona. *American Mineralogist*, *67*(1-2), 97-113.

London, D., & Kontak, D. J. (2012). Granitic Pegmatites: Scientific Wonders and Economic Bonanzas. *Elements*, *8*(4), 257-261. https://doi.org/10.2113/gselements.8.4.257

London, D., & Morgan, G. B. (2012). The pegmatite puzzle. *Elements*, *8*(4), 263-268.

London, D., Morgan, G. B., Wolf, M. B., Grew, E., & Anovitz, L. (1996). Boron in granitic rocks and their contact aureoles. *Reviews in Mineralogy*, *33*, 299-330.

London, D., VI, G. B. M., & Acosta-Vigil, A. (2012). Experimental simulations of anatexis and assimilation involving metapelite and granitic melt. *Lithos*, *153*, 292-307.

London, D., Wolf, M. B., Morgan, G. B., & Garrido, M. G. (1999). Experimental silicate–phosphate equilibria in peraluminous granitic magmas, with a case study of the Alburquerque batholith at Tres Arroyos, Badajoz, Spain. *Journal of Petrology*, *40*(1), 215-240.

Luz, B., & Barkan, E. (2005). The isotopic ratios 17O/16O and 18O/16O in molecular oxygen and their significance in biogeochemistry. *Geochimica Et Cosmochimica Acta*, *69*(5), 1099-1110.

Luz, B., & Barkan, E. (2010). Variations of 17O/16O and 18O/16O in meteoric waters. *Geochimica Et Cosmochimica Acta*, *74*(22), 6276-6286.

Løseth, H., & Thorsnes, T. (1991). Tectonostratigraphy in the Velfjord-Tosen region, southwestern part of the Helgeland Nappe Complex, Central Norwegian Caledonides.

Maner, J. L., & London, D. (2017). The boron isotopic evolution of the Little Three pegmatites, Ramona, CA. *Chemical Geology*, *460*, 70-83. https://doi.org/10.1016/j.chemgeo.2017.04.016

Manning, D. (1982). Chemical and morphological variation in tourmalines from the Hub Kapong batholith of peninsular Thailand. *Mineralogical Magazine*, *45*(337), 139-147.

Marks, M. A., Marschall, H. R., Schühle, P., Guth, A., Wenzel, T., Jacob, D. E., Barth, M., & Markl, G. (2013). Trace element systematics of tourmaline in pegmatitic and hydrothermal systems from the Variscan Schwarzwald (Germany): The importance of major element composition, sector zoning, and fluid or melt composition. *Chemical Geology*, *344*, 73-90.

Marschall, H. R., & Foster, G. L. (2018). Boron isotopes in the earth and planetary sciences—a short history and introduction. *Boron Isotopes: The Fifth Element*, 1-11.

Marschall, H. R., & Jiang, S.-Y. (2011). Tourmaline isotopes: no element left behind. *Elements*, *7*(5), 313-319.

Martin, E., & Bindeman, I. (2009). Mass-independent isotopic signatures of volcanic sulfate from three supereruption ash deposits in Lake Tecopa, California. *Earth and Planetary Science Letters*, *282*(1-4), 102-114.

Martin, R. F., & De Vito, C. (2005). The patterns of enrichment in felsic pegmatites ultimately depend on tectonic setting. *Canadian Mineralogist*, *43*(6), 2027.

Matsuhisa, Y., Goldsmith, J. R., & Clayton, R. N. (1978). Mechanisms of Hydrothermal Crystallization of Quartz at 250-Degrees-C and 15 Kbar. *Geochimica Et Cosmochimica Acta*, *42*(2), 173-&. https://doi.org/Doi 10.1016/0016-7037(78)90130-8

McCaffrey, D. M., & Jowitt, S. M. (2023). The crystallization temperature of granitic pegmatites: The important relationship between undercooling and critical metal prospectivity. *Earth-Science Reviews*, *244*, 104541.

McKinney, C. R., McCrea, J. M., Epstein, S., Allen, H., & Urey, H. C. (1950). Improvements in mass spectrometers for the measurement of small differences in isotope abundance ratios. *Review of Scientific Instruments*, *21*(8), 724-730.

Melleton, J., Gloaguen, E., Frei, D., Novák, M., & Breiter, K. (2012). How Are the Emplacement of Rare-Element Pegmatites, Regional Metamorphism and Magmatism Interrelated in the Moldanubian Domain of the Variscan Bohemian Massif, Czech Republic? *Canadian Mineralogist*, *50*(6), 1751-1773. https://doi.org/10.3749/canmin.50.6.1751

Melo, M. G. d., Stevens, G., Lana, C., Pedrosa-Soares, A., Frei, D., Alkmim, F. F. d., & Alkmin, L. (2017). Two cryptic anatectic events within a syn-collisional granitoid from the Araçuaí orogen (southeastern Brazil): evidence from the polymetamorphic Carlos Chagas batholith. *Lithos*, *277*, 51-71.

Meyer, C., Wunder, B., Meixner, A., Romer, R. L., & Heinrich, W. (2008). Boron-isotope fractionation between tourmaline and fluid: an experimental re-investigation. *Contributions to Mineralogy and Petrology*, *156*, 259-267.

Miller, M., Franchi, I., Sexton, A., & Pillinger, C. (1999). High precision δ17O isotope measurements of oxygen from silicates and other oxides: method and applications. *Rapid Communications in Mass Spectrometry*, *13*(13), 1211-1217.

Miller, M. F. (2002). Isotopic fractionation and the quantification of 17O anomalies in the oxygen three-isotope system: an appraisal and geochemical significance. *Geochimica Et Cosmochimica Acta*, *66*(11), 1881-1889.

Miller, M. F., & Pack, A. (2021). Why measure 17O? Historical perspective, triple-isotope systematics and selected applications. *Reviews in Mineralogy and Geochemistry*, *86*(1), 1-34.

Mitchell, N. J. (2017). *The Composition of Garnet in Granitic Pegmatites as a Proxy for Melt Evolution and Rare Metal Potential* East Carolina University].

Moecher, D. P., & Sharp, Z. D. (1999). Comparison of conventional and garnet-aluminosilicate-quartz O isotope thermometry: Insights for mineral equilibration in metamorphic rocks. *American Mineralogist*, *84*(9), 1287-1303.

Momma, K., & Izumi, F. (2011). VESTA 3 for three-dimensional visualization of crystal, volumetric and morphology data. *Journal of applied crystallography*, *44*(6), 1272-1276.

Moretz, L., Heimann, A., Bitner, J., Wise, M., Rodrigues Soares, D., & Mousinho Ferreira, A. (2013). The composition of garnet as indicator of rare metal (Li) mineralization in granitic pegmatites. International Symposium on Granitic Pegmatites,

Morgan, G. B., & London, D. (1989). Experimental reactions of amphibolite with boron-bearing aqueous fluids at 200 MPa: implications for tourmaline stability and partial melting in mafic rocks. *Contributions to Mineralogy and Petrology*, *102*, 281-297.

Muehlenbachs, K. (1998). The oxygen isotopic composition of the oceans, sediments and the seafloor. *Chemical Geology*, *145*(3-4), 263-273.

Müller, A. (2010). *Potentials of rare earth element and Zr-, Be-, U-, Th-,(W-) mineralisations in central and northern Nordland* (2010.037). https://hdl.handle.net/11250/2664651

Müller, A., Kearsley, A., Spratt, J., & Seltmann, R. (2012). Petrogenetic implications of magmatic garnet in granitic pegmatites from southern Norway. *The Canadian Mineralogist*, *50*(4), 1095-1115.

Müller, A., Romer, R. L., Augland, L. E., Zhou, H. Y., Rosing-Schow, N., Spratt, J., & Husdal, T. (2022). Two-stage regional rare-element pegmatite formation at Tysfjord, Norway: implications for the timing of late Svecofennian and late Caledonian high-temperature events. *International Journal of Earth Sciences*, *111*(3), 987-1007. https://doi.org/10.1007/s00531-022-02166-5

Müller, A., Romer, R. L., & Pedersen, R. B. (2017). The Sveconorwegian Pegmatite Province - Thousands of Pegmatites without Parental Granites. *Canadian Mineralogist*, *55*(2), 283-315. https://doi.org/10.3749/canmin.1600075

Müller, A., Spratt, J., Thomas, R., Williamson, B. J., & Seltmann, R. (2018). Alkali-F-rich albite zones in evolved NYF pegmatites: the product of melt–melt immiscibility. *The Canadian Mineralogist*, *56*(4), 657-687.

Nabelek, P. I., Whittington, A. G., & Sirbescu, M. L. C. (2010). The role of HO in rapid emplacement and crystallization of granite pegmatites: resolving the paradox of large crystals in highly undercooled melts. *Contributions to Mineralogy and Petrology*, *160*(3), 313-325. https://doi.org/10.1007/s00410-009-0479-1

Nesse, W. (2014). *Introduction to optical mineralogy* (4 ed.). Oxford University Press.

Northrup, C. (1997). Timing Structural Assembly, Metamorphism, and Cooling of Caledonian Nappes in the Ofoten-Efjorden Arca, North Norway: Tectonic Insights From U-Pb and 40Ar/39Ar Geochronology. *The Journal of Geology*, *105*(5), 565-582.

Novak, G. A., & Gibbs, G. (1971). The crystal chemistry of the silicate garnets. *American Mineralogist: Journal of Earth and Planetary Materials*, *56*(5-6), 791-825.

Novák, M., & Povondra, P. (1995). Elbaite pegmatites in the Moldanubicum: a new subtype of the rare-element class. *Mineralogy and Petrology*, *55*(1), 159-176.

Novák, M., Škoda, R., Gadas, P., Krmíček, L., & Černý, P. (2012). Contrasting origins of the mixed (NYF+ LCT) signature in granitic pegmatites, with examples from the Moldanubian Zone, Czech Republic. *The Canadian Mineralogist*, *50*(4), 1077-1094.

Oftedal, I. (1950). En litiumførende granittpegmatitt i Nordland. *Norsk Geologisk Tidsskrift*, *28*, 234-237.

Okrusch, M., & Matthes, S. (2014). *Eine Einführung in die spezielle Mineralogie, Petrologie und Lagerstättenkunde*. Springer.

Pack, A. (2021). Isotopic traces of atmospheric O2 in rocks, minerals, and melts. *Reviews in Mineralogy and Geochemistry*, *86*(1), 217-240.

Pack, A., & Herwartz, D. (2014). The triple oxygen isotope composition of the Earth mantle and understanding ΔO17 variations in terrestrial rocks and minerals. *Earth and Planetary Science Letters*, *390*, 138-145.

Pack, A., Tanaka, R., Hering, M., Sengupta, S., Peters, S., & Nakamura, E. (2016). The oxygen isotope composition of San Carlos olivine on the VSMOW2-SLAP2 scale. *Rapid Communications in Mass Spectrometry*, *30*(13), 1495-1504.

Palme, H., & Jones, A. (2003). Solar system abundances of the elements. *Treatise on geochemistry*, *1*, 711.

Palmer, M., London, D., VI, G. M., & Babb, H. (1992). Experimental determination of fractionation of11B/10B between tourmaline and aqueous vapor: A temperature-and pressure-dependent isotopic system. *Chemical Geology: Isotope Geoscience Section*, *101*(1-2), 123-129.

Palmer, M. R., & Swihart, G. H. (1996). Boron isotope geochemistry: an overview. *Reviews in Mineralogy*, *33*(1), 709-744.

Patchett, P. J., Todt, W., & Gorbatschev, R. (1987). Origin of continental crust of 1.9-1.7 Ga age: Nd isotopes in the Svecofennian orogenic terrains of Sweden. *Precambrian Research*, *35*, 145-160.

Petit, J.-R., Jouzel, J., Raynaud, D., Barkov, N. I., Barnola, J.-M., Basile, I., Bender, M., Chappellaz, J., Davis, M., & Delaygue, G. (1999). Climate and atmospheric history of the past 420,000 years from the Vostok ice core, Antarctica. *Nature*, *399*(6735), 429-436.

Pezzotta, F., & Laurs, B. M. (2011). Tourmaline: The kaleidoscopic gemstone. *Elements*, *7*(5), 333-338.

Piilonen, P., McDonald, A., Poirier, G., Rowe, R., & Larsen, A. (2012). The mineralogy and crystal chemistry of alkaline pegmatites in the Larvik Plutonic Complex, Oslo rift valley, Norway. Part 1. Magmatic and secondary zircon: implications for petrogenesis from trace-element geochemistry. *Mineralogical Magazine*, *76*(3), 649-672.

Prol-Ledesma, R.-M., Melgarejo, J. C., & Martin, R. F. (2012). The El Muerto “NYF” granitic pegmatite, Oaxaca, Mexico, and its striking enrichment in allanite-(Ce) and monazite-(Ce). *The Canadian Mineralogist*, *50*(4), 1055-1076.

Quinn, R., Kitajima, K., Nakashima, D., Spicuzza, M., & Valley, J. (2017). Oxygen isotope thermometry using quartz inclusions in garnet. *Journal of Metamorphic Geology*, *35*(2), 231-252.

Quintero, R. R., Kitajima, K., Star Lackey, J., Kozdon, R., Strickland, A., & Valley, J. W. (2021). Oxygen isotope ratios in zircon and garnet: A record of assimilation and fractional crystallization in the Dinkey Dome peraluminous granite, Sierra Nevada, California. *American Mineralogist*, *106*(5), 715-729.

Reid, K. (2004). *Magmatic processes in the Tosenfjord region, north-central Norway: implications for the evolution of the Helgeland Nappe complex* [MSc thesis, Texas Tech University].

Rieder, M., Cavazzini, G., D'yakonov, Y. S., Frank-Kamenetskii, V. A., Gottardi, G., Guggenheim, S., Koval, P. W., Müller, G., Neiva, A. M., & Radoslovich, E. W. (1998). Nomenclature of the micas. *Clays and clay minerals*, *46*(5), 586-595.

Roberts, D., & Gee, D. G. (1985). An introduction to the structure of the Scandinavian Caledonides. *The Caledonide orogen–Scandinavia and related areas*, *1*, 55-68.

Romer, R., Kjøsnes, B., Korneliussen, A., Lindahl, I., Skyseth, T., Stendal, M., & Sundvoll, B. (1992). The Archaean–Proterozoic boundary beneath the Caledonides of northern Norway and Sweden: U–Pb, Rb–Sr and Nd isotopic data from the Rombak–Tysfjord area. *Geological Survey of Norway, Report*, *91*.

Romer, R. L., & Kroner, U. (2016). Phanerozoic tin and tungsten mineralization-Tectonic controls on the distribution of enriched protoliths and heat sources for crustal melting. *Gondwana Research*, *31*, 60-95. https://doi.org/10.1016/j.gr.2015.11.002

Romer, R. L., & Pichavant, M. (2021). Rare metal granites and pegmatites. In *Encyclopedia of Geology* (2 ed., pp. 840-846). Elsevier. https://doi.org/https://doi.org/10.1016/B978-0-08-102908-4.00003-5

Rosenbaum, J. M., & Mattey, D. (1995). Equilibrium garnet-calcite oxygen isotope fractionation. *Geochimica Et Cosmochimica Acta*, *59*(13), 2839-2842.

Rosman, K., & Taylor, P. (1998). Isotopic compositions of the elements 1997. *Journal of Physical and Chemical Reference Data*, *27*(6), 1275-1287.

Rumble, D., Miller, M. F., Franchi, I., & Greenwood, R. (2007). Oxygen three-isotope fractionation lines in terrestrial silicate minerals: An inter-laboratory comparison of hydrothermal quartz and eclogitic garnet. *Geochimica Et Cosmochimica Acta*, *71*(14), 3592-3600.

Rutland, R., Holmes, M., & Jones, M. (1960). Granites of the Glomfjord area, northern Norway. Int. Geol. Congress,

Raade, G. (2020). Helvine-group minerals from Norwegian granitic pegmatites and some other granitic rocks: Cases of significant Sc and Sn contents. *The Canadian Mineralogist*, *58*(3), 367-379.

Samadi, R., Miller, N. R., Mirnejad, H., Harris, C., Kawabata, H., & Shirdashtzadeh, N. (2014). Origin of garnet in aplite and pegmatite from Khajeh Morad in northeastern Iran: A major, trace element, and oxygen isotope approach. *Lithos*, *208*, 378-392.

Savarino, J., Romero, A., Cole-Dai, J., Bekki, S., & Thiemens, M. (2003). UV induced mass-independent sulfur isotope fractionation in stratospheric volcanic sulfate. *Geophysical Research Letters*, *30*(21).

Schmidt, C., Thomas, R., & Heinrich, W. (2005). Boron speciation in aqueous fluids at 22 to 600 C and 0.1 MPa to 2 GPa. *Geochimica Et Cosmochimica Acta*, *69*(2), 275-281.

Schweizer, P., Brackx, E., & Jonnard, P. (2022). Electron probe microanalysis of light elements: Improvements in the measurement and signal extraction methods. *X-Ray Spectrometry*, *51*(4), 403-412.

Selway, J. B. (1999). *Compositional evolution of tourmaline in granitic pegmatites* [Doctoral Dissertation, University of Manitoba].

Selway, J. B., Novák, M., Cerny, P., & Hawthorne, F. C. (1999). Compositional evolution of tourmaline in lepidolite-subtype pegmatites. *European Journal of Mineralogy-Ohne Beihefte*, *11*(3), 569-584.

Sharp, Z., Gibbons, J., Maltsev, O., Atudorei, V., Pack, A., Sengupta, S., Shock, E., & Knauth, L. (2016). A calibration of the triple oxygen isotope fractionation in the SiO2–H2O system and applications to natural samples. *Geochimica Et Cosmochimica Acta*, *186*, 105-119.

Sharp, Z., Wostbrock, J., & Pack, A. (2018). Mass-dependent triple oxygen isotope variations in terrestrial materials. *Geochem. Perspect. Lett*, *7*, 27-31.

Shaw, R. A., Goodenough, K. M., Deady, E., Nex, P., Ruzvidzo, B., Rushton, J. C., & Mounteney, I. (2022). The magmatic-hydrothermal transition in lithium pegmatites: Petrographic and geochemical characteristics of pegmatites from the Kamativi area, Zimbabwe. *Canadian Mineralogist*, *60*, 957-987.

Shigley, J. E., Cook, B. C., Laurs, B. M., & Bernardes, M. (2001). An update on “Paraíba” tourmaline from Brazil. *Gems & Gemology*, *37*(4), 260-276.

Shtukenberg, A., Rozhdestvenskaya, I., Frank-Kamenetskaya, O., Bronzova, J., Euler, H., Kirfel, A., Bannova, I., & Zolotarev, A. (2007). Symmetry and crystal structure of biaxial elbaite-liddicoatite tourmaline from the Transbaikalia region, Russia. *American Mineralogist*, *92*(4), 675-686.

Siegel, K., Wagner, T., Trumbull, R. B., Jonsson, E., Matalin, G., Wälle, M., & Heinrich, C. A. (2016). Stable isotope (B, H, O) and mineral-chemistry constraints on the magmatic to hydrothermal evolution of the Varutrask rare-element pegmatite (Northern Sweden). *Chemical Geology*, *421*, 1-16. https://doi.org/10.1016/j.chemgeo.2015.11.025

Simmons, W. B. S., & Webber, K. L. (2008). Pegmatite genesis: state of the art. *European Journal of Mineralogy*, *20*(4), 421.

Sirbescu, M.-L. C., Schmidt, C., Veksler, I. V., Whittington, A. G., & Wilke, M. (2017). Experimental crystallization of undercooled felsic liquids: generation of pegmatitic texture. *Journal of Petrology*, *58*(3), 539-568.

Skjerlie, K. P., & Johnston, A. D. (1992). Vapor-absent melting at 10 kbar of a biotite-and amphibole-bearing tonalitic gneiss: implications for the generation of A-type granites. *Geology*, *20*(3), 263-266.

Skår, Ø. (2002). U–Pb geochronology and geochemistry of early Proterozoic rocks of the tectonic basement windows in central Nordland, Caledonides of north-central Norway. *Precambrian Research*, *116*(3-4), 265-283.

Soares, D. R., Beurlen, H., Barreto, S. d. B., Da Silva, M. R. R., & Ferreira, A. C. M. (2008). Compositional variation of tourmaline-group minerals in the Borborema Pegmatite Province, northeastern Brazil. *The Canadian Mineralogist*, *46*(5), 1097-1116.

Spjeldnæs, N. (1985). Biostratigraphy of the Scandinavian Caledonides. In (pp. 317-329): John Wiley and Sons Chichester.

Stephens, M., Gustavson, M., Ramberg, I., & Zachrisson, E. (1985). The Caledonides of central-north Scandinavia-a tectonostratigraphic overview. *The Caledonide orogen–Scandinavia and related areas*, 135-162.

Stephens, M. B., & Gee, D. G. (1985). A tectonic model for the evolution of the eugeoclinal terranes in the central Scandinavian Caledonides. *The Caledonide Orogen: Scandinavia and related Areas*, 953-978.

Stevens, G., Villaros, A., & Moyen, J.-F. (2007). Selective peritectic garnet entrainment as the origin of geochemical diversity in S-type granites. *Geology*, *35*(1), 9-12.

Sun, T., & Bao, H. (2011). Non-mass-dependent 17O anomalies generated by a superimposed thermal gradient on a rarefied O2 gas in a closed system. *Rapid Communications in Mass Spectrometry*, *25*(1), 20-24.

Thiemens, M. H., & Heidenreich, J. E. (1983). The mass-independent fractionation of oxygen: A novel isotope effect and its possible cosmochemical implications. *Science*, *219*(4588), 1073-1075.

Thomas, R., & Davidson, P. (2012). Water in granite and pegmatite-forming melts. *Ore Geology Reviews*, *46*, 32-46. https://doi.org/10.1016/j.oregeorev.2012.02.006

Thomas, R., & Davidson, P. (2016). Revisiting complete miscibility between silicate melts and hydrous fluids, and the extreme enrichment of some elements in the supercritical state—Consequences for the formation of pegmatites and ore deposits. *Ore Geology Reviews*, *72*, 1088-1101.

Thomas, R., Davidson, P., & Beurlen, H. (2012). The competing models for the origin and internal evolution of granitic pegmatites in the light of melt and fluid inclusion research. *Mineralogy and Petrology*, *106*(1-2), 55-73. https://doi.org/10.1007/s00710-012-0212-z

Thomas, R., & Veksler, I. (2002). Formation of granite pegmatites in the light of melt and fluid inclusion studies and new and old experimental work. *Mineralogical Society of Poland Special Papers*, *20*, 44-49.

Thomas, R., Webster, J., & Heinrich, W. (2000). Melt inclusions in pegmatite quartz: complete miscibility between silicate melts and hydrous fluids at low pressure. *Contributions to Mineralogy and Petrology*, *139*, 394-401.

Thomas, R., Webster, J., Rhede, D., Seifert, W., Rickers, K., Förster, H.-J., Heinrich, W., & Davidson, P. (2006). The transition from peraluminous to peralkaline granitic melts: evidence from melt inclusions and accessory minerals. *Lithos*, *91*(1-4), 137-149.

Tippe, A., & Hamilton, W. C. (1971). A neutron-diffraction study of the ferric tourmaline, buergerite. *American Mineralogist: Journal of Earth and Planetary Materials*, *56*(1-2), 101-113.

Tischendorf, G., Förster, H.-J., & Gottesmann, B. (2001). Minor-and trace-element composition of trioctahedral micas: a review. *Mineralogical Magazine*, *65*(2), 249-276.

Tischendorf, G., Gottesmann, B., Förster, H.-J., & Trumbull, R. B. (1997). On Li-bearing micas: estimating Li from electron microprobe analyses and an improved diagram for graphical representation. *Mineralogical Magazine*, *61*(409), 809-834.

Tonarini, S., Forte, C., Petrini, R., & Ferrara, G. (2003). Melt/biotite 11B/10B isotopic fractionation and the boron local environment in the structure of volcanic glasses. *Geochimica Et Cosmochimica Acta*, *67*(10), 1863-1873.

Trumbull, R. B., Beurlen, H., Wiedenbeck, M., & Soares, D. R. (2013). The diversity of B-isotope variations in tourmaline from rare-element pegmatites in the Borborema Province of Brazil. *Chemical Geology*, *352*, 47-62. https://doi.org/10.1016/j.chemgeo.2013.05.021

Trumbull, R. B., Codeço, M. S., Jiang, S.-Y., Palmer, M. R., & Slack, J. F. (2020). Boron isotope variations in tourmaline from hydrothermal ore deposits: a review of controlling factors and insights for mineralizing systems. *Ore Geology Reviews*, *125*, 103682.

Trumbull, R. B., Krienitz, M.-S., Gottesmann, B., & Wiedenbeck, M. (2008). Chemical and boron-isotope variations in tourmalines from an S-type granite and its source rocks: the Erongo granite and tourmalinites in the Damara Belt, Namibia. *Contributions to Mineralogy and Petrology*, *155*, 1-18.

Trumbull, R. B., & Slack, J. F. (2018). Boron isotopes in the continental crust: granites, pegmatites, felsic volcanic rocks, and related ore deposits. *Boron Isotopes: The Fifth Element*, 249-272.

Valley, J. W. (2001). Stable isotope thermometry at high temperatures. *Reviews in Mineralogy and Geochemistry*, *43*(1), 365-413.

Valley, J. W., Bindeman, I. N., & Peck, W. H. (2003). Empirical calibration of oxygen isotope fractionation in zircon. *Geochimica Et Cosmochimica Acta*, *67*(17), 3257-3266.

van der Does, L. M., Hulsbosch, N., Kaskes, P., Elsen, J., Claeys, P., Muchez, P., & Sirbescu, M.-L. C. (2024). Tourmaline growth in the border and wall zones of the Emmons pegmatite (Maine, USA): Evidence for disequilibrium crystallization and boundary layer formation. *American Mineralogist*, *109*(4), 785-798.

van Hinsberg, V. J., Henry, D. J., & Dutrow, B. L. (2011). Tourmaline as a petrologic forensic mineral: A unique recorder of its geologic past. *Elements*, *7*(5), 327-332.

Veksler, I. V. (2004). Liquid immiscibility and its role at the magmatic-hydrothermal transition: a summary of experimental studies. *Chemical Geology*, *210*(1-4), 7-31. https://doi.org/10.1016/j.chemgeo.2004.06.002

Veksler, I. V., Dorfman, A. M., Dingwell, D. B., & Zotov, N. (2002). Element partitioning between immiscible borosilicate liquids: a high-temperature centrifuge study. *Geochimica Et Cosmochimica Acta*, *66*(14), 2603-2614.

Veksler, I. V., Dorfman, A. M., Dulski, P., Kamenetsky, V. S., Danyushevsky, L. V., Jeffries, T., & Dingwell, D. B. (2012). Partitioning of elements between silicate melt and immiscible fluoride, chloride, carbonate, phosphate and sulfate melts, with implications to the origin of natrocarbonatite. *Geochimica Et Cosmochimica Acta*, *79*, 20-40.

Veksler, I. V., & Thomas, R. (2002). An experimental study of B-, P- and F-rich synthetic granite pegmatite at 0.1 and 0.2 GPa. *Contributions to Mineralogy and Petrology*, *143*(6), 673-683. https://doi.org/10.1007/s00410-002-0368-3

Villaros, A., Stevens, G., & Buick, I. S. (2009). Tracking S-type granite from source to emplacement: clues from garnet in the Cape Granite Suite. *Lithos*, *112*(3-4), 217-235.

Warr, L. N. (2021). IMA–CNMNC approved mineral symbols. *Mineralogical Magazine*, *85*(3), 291-320.

Wen, J., & Thiemens, M. H. (1990). An apparent new isotope effect in a molecular decomposition and implications for nature. *Chemical physics letters*, *172*(5), 416-420.

Wen, J., & Thiemens, M. H. (1991). Experimental and theoretical study of isotope effects on ozone decomposition. *Journal of Geophysical Research: Atmospheres*, *96*(D6), 10911-10921.

Wiedenbeck, M., Trumbull, R. B., Rosner, M., Boyce, A., Fournelle, J. H., Franchi, I. A., Halama, R., Harris, C., Lacey, J. H., & Marschall, H. (2021). Tourmaline reference materials for the in situ analysis of oxygen and lithium isotope ratio compositions. *Geostandards and Geoanalytical Research*, *45*(1), 97-119.

Wilson, M. R., & Nicholson, R. (1973). The structural setting and geochronology of basal granitic gneisses in the Caledonides of part of Nordland, Norway. *Journal of the Geological Society*, *129*(4), 365-386.

Wise, M. A., Müller, A., & Simmons, W. B. (2022). A proposed new mineralogical classification system for granitic pegmatites. *The Canadian Mineralogist*, *60*(2), 229-248.

Wolf, M., Romer, R. L., Franz, L., & López-Moro, F. J. (2018). Tin in granitic melts: The role of melting temperature and protolith composition. *Lithos*, *310*, 20-30.

Wunder, B., Meixner, A., Romer, R. L., Wirth, R., & Heinrich, W. (2005). The geochemical cycle of boron: constraints from boron isotope partitioning experiments between mica and fluid. *Lithos*, *84*(3-4), 206-216.

Yakir, D., & Sternberg, L. d. S. (2000). The use of stable isotopes to study ecosystem gas exchange. *Oecologia*, *123*, 297-311.

Yang, S.-Y., Jiang, S.-Y., & Palmer, M. R. (2015). Chemical and boron isotopic compositions of tourmaline from the Nyalam leucogranites, South Tibetan Himalaya: Implication for their formation from B-rich melt to hydrothermal fluids. *Chemical Geology*, *419*, 102-113.

Yoshinobu, A., Reid, K., Barnes, C., & Allen, C. (2005). Crustal melting in the Helgeland Nappe Complex, central Norway. AGU Fall Meeting Abstracts,

Yoshinobu, A. S., Barnes, C. G., Nordgulen, Ø., Prestvik, T., Fanning, M., & Pedersen, R. (2002). Ordovician magmatism, deformation, and exhumation in the Caledonides of central Norway: An orphan of the Taconic orogeny? *Geology*, *30*(10), 883-886.

Young, E. D., Galy, A., & Nagahara, H. (2002). Kinetic and equilibrium mass-dependent isotope fractionation laws in nature and their geochemical and cosmochemical significance. *Geochimica Et Cosmochimica Acta*, *66*(6), 1095-1104.

Yu, M., Xia, Q.-X., Zheng, Y.-F., Zhao, Z.-F., Chen, Y.-X., Chen, R.-X., Luo, X., Li, W.-C., & Xu, H. (2021). The composition of garnet in granite and pegmatite from the Gangdese orogen in southeastern Tibet: Constraints on pegmatite petrogenesis. *American Mineralogist*, *106*(2), 265-281.

Zhang, C., Giere, R., Stünitz, H., Brack, P., & Ulmer, P. (2001). Garnet-quartz intergrowths in granitic pegmatites from Bergell and Adamello, Italy. *SCHWEIZ. MINERAL. PETROGR. MITT.*(81), 89-113.

Zheng, Y.-F. (1993). Calculation of oxygen isotope fractionation in anhydrous silicate minerals. *Geochimica Et Cosmochimica Acta*, *57*(5), 1079-1091.

Zhou, Q., Li, W., Wang, G., Liu, Z., Lai, Y., Huang, J., Yan, G., & Zhang, Q. (2019). Chemical and boron isotopic composition of tourmaline from the Conadong leucogranite-pegmatite system in South Tibet. *Lithos*, *326*, 529-539.

Åhäll, K.-I., & Connelly, J. N. (2008). Long-term convergence along SW Fennoscandia: 330 my of Proterozoic crustal growth. *Precambrian Research*, *161*(3-4), 452-474.

Åhäll, K.-I., & Larson, S. Å. (2000). Growth-related 1.85–1.55 Ga magmatism in the Baltic Shield; a review addressing the tectonic characteristics of Svecofennian, TIB 1-related, and Gothian events. *GFF*, *122*(2), 193-206.

Appendix A
Complementary figures

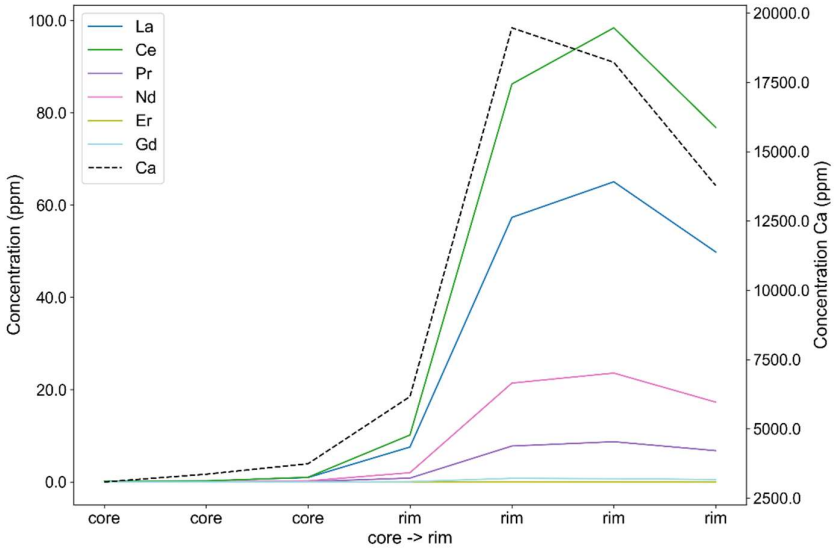

***Figure A1**. Profile through the outer core and rim of the tourmaline crystal 111 from Ågskardet OQ5. The left scale indicates concentrations of selected REE and the right scale shows the concentration of Ca (ppm).*

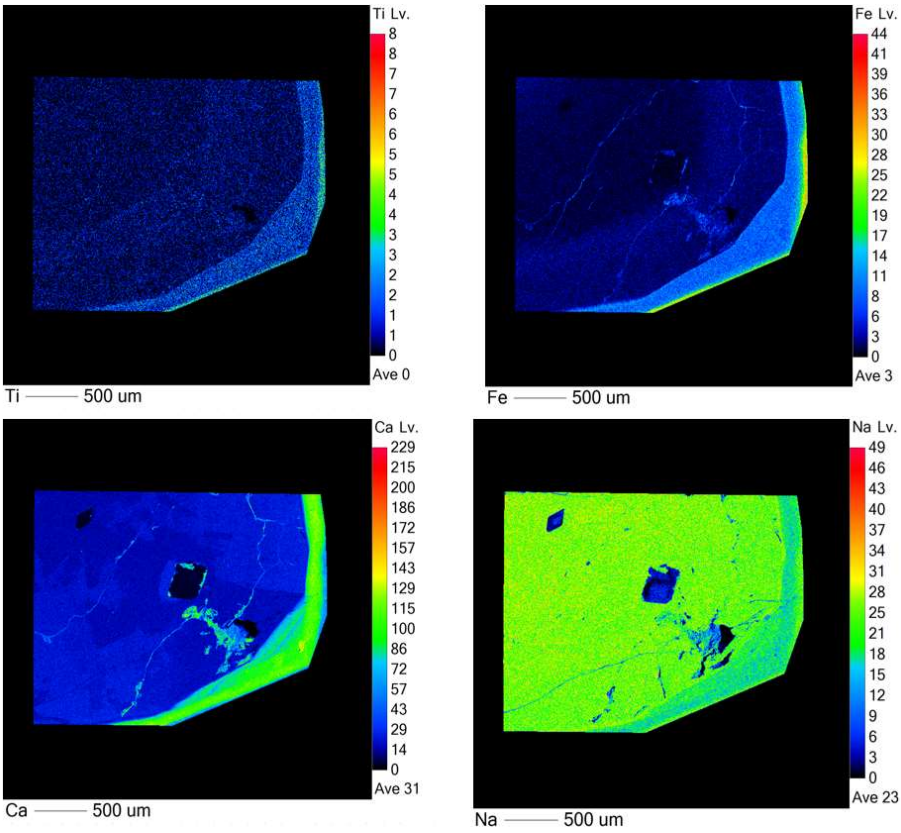

***Figure A2.** Element maps showing increase of Ti, Fe, Ca and Na in the rim of tourmaline crystal 111 from Ågskardet OQ5.*

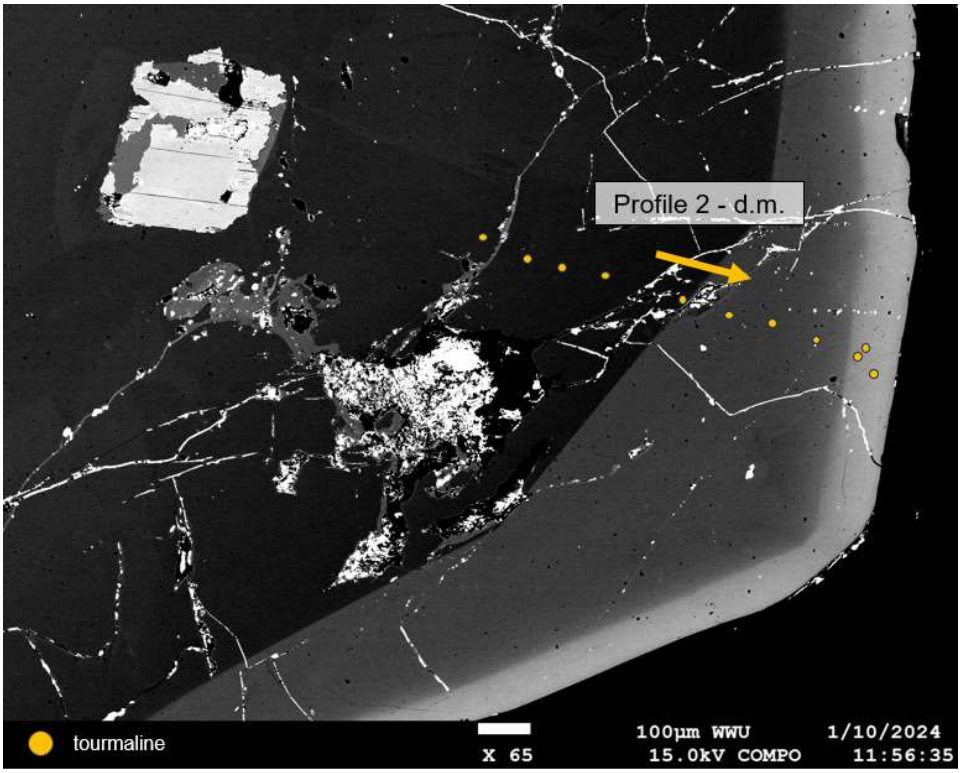

Figure A3. *EPMA profile 2 detailed margin in tourmaline crystal 111 from Ågskardet OQ5.*

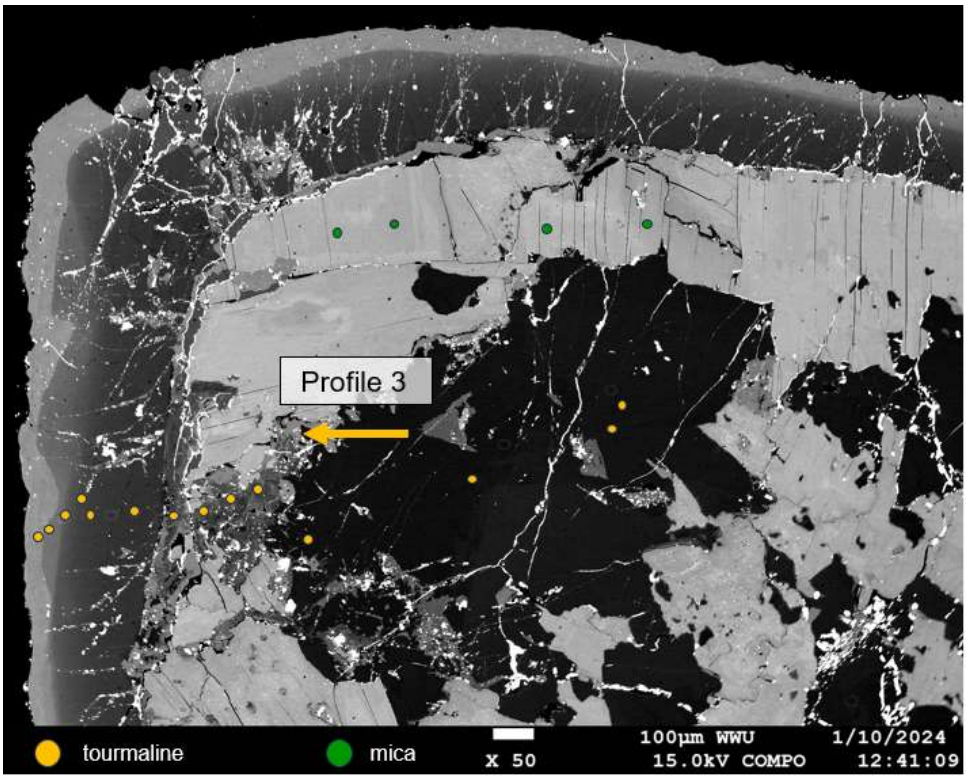

Figure A4. *EPMA profile 3 in tourmaline (yellow) and analysis spots in mica (green) in crystal 112 from Ågskardet OQ6.*

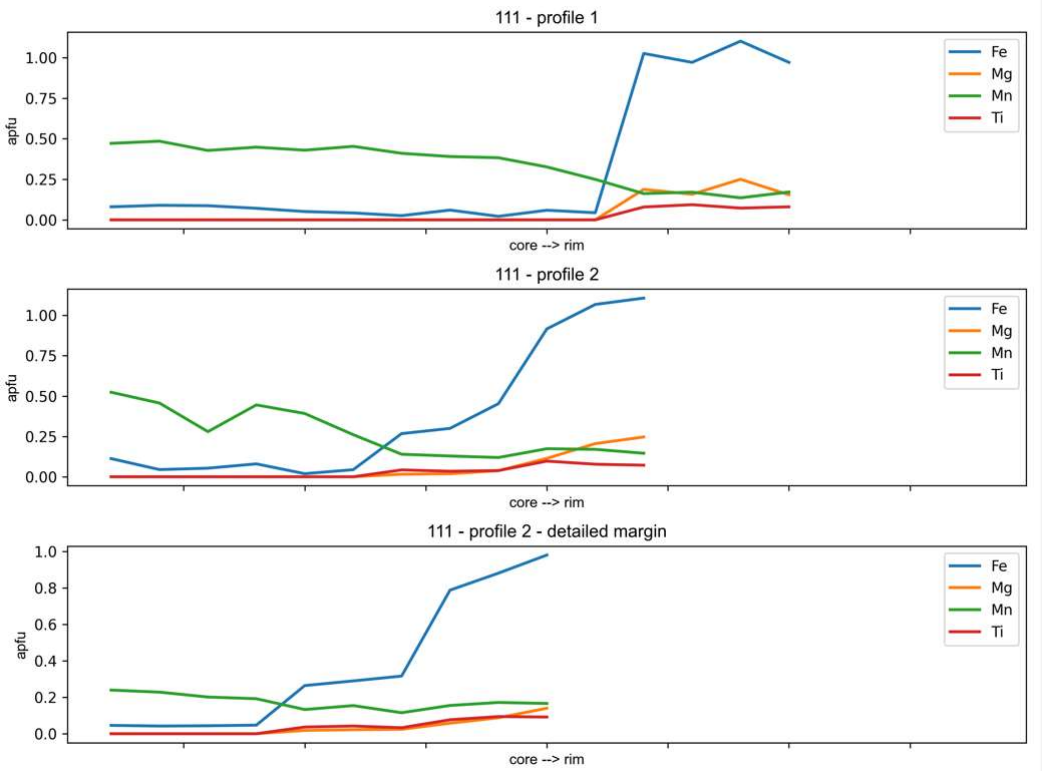

Figure A5. *Major element profiles from core to rim on tourmaline crystal 111 from Ågskardet OQ5.*

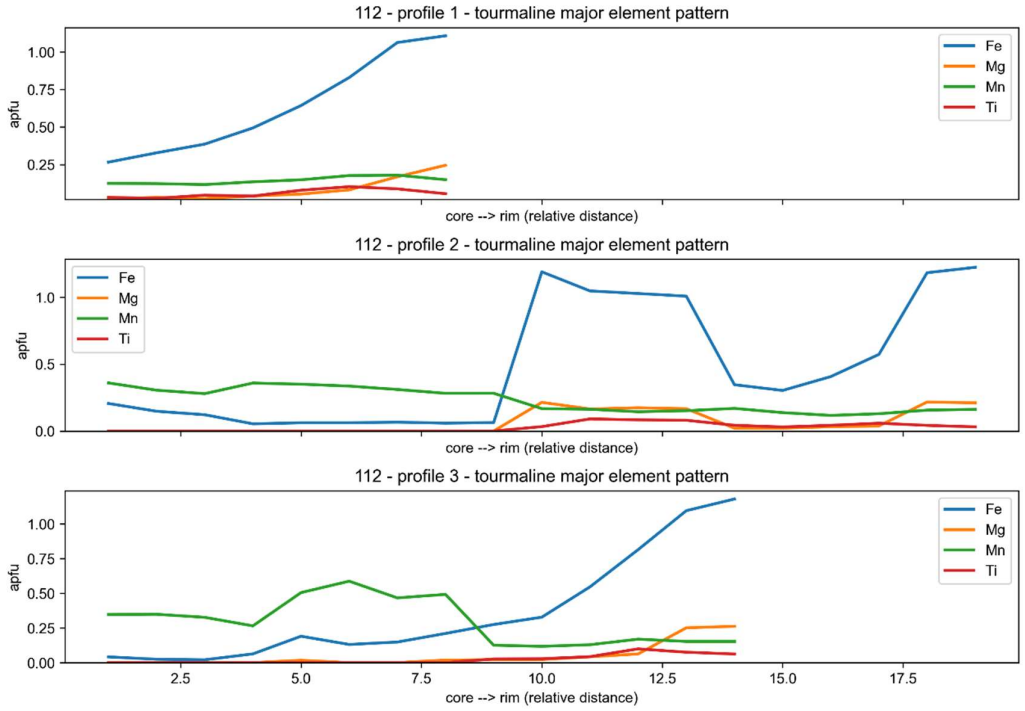

Figure A6. *Major element profiles from core to rim on tourmaline crystal 112 from Ågskardet OQ6.*

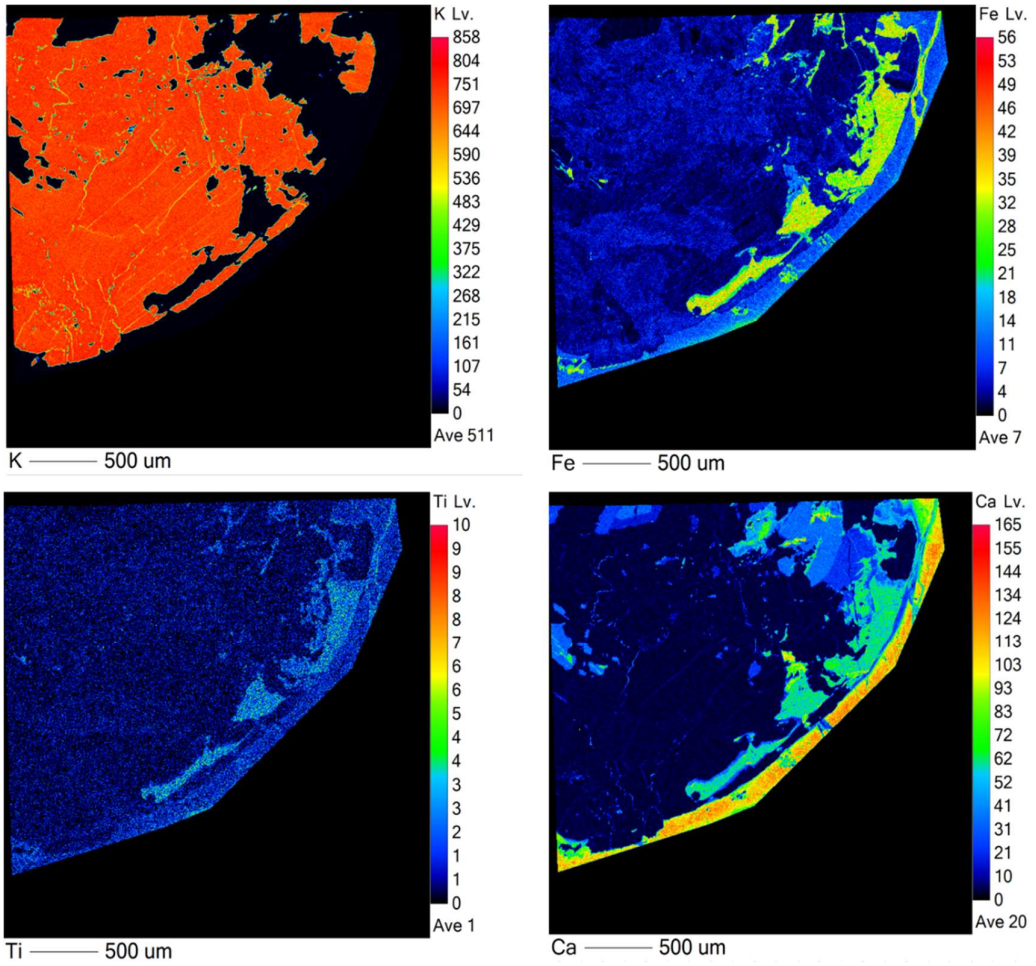

Figure A7. *Element map of tourmaline crystal 112 with abundant mica inclusions from Ågskardet OQ6. It shows the difference between mica (rich in K) and tourmaline (low in K). Tourmaline shows variation in composition with Ca-rich rims and a Fe- and Ti-rich 'late' generation in addition to a low-Fe, medium-Ca composition in the inner fragments*

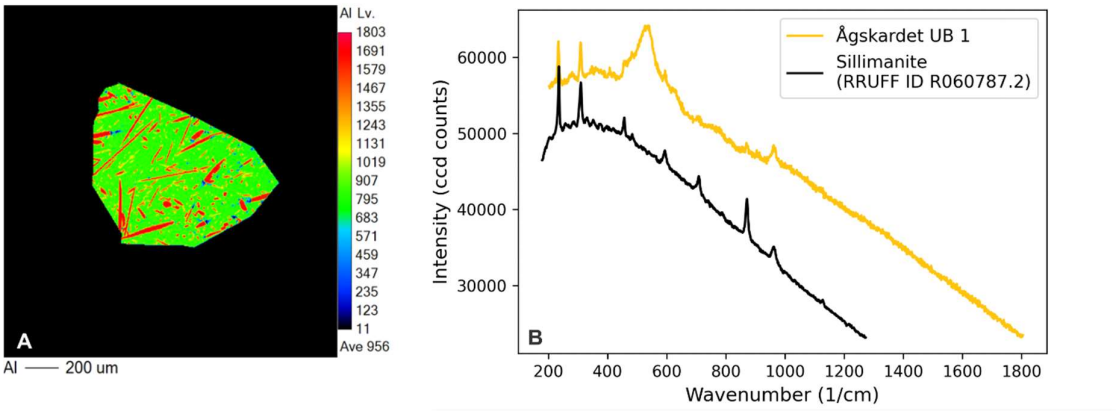

Figure A8. *A) Element map showing high Al contents in acicular sillimanite inclusions within tourmaline. B) Raman spectrum of sillimanite from Ågskardet UB1 (yellow) to sillimanite data from the RRUFF database (Lafuente et al., 2015). Due to the small grain size of the analyzed sillimanite, the analysis is partially mixed between sillimanite and dravite.*

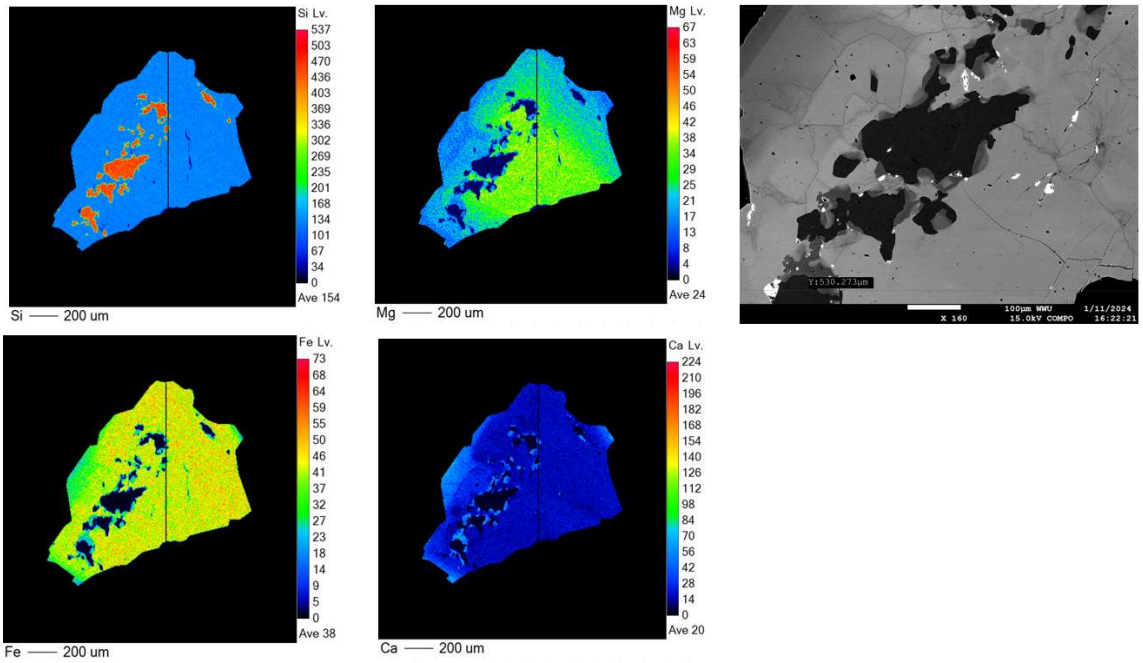

Figure A9. *Element maps and BSE image of a tourmaline grain from Ågskardet OQ4. It has quartz inclusions in the core. The tourmaline in vicinity to the quartz richer in Ca and poorer in Fe than the mean composition.*

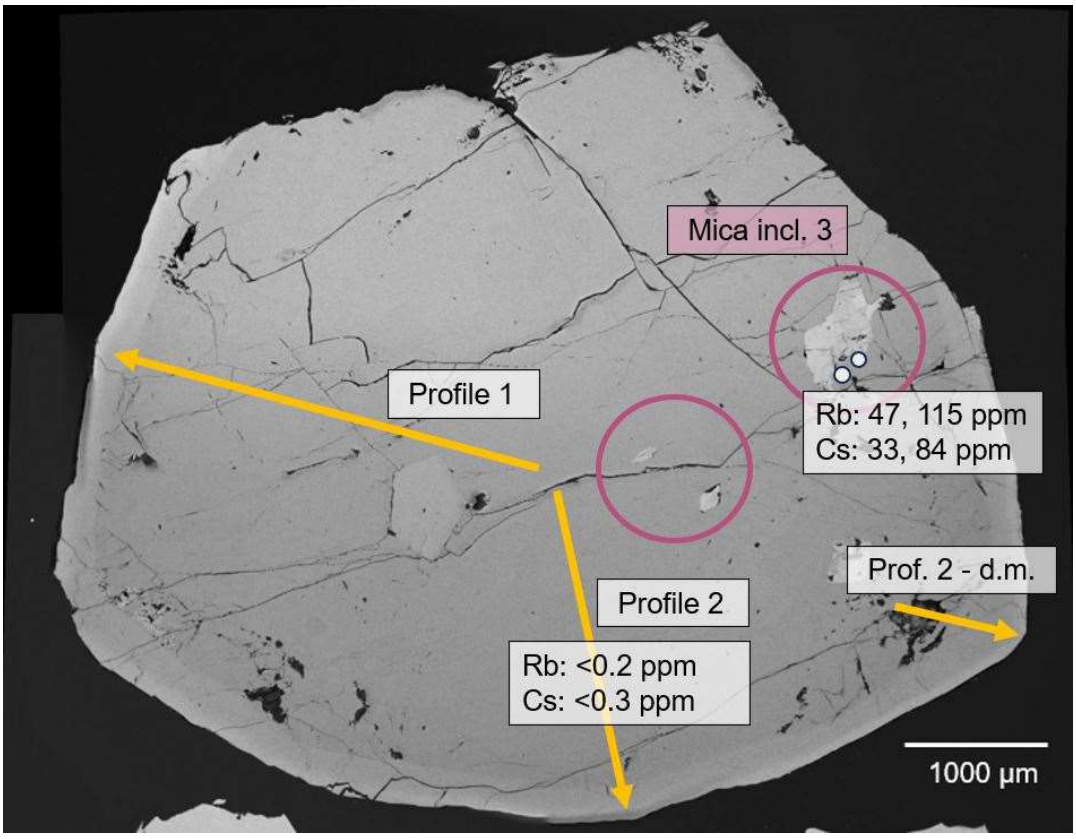

Figure A10*. Tourmaline crystal 111 from Ågskardet OQ5 with indicated analysis profiles of EPMA (profile 1, profile 2, profile 2 detailed margin) and LA-ICP-MS (profile 1 and profile 2) analyses (yellow). Additionally indicated are the analyzed mica inclusions. The two white points indicate tourmaline analysis points adjacent to mica inclusion 3 with elevated Rb and Cs concentrations.*

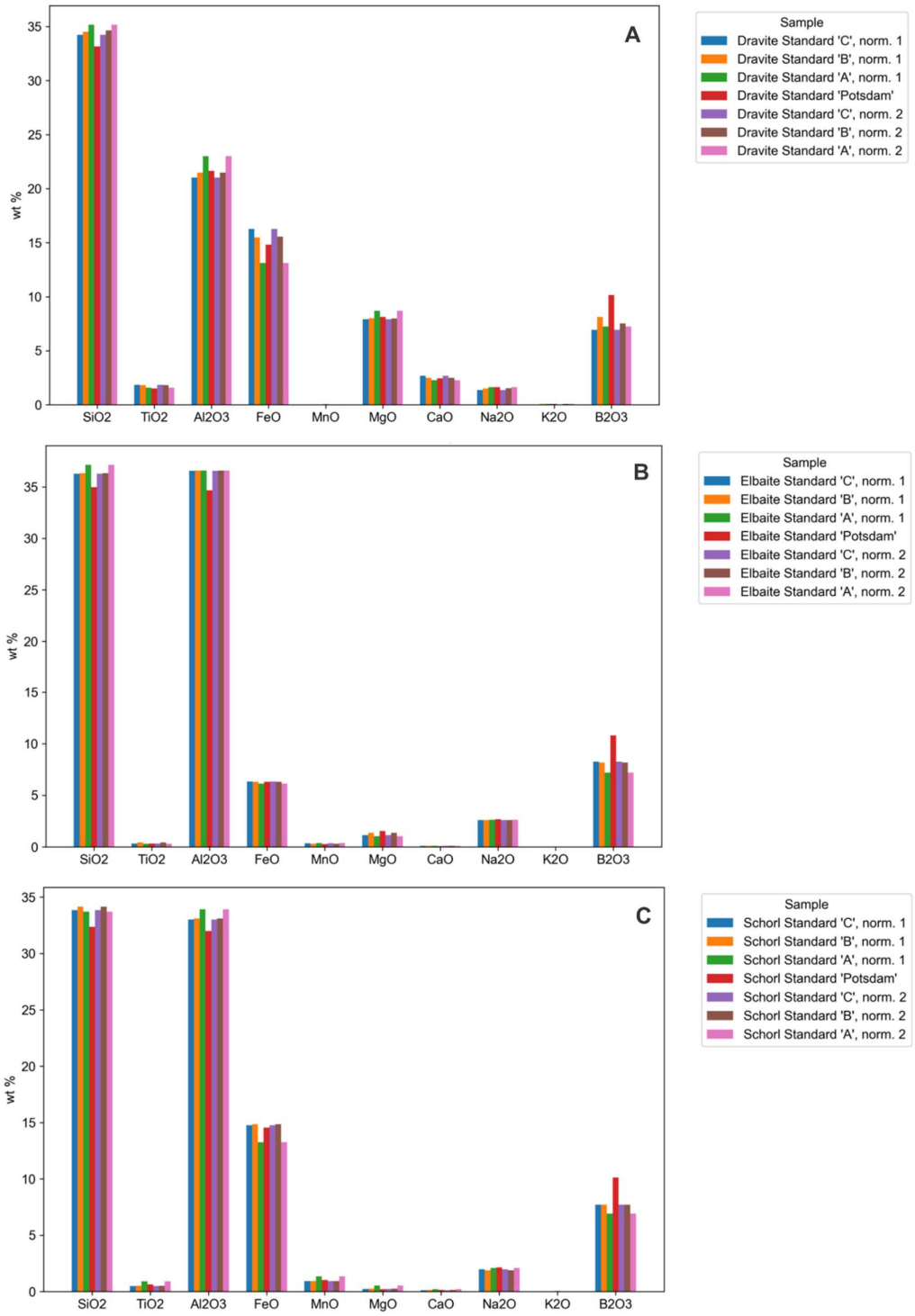

Figure A11. *Effect of normalization procedure on reported major element composition of tourmaline, by the example of the tourmaline standards embedded for use in SIMS analyses. Norm. 1 = Y+Z+T=15 normalization procedure; norm. 2: 31 anions normalization procedure. Values labeled 'Potsdam' are taken from Wiedenbeck et al. (2021). Lower reported B_2O_3 is due to normalization effects. A) Dravite standard. B) Elbaite standard. C) Schorl standard.*

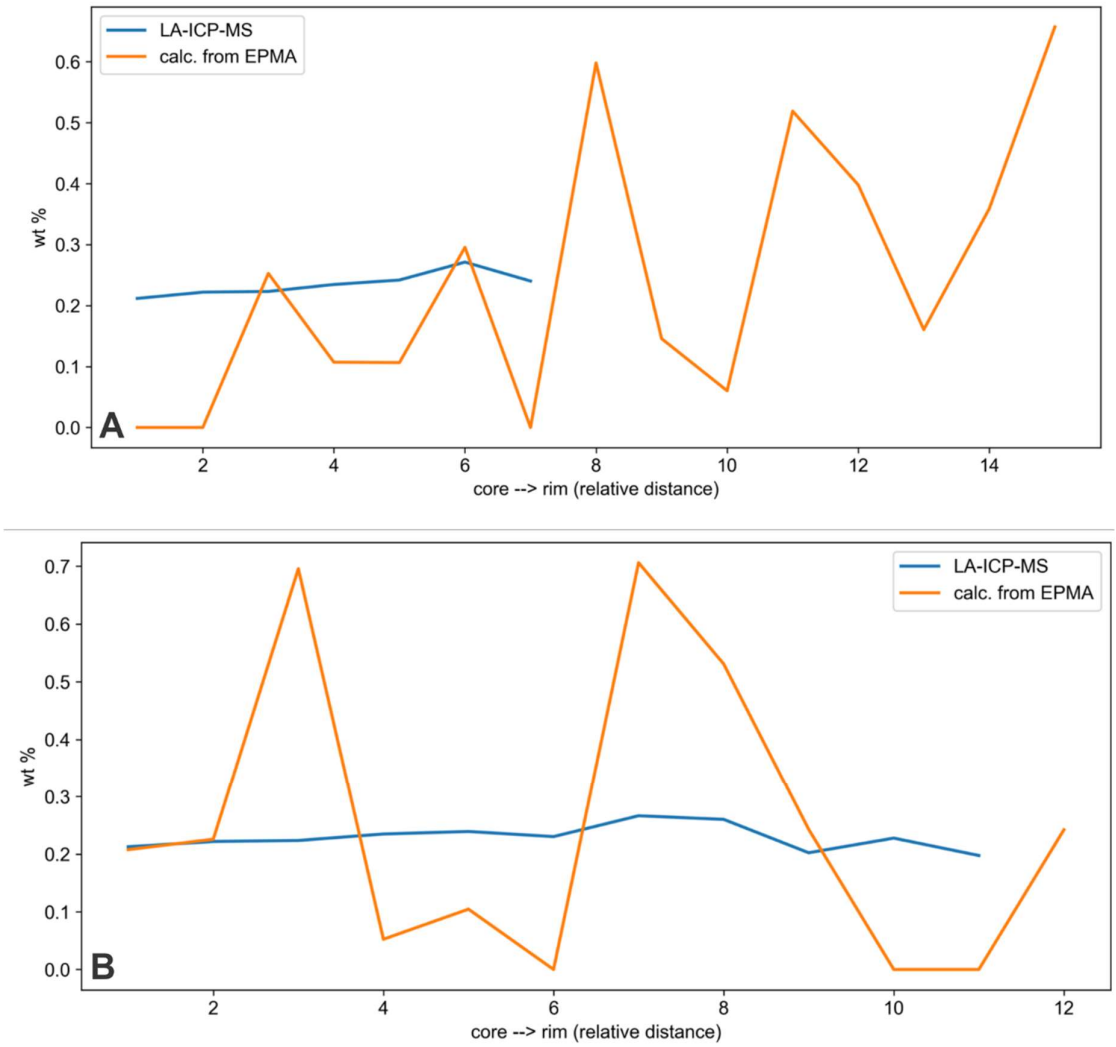

Figure A12. *Comparison of Li_2O content measured by LA-ICP-MS and calculated stoichiometrically based on EPMA results. A) Profile 1 on crystal 111 from Ågskardet OQ5. B) Profile 2 on crystal 111 from Ågskardet OQ5.*

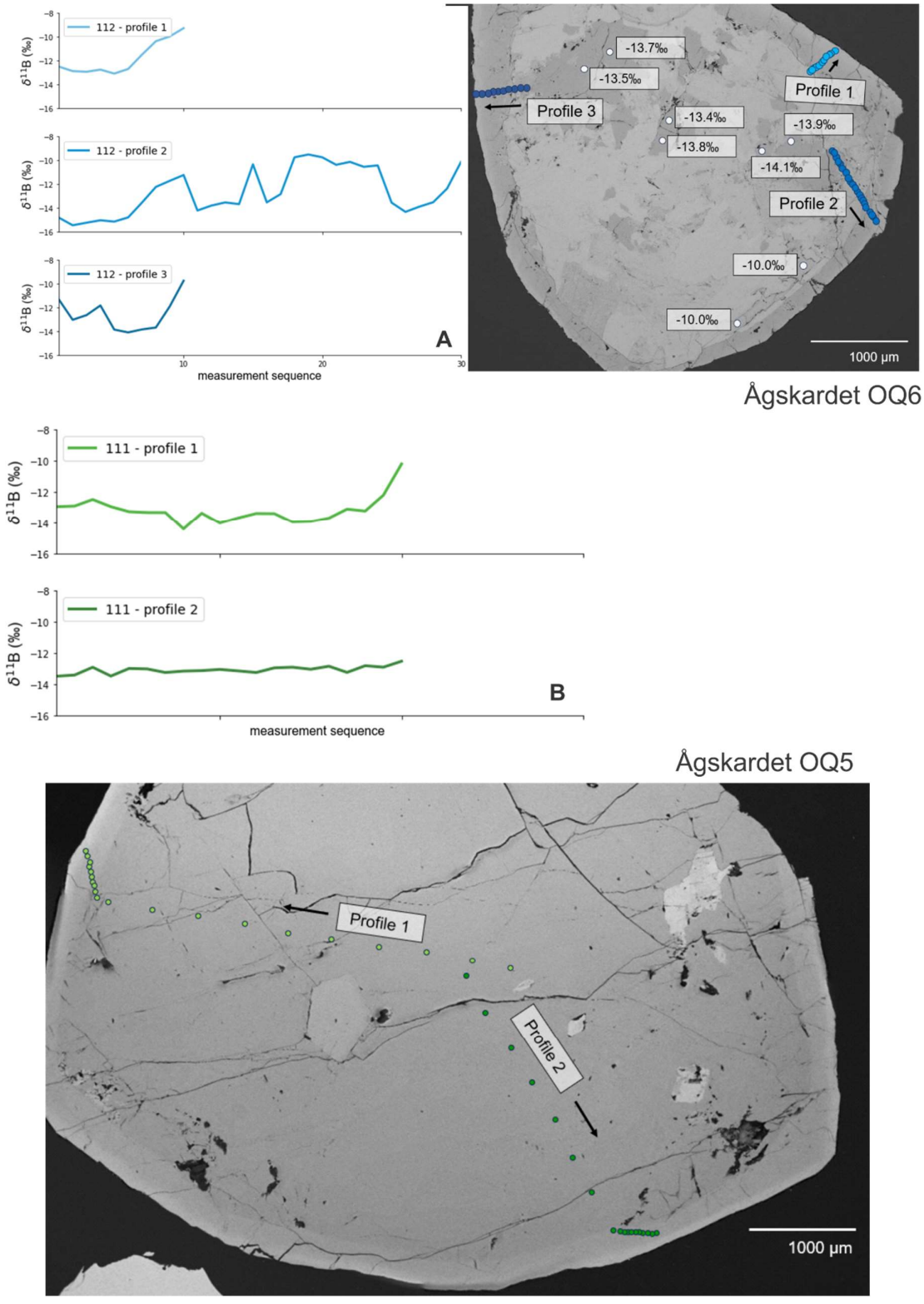

Figure A13. *Tourmaline crystals 112 and 111 from Ågskardet OQ6 and OQ5, respectively, with indicated boron isotope profiles and $\delta^{11}B$ values measured within the different tourmaline generations. A) Ågskardet OQ6. B) Ågskardet OQ5.*

Appendix B

Trace element analyses by LA-ICP-MS

Appendix B is attached as supplementary data file.

Table B1. Trace element analyses of tourmaline from the North Helgeland pegmatites
Table B2. Trace element analyses of garnet from the North Helgeland pegmatites
Table B3. Trace element analyses of mica from the North Helgeland pegmatites

Appendix C

Major element analyses by EPMA

Appendix C is attached as supplementary data file.

Table C1. Major element analyses of tourmaline from the North Helgeland pegmatites
Table C2. Major element analyses of garnet from the North Helgeland pegmatites
Table C3. Major element analyses of mica from the North Helgeland pegmatites

Appendix D

Boron isotope analyses of tourmaline from the North Helgeland pegmatites by SIMS

Appendix D is attached as supplementary data file.